EXPERIMENTAL INVESTIGATION OF THE EFFECTS OF TIP-INJECTION ON THE AERODYNAMIC LOADS AND WAKE CHARACTERISTICS OF A MODEL HORIZONTAL AXIS WIND TURBINE ROTOR

A THESIS SUBMITTED TO
THE GRADUATE SCHOOL OF NATURAL AND APPLIED SCIENCES
OF
MIDDLE EAST TECHNICAL UNIVERSITY

BY

ANAS ABDULRAHIM

IN PARTIAL FULFILLMENT OF THE REQUIREMENTS
FOR
THE DEGREE OF MASTER OF SCIENCE
IN
AEROSAPCE ENGINEERING

SEPTEMBER 2014

Approval of the thesis:

EXPERIMENTAL INVESTIGATION OF THE EFFECTS OF TIP-INJECTION ON THE AERODYNAMIC LOADS AND WAKE CHARACTERISTICS OF A MODEL HORIZONTAL AXIS WIND TURBINE ROTOR

Submitted by **ANAS ABDULRAHIM** in partial fulfillment of the requirements for the degree of **Master of Science in Aerospace Engineering Department, Middle East Technical University** by,

Prof. Dr. Canan Özgen
Dean, Graduate School of **Natural and Applied Sciences** _____

Prof. Dr. Ozan Tekinalp
Head of Department, **Aerospace Engineering** _____

Assoc. Prof. Dr. Oğuz Uzol
Supervisor, **Aerospace Engineering Dept., METU** _____

Examining Committee Members:

Prof. Dr. İsmail H. Tuncer
Aerospace Engineering Dept., METU _____

Assoc. Prof. Dr. Oğuz Uzol
Aerospace Engineering Dept., METU _____

Assoc. Prof. Dr. İlkay Yavrucuk
Aerospace Engineering Dept., METU _____

Asst. Prof. Dr. Monier Ali Elfarra
Faculty of Air Transportation, THK _____

Prof. Dr. Ünver Kaynak
Mechanical Engineering Dept., TOBB ETU _____

Date: 01.09.2014

I hereby declare that all information in this document has been obtained and presented in accordance with academic rules and ethical conduct. I also declare that, as required by these rules and conduct, I have fully cited and referenced all material and results that are not original to this work.

Name, Last Name: Anas Abdulrahim

Signature :

ABSTRACT

EXPERIMENTAL INVESTIGATION OF THE EFFECTS OF TIP-INJECTION ON THE AERODYNAMIC LOADS AND WAKE CHARACTERISTICS OF A MODEL HORIZONTAL AXIS WIND TURBINE ROTOR

Abdulrahim, Anas

M.S., Department of Aerospace Engineering

Supervisor: Assoc. Prof. Dr. Oğuz Uzol

September 2014, 102 pages

In this study, tip injection is implemented on a model Horizontal Axis Wind Turbine (HAWT) rotor to investigate the power and thrust coefficient variations as well as the wake characteristics. The model wind turbine has a 0.95 m diameter 3-bladed rotor with non-linearly twisted and tapered blades that has NREL S826 profile. The nacelle, hub and the blades are specifically designed to allow pressurized air to pass through and get injected from the tips while the rotor is rotating. The experiments are performed at selected tip speed ratios by placing the turbine at the exit of a 1.7 m diameter open-jet wind tunnel facility. This thesis will present a comparative study of the power and thrust coefficient distributions with Tip Speed Ratio (TSR) for the baseline (no-injection) case as well as for the injection cases. In addition, wake measurements using Constant Temperature Anemometry (CTA) system have been conducted at different axial locations downstream of the rotor plane. Results show that, when there is injection, obtained characteristics have significant differences compared to the baseline case both for the load data showing an increase in power and thrust coefficients for TSR values starting near maximum C_P condition up to higher TSR levels as well as for the wake characteristics showing a tip flow region

that is radially pushed outwards with increased levels of turbulence occupying wider areas compared to the baseline case. Within the wake zone, it’s observed that the boundary between the wake and the freestream gets wider and more diffused due to tip injection. Finally, tip injection shows a power deficiency in terms of increasing the load data, since we are spending more power on the injected air than we gain. Therefore, it is best used for instantaneous active load control depending on flow conditions and load requirements.

Keywords: Tip vortex, Flow Control, Tip Vortex Control, Tip Injection, HAWT

ÖZ

UÇ ENJEKSİYONUNUN YATAY EKSENLİ BİR MODEL RÜZGAR TÜRBİNİNİN AERODİNAMİK YÜK VE İZ BÖLGESİ KARAKTERİSTİKLERİ ÜZERİNDEKİ ETKİSİNİN DENEYSEL OLARAK İNCELENMESİ

Abdulrahim, Anas
Yüksek Lisans, Havacılık ve Uzay Mühendisliği Bölümü
Tez yöneticisi: Doç. Dr. Oğuz Uzol

Eylül 2014, 102 sayfa

Bu çalışmada, uç enjeksiyonu yatay eksenli model bir rüzgar türbini rotoruna uygulanarak farklı enjeksiyon senaryolarında güç ve yük karakteristikleri üzerindeki etkileri incelenmiştir. Model rüzgar türbini 0.95 m çaplı ve 3 palli bir rotora, paller ise NREL S826 kanat profilinde ve doğrusal olmayan burulma ve veter dağılımına sahiptir. Nasel, pal göbeği ve paller, rotor dönerken basınçlı havanın sistemden geçerek pal uçlarından enjekte edilebilmesi için özel olarak tasarlanmıştır. Deneyler, seçilmiş uç hız oranlarında ve 1.7 m çapındaki açık-jet tünelinin çıkışında gerçekleştirilmiştir. Dolayısıyla bu tez referans ve enjeksiyonlu koşullarda güç ve yük katsayılarının uç hız oranına göre değişimini karşılaştırılmalı olarak sunmaktadır. Ek olarak, türbin iz bölgesi ölçümleri sabit sıcaklıklı tel anemometresi (CTA) kullanılarak rotor düzleminin arkasındaki farklı eksenel konumlarda gerçekleştirilmiştir. Son olarak, rotor düzleminin arkasındaki akış alanı, tek sensörlü sabit sıcaklıklı tel anemometresi kullanılarak referans (enjeksiyonsuz) ve enjeksiyonlu durumlar için taranmıştır. Sonuçlar göstermiştir ki, uç enjeksiyonu kullanıldığında ölçülen değerlerde referans değerlere göre önemli bir fark oluşmaktadır. Bu fark uç enjeksiyonlu yük ölçümleri için kuvet ve güç katsayılarında

özellikle uç hız oranı maksimum güç katsayısındaki uç hız oranına eşit ve daha yüksek değerler için artış göstermektedir. Türbin iz bölgesinde ise enjeksiyon ile birlikte türbin uç iz bölgesinin, radyal olarak dışarı doğru itildiği ve türbülans seviyelerinin referans ölçümlere göre artarak daha geniş alanlar kapladıkları gözlemlenmiştir. Rotor çapının iki katına kadar olan uzaklıklarda türbin iz bölgesi içerisinde, iz bölgesi ve ana akış arasındaki sınırın uç enjeksiyou ile birlikte genişlediği, akışın içinde daha çok dağıldığı ve türbülans seviyelerinin arttığı tespit edilmiştir.

Anahtar Kelimeler: Uç Girdabı, Akış Kontrolü, Uç Girdabı Kontrolü, Uç Enjeksiyonu, Yatay Eksenli Rüzgar Türbini

Be the change you want to see in the world…

ACKNOWLEDGEMENTS

I would like to express my sincere gratitude to my supervisor Assoc. Prof. Dr. Oğuz Uzol for his professional support, mentorship, guidance, friendship and constant encouragement throughout this thesis work. I deeply appreciate his patience and many efforts to proofread my thesis and papers.

I would like to thank my jury members Prof. İsmail H. Tuncer, Prof. Ünver Kaynak, Assoc. Prof. Dr. İlkay Yavrucuk as well as Asst. Prof. Dr. Monier A. Elfarra for their reviews and comments. I would like to express my gratitude to Dr. Monier for his support and friendship for the past 7 years. Dr. Monier has been a mentor for me during this period and I have learned quite a lot from him and I am still learning. Moreover, I would like to also express my gratitude to Dr. Ilkay for his advice throughout this period, the small conversation I used to have with him always helped me widen my prespective and gave me a lot of encouragement.

I would like to thank my friends and collegues, Ezgi Anık, Yashar Ostovan, Bayram Mercan, that supported me throughout this thesis study, I have learned so much from them. We had so many ups and downs, but above all I enjoyed every moment with them.

I am very grateful for all the friendships I have made in the workplace, this place has been my home for the past 3 years and the people within are like family to me. I am so grateful to be part of such an environment and work place.

I would like to especially thank Gökhan Ahmet for his friendship and support throughout this time. He is one of the most amazing people I have ever met in my life, I am truly grateful for his friendship. I would like to also thank Başak Zeka for her friendship and help throughout this time. Whenever I needed a friend she was

there, she is an amazing person, my guardian angel, and I am grateful to have met her.

Lastly I would like to thank God for giving me the best parents and family I could ever dream to have. Without their constant prayers and support, I wouldn’t have survived and accomplished everything I dreamed off. They have been my motivation and they will always be my driving force to proceed further in life.

This study is supported by the Scientific and Technological Research Council of Turkey (TÜBITAK) under the project number 112M105 as well as by METU Center for Wind Energy (METUWIND). Their support is greatly appreciated.

TABLE OF CONTENTS

LIST OF TABLES

TABLES

LIST OF FIGURES

FIGURES

NOMENCLATURE

AFC	*Active Flow Control*
BEM	*Blade Element Momentum Theory*
CFD	*Computational Fluid Dynamics*
CTA	*Constant Temperature Anemometry*
DAQ	*Data Acquisition system*
FBD	*Free Body Diagram*
HAWT	*Horizontal Axis Wind Turbine*
NREL	*National Renewable Energy Laboratory*
PFC	*Passive Flow Control*
PBC	*Power Budget Calculation*
PE	*Power Efficiency*
RANS	*Reynolds Averaged Navier-Stokes Equations*
TSR	*Tip Speed Ratio*

$\boldsymbol{A}$	*rotor cross sectional area* [m^2]
$\boldsymbol{\beta}$	*open area ratio*
$\boldsymbol{C_P}$	*Power Coefficient*
$\boldsymbol{C_T}$	*Thrust Coefficient*
$\boldsymbol{D}$	*rotor diameter* [m]
$\boldsymbol{Re}$	*Reynolds number*
$\mathbf{R_M}$	*Injection Momentum Ratio*
$\mathbf{R_V}$	*Injection Velocity Ratio*
$\mathbf{R_1}$	*Mass flow ratio*
$\boldsymbol{R}$	*radial distance* [m]
$\boldsymbol{R_{tip}}$	*rotor radius* [m]
$\boldsymbol{P}$	*Power available in the wind* [Watt]
$\boldsymbol{P_{BL}}$	*Rotor power for baseline case* [Watt]
$\boldsymbol{P_{INJ}}$	*Rotor power for injection case* [Watt]

$\boldsymbol{P_{total}}$	*Total pressure* [Pa]
$\boldsymbol{P_{static}}$	*Static pressure* [Pa]
$\boldsymbol{P_{dynamic}}$	*Dynamic pressure* [Pa]
$\boldsymbol{\rho}$	*density of air* [kg/m^3]
$\boldsymbol{U_{\infty}}$	*free stream velocity* [m/s]
$\boldsymbol{U_{tip}}$	*velocity at the blade tip* [m/s]
$\boldsymbol{U_{jet}}$	*injected air velocity* [m/s]
$\boldsymbol{\omega}$	*rotational velocity at the blade tip* [rad/s]
$\boldsymbol{\Omega}$	*Rotational velocity of turbine rotor* [rad/s]
$\boldsymbol{\lambda}$	*Tip Speed Ratio (TSR)*
$\boldsymbol{Q}$	*torque on the element*
$\boldsymbol{T}$	*Thrust force* [N]
$\boldsymbol{\Delta\Gamma}$	*strength of wake rotation*
$\boldsymbol{TI}$	*turbulence intensity*
$\boldsymbol{x/R}$	*streamwise direction*
$\boldsymbol{y/R}$	*radial direction*
$\boldsymbol{z/R}$	*vertical direction*
$\dot{m}_{inlet}$	*Inlet mass flow rate calculated using the flow meter* [kg/s]
$\dot{m}_{rotor}$	*Mass flow rate of air going through rotor disk* [kg/s]
$\dot{m}_{jet}$	*Mass flow rate of the injected air from each blade tip* [kg/s]
$\dot{m}_{jet,total}$	*Total mass flow rate of the injected air* [kg/s]
mom_{jet}	*Momentum of the injected air from each blade tip*
$mom_{jet,total}$	*Total momentum of the injected air*
mom_{rotor}	*Momentum of air going through rotor disk*

CHAPTER 1

INRODUCTION

The quest for new and renewable sources of energy has inspired many researchers and engineers around the world for the past few decades. Wind energy is considered one of the most promising and attractive areas of development. Engineers have developed wind turbines in order to extract the energy available in the wind and transformed it into electricity. In order to increase the energy production from the wind, arrangements of wind farms has been adopted in many countries around the world. The first wind farm was developed in 1970 in California, United States as shown in Figure 1.1 (left). In Europe the development of wind farms started in 1980 in Denmark. Currently, Denmark, Germany, Spain and the Netherlands are the leading European countries in the wind energy industry [1].

In a wind farm wind turbines are placed in an organized manner in order to extract the greatest amount of energy available in the wind. With this arrangement, the different wind turbines will be subjected to different wind conditions which results in different power production. The first row of wind turbines will produce the most power, because they are not disturbed by the wakes generated by other turbines.

The wakes generated by the upstream turbines affect the power production of the downstream turbines in two different ways: by the velocity deficits and the increased turbulence intensity [2]. Consequently, in the presence of velocity deficit, less energy will be produced by the downstream wind turbines [1]. Due to this fact, researchers have dedicated tremendous effort in order to understand the development of wakes, their sources, and their effects on the downstream turbines and the individual turbines themselves.

Figure 1.1: (Left) California wind farm (National Renewable Energy Laboratory) [1], (right) Modern utility-scale wind turbine. Reproduced by permission of General Electric [1]

1.1. OVERVIEW ON WIND TURBINE AERODYNAMICS

An overview on the most fundamental aerodynamic concepts related to Horizontal Axis Wind Turbine (HAWT), such as the performance characteristics quantified by the power and thrust distributions, blade aerodynamics, and wake aerodynamics will be briefly presented in this section.

1.1.1. Performance Characteristics

The wind turbine is a device that extracts the kinetic energy of the wind. Horizontal Axis Wind Turbine (HAWT) is the most common type of modern wind turbines (shown in Figure 1.1). These wind turbines typically have 3-bladed rotors. When the wind turbine rotor is exposed to wind velocity, the resulting torque on the rotor blades is converted into electrical energy.

The energy available in a given cross section, $\boldsymbol{A}$, normal to the wind direction is given by:

$$P = \frac{1}{2}\rho U_{\infty}^{3} A \qquad [1.1]$$

Where $\boldsymbol{U_{\infty}}$ is the wind speed and $\boldsymbol{\rho}$ is the density of the air.

The performance characteristics of a given wind turbine are usually depicted through visualizing the characteristic curves. These characteristic curves are basically the power and thrust coefficient distributions against Tip Speed Ratio (***TSR***).

Where the TSR is defined as the relationship between the velocities at the blade tips, where the radius is the distance from the axis of rotation to the tip of the blade, ***R***, and the free stream velocity $\boldsymbol{U_{\infty}}$:

$$TSR = \frac{\Omega R}{U_{\infty}} \qquad [1.2]$$

Where $\boldsymbol{\Omega}$ is the rotational velocity of the wind turbine rotor.

The power coefficient, $\boldsymbol{C_p}$, describes the relationship between the power extracted by the turbine and the power available in the wind through the rotor area:

$$C_P = \frac{Rotor\ Power}{Power\ Available\ in\ the\ Wind} = \frac{P}{\frac{1}{2}\rho U_{\infty}^{3} A} \qquad [1.3]$$

Based on the actuator disc theory, Betz limit is the maximum power $\left(C_P = \frac{16}{27} = 0.593\right)$ a wind turbine can extract from the wind under ideal conditions [2]. Due to the rotation of the wake, a finite number of blades, related tip losses and non-zero aerodynamic drag, the $\boldsymbol{C_p}$ values of operating turbines will not be able to reach the value of Betz limit [1].

The power produced by the rotor is determined as:

$$P = Q\Omega \qquad [1.4]$$

Q represents the torque on the element. Plotting the C_p against the Tip Speed Ratio (***TSR***), Equation 1.2, we obtain the turbine performance curve. A typical example is illustrated in Figure 1.2.

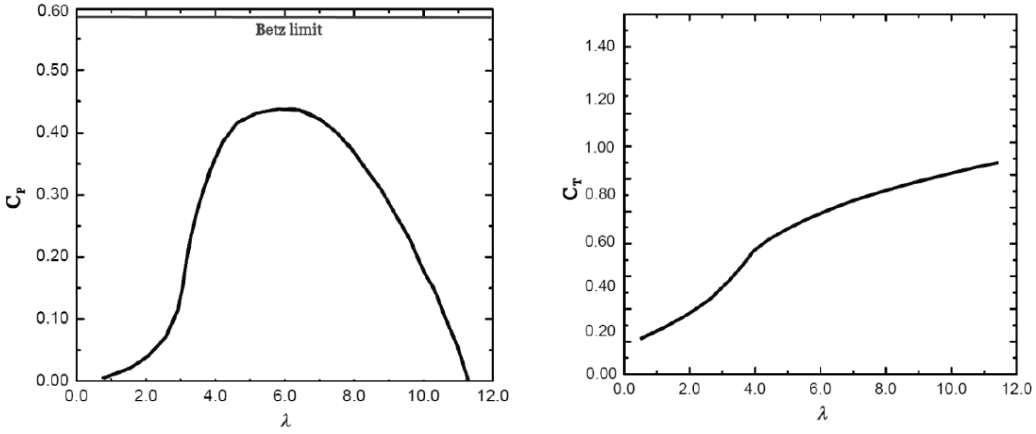

Figure 1.2: Typical C_p-λ and C_T-λ curves of a modern wind turbine [4]. λ represents the tip speed ratio (TSR)

Another parameter used to evaluate the performance of the turbine is the thrust coefficient C_T. The thrust coefficient is defined as the axial thrust force divided by a dynamic force, both acting on the rotor area.

$$C_T = \frac{Thrust\,Force}{Dynamic\,Force} = \frac{T}{\frac{1}{2}\rho U_\infty^2 A} \qquad [1.5]$$

A typical development of the thrust coefficient is illustrated in Figure 1.2. **λ** in the power and thrust coefficients variations corresponds to the tip speed ratio (***TSR***). From this point forward TSR will be used to define the Tip Speed Ratio values.

1.1.2. Blade Aerodynamics

The blades of a wind turbine are the most important component when considering the aerodynamic effects on the wind turbine. The design of the blades aims at extracting as much energy as possible from the wind. Depending on the wind speed and whether the turbine has a variable or constant rotational speed, a specific blade design will be developed.

Most wind turbine blades are designed according to the Blade Element Momentum (***BEM***) theory. The blades are cut into infinitesimally small span-wise blade elements. On every blade elements the two-dimensional cross section is adjusted so that the angle of attack and the aerodynamic forces are optimized.

When the wind turbine is operating, many flow regimes occur where the flow locally does not hit the blades at the designed angle of attack. This can be caused by the highly stochastic wind field hitting the rotor as well as to slow or high rotational speeds of the rotor, which can lead to stall at certain section of the blade. The development of stall at a span-wise blade element is depicted in Figure 1.3 [4].

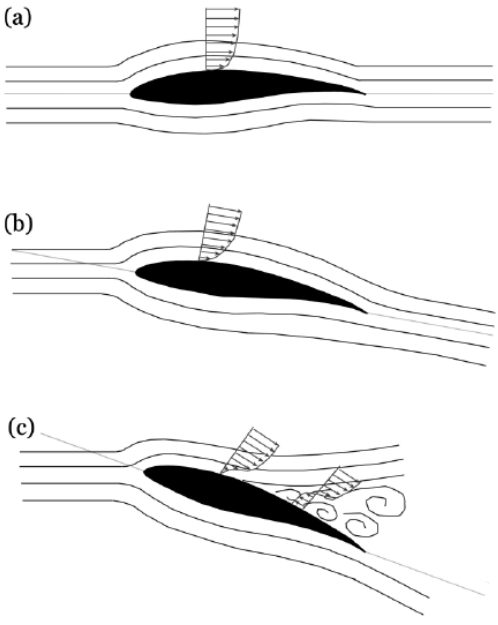

Figure 1.3: Typical flow field around wind turbine blades at different angles of attack

Figure 1.3 (a) shows a wind turbine blade profile subjected to the incoming relative flow at the design angle of attack. The flow adheres and follows the blade profile smoothly. When the relative angle of attack is increased as shown in Figure 1.3 (b) it is still possible for the flow to be attached and follows the profile smoothly. When exceeding the critical angle of attack, the flow cannot follow the blades profiles anymore and highly turbulent recirculation zones appear near the blade surface resulting in flow separation as shown in Figure 1.3 (c). Afterwards so-called stalled conditions are dominant in this section of the blade resulting in substantial aerodynamic losses [4].

The span-wise position on the blade, the operating conditions of the turbine and the type of the incoming wind to the rotor have a considerable influence on the flow exiting from the turbine rotor. The flow behind the turbine rotor is called the wake and it is characterized by a very turbulent flow characteristics. The flow field in the wake behind the rotor is influenced by a number of aerodynamic effects.

1.1.3. Wake Aerodynamics

The aerodynamic conditions present in the flow field downstream of the wind turbine rotor have been an interesting and a challenging research field of study since the beginning of wind turbine development. This flow field is also referred to as the wake of the wind turbine rotor. The stall phenomenon during the operation of a wind turbine together with non-uniform transient inflow defines the aerodynamic conditions prevailing in this wake region.

The main characteristics of the turbine rotor wake are the velocity deficit and turbulence intensity. The velocity deficit causes the downstream turbines to extract lower power in a wind farm arrangement. Moreover, the high levels of turbulence intensity in the wake can inflict large fatigue loads on the downstream turbines [3].

The aerodynamic behavior and shape of the flow field in the wake of a wind turbine rotor is affected by different phenomena. To illustrate, the aerodynamics of the incoming wind, the aerodynamic design and the swirl generated by the rotation of the blades, the root vortices and the shear layer created by the tip vortices as well as the geometry of the wind turbine tower and nacelle which influence the turbulent structures prevailing in the wake [4].

The wake of a wind turbine is typically divided into a near and a far wake [5]. The near wake is the region from the turbine rotor to approximately one rotor diameter downstream, where the turbine geometry determines the shape of the flow field, consequently determining the performance of the turbine. Moreover, the axial pressure gradient is an important factor in developing the wake deficit.

On the other hand, the far wake is the region in which the actual rotor shape is of less importance, whereas the focus lies on wake modeling, wake interference (wake farms), turbulence modeling and topographical effects [5].

The actuator disc theory assumes that the control volume, surrounding the wake, separates the free stream flow from the flow in the wake entirely. In reality this is not the case. The velocity difference between the air inside and outside the wake results in a shear layer, which expands when moving downstream until it reaches the wake axis as illustrated in Figure 1.4. The end of the near wake region is represented by this point.

In this shear layer turbulent eddies are formed, and due to ambient shear flow the turbulence in the shear flow is non-uniform, i.e. the turbulence intensity in the upper part is larger than the lower part. This results in the expansion of the wake and a reduction in the velocity deficit [6 & 7]. Consequently in the far wake the velocity deficit keeps decreasing gradually and the turbulent level is predominant, resulting in a fully developed wake.

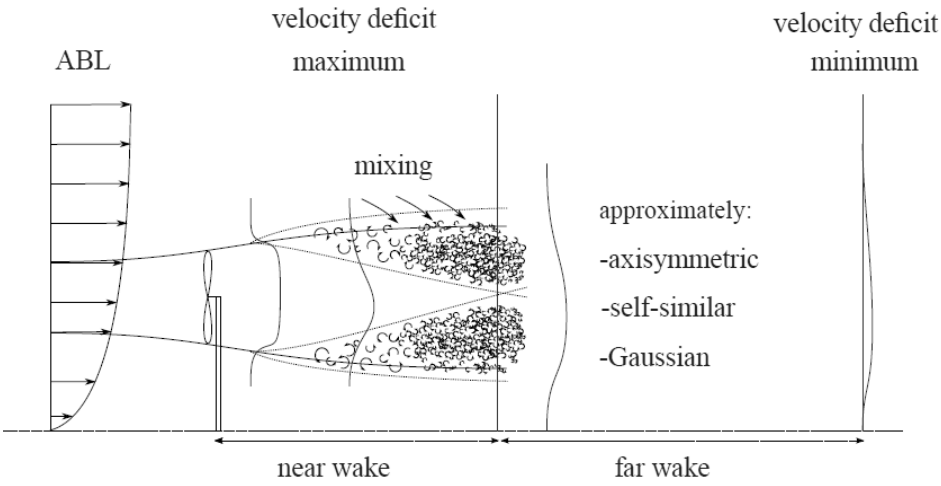

Figure 1.4: Velocity profile and transition between the near and far wake [6]

In a wind turbine wake there are many important aerodynamic factors affecting the behavior and structure of the flow field. For instance, the rotation of the flow field is one of the most important aerodynamic phenomena in the wake of a wind turbine rotor. Manwell et al. [1] claim that the flow behind the rotor rotates in the opposite direction to the rotor, in reaction to the torque exerted by the flow on the rotor. This rotation in the wake contributes to the tangential velocity distribution, since each blade generates a radial, uniform distribution with strength $\boldsymbol{\Delta\Gamma}$.

Another important factor that affects the wake flow field is the formation of tip vortices at the blade tip which leads to the formation of a shear layer that separates the highly turbulent flow in the rotor wake from the free stream flow. This tip vortex is due to the pressure difference between the upper and lower surface of the blade. Consequently, these tip vortices shed by the turbine blades move further downstream with the local velocity in helical spirals having equal strength. As the speed of the blade tips $U_{tip} = \omega R_{tip}$ usually is much higher than the incoming wind speed $\boldsymbol{U}_{\infty}$, the distance between the tip vortex spirals is very low. Therefore, the vortex system can be approximated as a very turbulent cylindrical shear layer [8]. A schematic sketch of the tip vortices forming a cylindrical shear layer is presented in Figure 1.5.

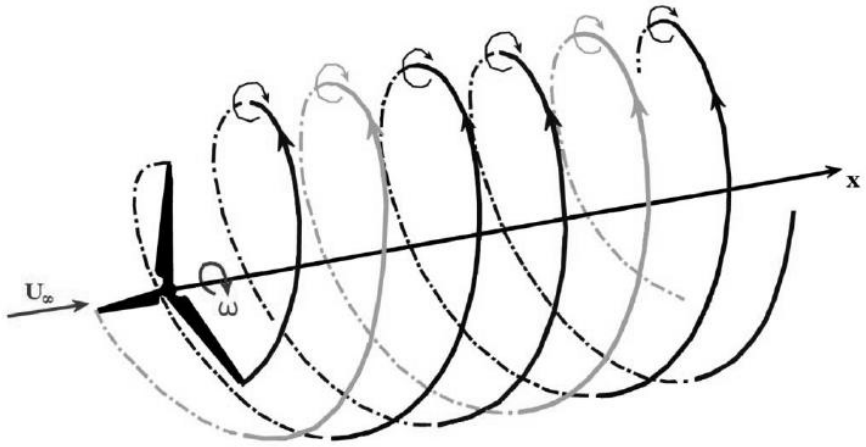

Figure 1.5: Cylindrical shear layers in the wake of the rotor induced by tip vortices

1.2. OVERVIEW ON THE TIP VORTEX FLOW PHENOMENON

In this section an overview of tip vortex flow physics, characteristics and effects on wind turbine operation as well as methods investigated over the years in order to control the tip vortices and minimize its effects will be presented.

1.2.1. Theory and Physics of the Tip Vortex Flow

The tip vortex flow phenomenon has been an interesting topic for many researchers over the years. The tip vortex occurs in many areas such as wings of manned and unmanned aircrafts, propellers and helicopter blades, turbine and compressor blades in turbomachinery studies as well as wind turbine blades. Therefore, an understanding of the tip vortex flow physics, its evolution, decay, and location as well as its effects on lifting surfaces and overall performance of machines is essential.

As fluid flow passes over lifting surfaces, whether the lifting surface is a wing of an aircraft, a blade of a helicopter, a blade of a turbomachinery component, or a wind turbine blade, the flow accelerates over one side of the surface and decelerates over

the other, resulting in a pressure difference across the surface. This pressure difference can result in a force which can be applied for lift or propulsion.

The tip vortices are by-products of the lift generated by the pressure on the lifting surface. This pressure difference results in the leakage of the flow from the lower to the upper surface. When this leakage flow combines with the main stream, concentrated vortical structures get generated at the wing/blade tip usually referred to as tip vortices as shown in Figure 1.6.

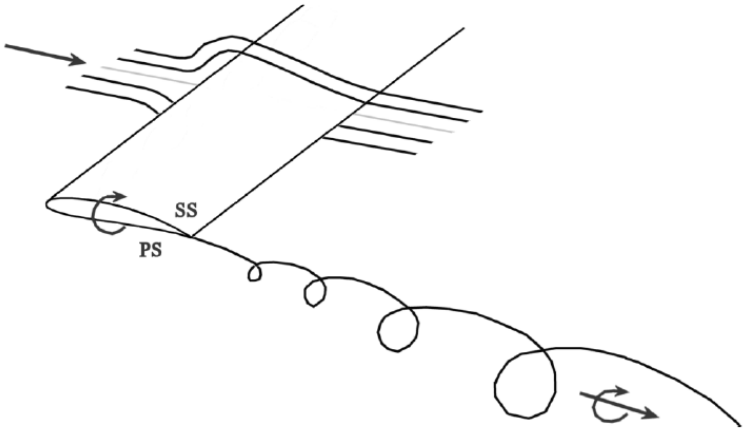

Figure 1.6: Formation of the tip vortex

1.2.2. Overview on the Tip Vortex Control

These vortex structures resulting from the pressure difference can cause a variety of performance losses and noise problems for horizontal axis wind turbines, gas turbine engines, helicopters and airplanes. In addition, these vortices can cause structural and performance problems due to vortex-turbine interactions in successively arranged wind turbines in wind farms.

Therefore, in order to minimize such problems, controlling these vortices is achieved by passive and/or active means. Passive and active control techniques have been mentioned in the literature for many applications ranging from manned/unmanned

aircrafts, helicopters and turbomachinery. However, in this thesis restriction to horizontal axis wind turbine applications will be presented.

The ability to manipulate a flow field passively or actively to improve efficiency and/or the performance of a specific machine is of great technological importance. Flow control is considered one of the leading areas of research in the fluid mechanics community. The potential benefit of flow control includes improved performance, reduced noise, and environmental compliance [9].

The purpose of employing flow control is to delay/advance transition, to suppress/enhance turbulence, or to prevent/promote separation. Consequently, the outcome include drag reduction, lift enhancement, mixing augmentation, heat transfer enhancement, and flow-induced noise suppression [10].

The classification of flow control depends on energy expenditure. Flow control is divided into passive and active methods. Several methods of the two types will be mentioned in the following sections. However, focus will be on application of these methods on wind turbine technology. Furthermore, various passive flow control techniques have found application in actual systems such as delta-wing vortex generators for separation control near the blade roots or winglet like tip extensions for tip leakage control. On the other hand, in terms of Active flow control techniques research efforts are still limited.

1.2.2.1. Passive Flow Control (PFC)

Passive flow control has been widely used in many applications over the years. Passive flow methods modify the flow without external energy expenditure. There are many passive flow techniques and methods used in the literature such as geometric shaping to manipulate the pressure gradient, vortex generators for separation control, and winglets attached to blade tips to manipulate the tip flow [11].

Studies about winglets reveals that adding a winglet causes the wind turbine power to be increased around 0.6% to 1.4% for wind speeds larger than 6 m/s. On the other hand there exists an increase in thrust of around 1% to 1.6% [12]. In addition, Elfarra, [13] in his studies conducted a numerical investigation of the effects of different winglet configurations on horizontal axis wind turbine blade. It is shown that a winglet tilted towards the suction surface of the blade increased the power about 3.5%. Also, the winglet had a slight effect on separation and tip loss reduction. Moreover, Gaunna and Johansen, [14] mentioned in their numerical paper that downwind winglets are superior to upwind ones with respect to optimization of power coefficient and that the increase in power production is less than what may be obtained by a simple extensions of the wing in radial direction. Furthermore, Shimizu et al., [15 & 16] conducted several experimental and numerical studies on special type V-shaped winglets called Mie-Vanes (or tip vanes), results show a decrease in the effect of tip vortices and an increase in the power coefficient of wind turbine by 15%. Also the addition of Mie-Vanes causes significant changes in the flow behavior near the blade tip, resulting in additional blade lift. Moreover, the results of integrating a vortex diffuser on a wind turbine blade show an increase on the total pressure coefficient of the core vortex, and a decrease in the strength of the blade tip vortex, consequently lowering the noise and improving the efficiency of the blade [17].

1.2.2.2. Active Flow Control (AFC)

The implementation of AFC methods, in which energy or auxiliary power is introduced to the flow field, has attracted attention in the last few decades especially in the wind turbine technology due to the tremendous results that AFC could provide, in terms of improving efficiency and performance of turbomachines such as compressors and turbines, combustors, as well as intakes and nozzles.

There are several active flow control techniques used in wind turbine research such as vortex generator jets [18 & 19], blowing & suction [20 & 21], synthetic jets [22 & 23] and plasma actuators [24, 25 & 26].

1.3. LITERATURE REVIEW ON TIP INJECTION

Tip injection which has never been investigated before on wind turbine rotors according to author's best knowledge, it has previously been implemented in many research areas such as fixed wings as well as helicopter and turbomachinery blades. Therefore, the focus of this thesis study will be on tip injection technique which is an active flow control technique aimed at controlling the leakage characteristics at the tip as well as the size, vorticity and turbulence characteristics of the tip vortex. For instance, Ostovan, [27] conducted an experimental study on the effects of tip injection on a rectangular wing with a NACA 0015 airfoil profile. Results show significant effects of the tip injection on the vortex characteristics. To illustrate, the vortex size gets bigger with injection and the total pressure levels get reduced significantly near the vortex core, also it affects the wake behind the wing as well as the wake entrainment characteristics of the tip vortex. Moreover, Bettle, [28] investigated the effect of tip injection on the turbulence characteristics of the wake and the tip vortex. It was shown that tip injection causes significant dispersion and outward movement of the vortex as well as excess momentum and increased turbulent kinetic energy with its core.

Investigations about control of helicopter rotor tip vortex structure using blowing devices show that when high pressure air is provided to tip vortex center, swirl velocity of tip vortex decreases and diffusion of tip vortex increases [29 & 30]. Moreover, Numerical studies of helicopter rotor tip vortex control by tip injection with piezoelectric actuator shows that tip vortex power decreases 14% when the proposed method is applied [31]. In addition, An experimental study, in which high pressure air from leading edge of blade is provided to blade tip, demonstrates that the slotted blade reduces the peak value of the swirl velocity components in the tip

vortex by up to 60% relative to those of the baseline blade and the core growth of the tip vortices from the slotted blade suggested a much higher rate of diffusion, up to as much as three times that of the baseline [32].

Tip injection has been widely used in turbomachinery for turbine/compressor performance enhancement. For instance, an experimental study about tip vortex control using active tip injection method for low pressure turbine cascade shows that pressure loss can be decreased by 15% [33 & 34]. Moreover, Rao, [35] conducted an experimental study of a turbine tip desensitization method based on tip coolant injection in a large-scale rotating turbine rig. It was shown that the coolant injection from the tip trench was successful in filling the total pressure defect originally resulting from the leakage vortex without injection. Furthermore, another study of tip injection effects on tip clearance flow in high turning axial turbine cascade shows that tip injection can weaken tip clearance flow, reducing the tip clearance mass flow and its associated losses [36].

1.4. OBJECTIVES AND SCOPE OF THE THESIS STUDY

The main purpose of this thesis study is to experimentally investigate the effects of tip injection on the aerodynamic loads and wake characteristics of a model horizontal axis wind turbine rotor. The model wind turbine has a 1m diameter 3-bladed rotor with non-linearly twisted and tapered blades that has a NREL S826 profile. The nacelle, hub and the blades are specifically designed to allow pressurized air to pass through and get injected from the tips while the rotor is rotating. The experiments are performed at selected tip speed ratios by placing the turbine at the exit of a 1.7 m diameter open-jet facility. The wind turbine is instrumented to allow torque, thrust and rpm measurements to quantify the performance with and without injection at different tip speed ratios. Wake measurements downstream of the wind turbine rotor are also performed using a Constant Temperature Anemometry (CTA) system to investigate the effects of tip injection on the wake. Results of various tip injection scenarios are compared with the baseline (no injection) case.

1.5. LAY-OUT OF THE STUDY

This thesis study consists of five chapters. Chapter 1 of this thesis includes a brief introduction of the wind energy and wind turbine aerodynamics, as well as a literature review of the main subject of this thesis.

The details of the design and manufacturing process of the wind tunnel and wind turbine are presented in chapter 2. Measurement details including control system and CTA measurements, as well as data acquisition are included in chapter 3.

Detailed explanations and related discussions of the results are presented in chapter 4. Results include aerodynamic performance and wake measurements of the wind turbine rotor as well as tip flow measurements.

Chapter 5 includes conclusions drawn from the results as well as recommendations for future work that can be done to further investigate the problem in hand.

CHAPTER 2

EXPERIMENTAL SETUP

This chapter summarizes the details of the wind tunnel as well as the model wind turbine design, manufacturing and instrumentation process.

2.1. OPEN-JET WIND TUNNEL FACILITY

In order to conduct an experimental investigation of the wind turbine performance characteristics such as load measurements and wake analysis, an open jet wind tunnel facility was designed and constructed for this specific application. This section summarizes the preliminary design and manufacturing process of the wind tunnel to be utilized for the experiments. In addition, wind tunnel characterization is also presented.

2.1.1. Preliminary Computational Fluid Dynamics (CFD) Analysis of the Wind Tunnel

This section provides a preliminary Computational Fluid Dynamics (CFD) analysis of the design of the open jet wind tunnel required for this study. To begin with, the wind turbine has a 1 m diameter 3-bladed rotor. Therefore, the open jet wind tunnel exit diameter should be greater than 1.5 m. The wind tunnel is divided into two main parts, a diffuser section starting with a 1.25 m circular inlet which is the diameter of the fan, reaching out to a 1.5 m circular exit. Also, the diffuser is followed by a circular straight duct with a diameter of 1.5 m and a length of 0.5 m.

The aim of the CFD analysis is to predict the flow regime inside the wind tunnel, and to predict the desired diffusion angle for the diffuser, as well as the total length of the wind tunnel and the inflow speed at the jet exit.

The diffusion angle is considered an important parameter in the design of the diffuser section of the wind tunnel. The diffusion angle affects the diameter of the diffuser outlet and the total length of the diffuser. Moreover, it also affects the boundary layer thickness and the flow regime inside the diffuser. Theoretical studies shows that the diffusion angle must not exceed 7 degrees, otherwise flow separation will be inevitable. Therefore preliminary two- dimensional CFD analysis was performed to determine the appropriate diffusion angle. Consequently the total length of the tunnel will be determined.

Figure 2.1 shows the geometry of the wind tunnel and the unstructured mesh used in the analysis. The mesh has been generated using the Fluent Gambit version 2.4.6. The cell growth rate was taken as 1.2. Flow direction, inlet and exit of the wind tunnel are also specified in Figure 2.1.

Wall boundary condition which is used to separate fluid and solid zones has been used to define the tunnel geometry. The no-slip boundary condition is enforced at the walls. The inlet boundary conditions were set as mass flow rate inlet conditions. They were taken from the performance curve of the fan shown in Figure 2.2.

Pressure outlet boundary conditions were applied to the flow outlet. It is necessary to specify a gauge pressure for this condition. In the present cases, the gauge pressure is set to be zero. These values with fluid density and temperature were taken for Ankara atmospheric conditions mentioned in Table 2.1.

The Fan specifications and dimensions are mentioned in Appendix A.

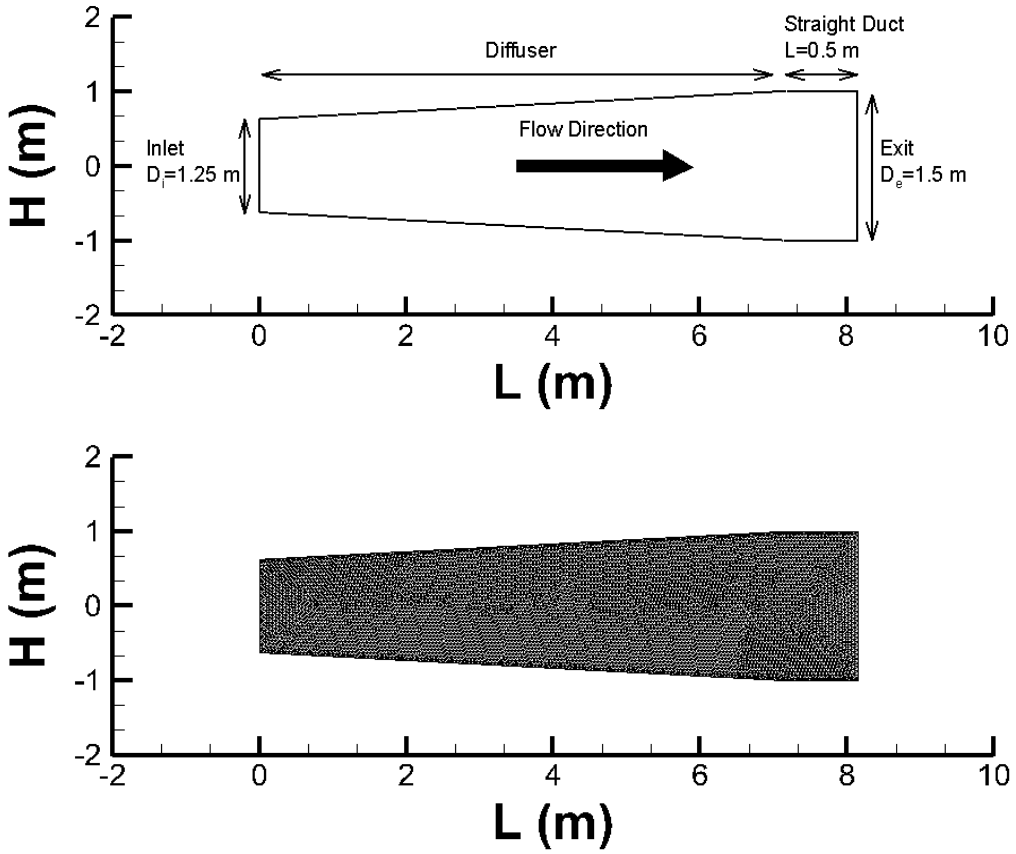

Figure 2.1: Geometry of the wind tunnel (top), and the unstructured mesh (bottom)

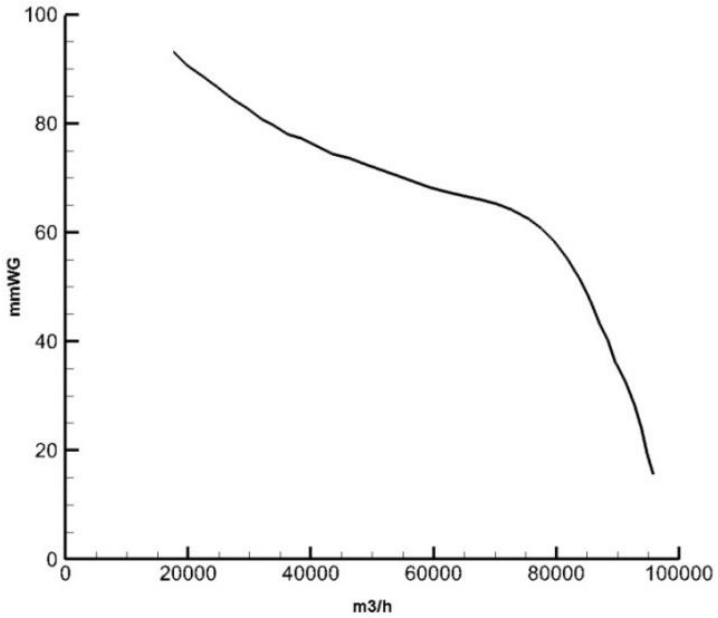

Figure 2.2: Fan performance curve

Table 2.1: Ankara atmospheric conditions

ANKARA Atmospheric Conditions			
Altitude (m)	**ρ (kg/m^3)**	**Pressure (Pa)**	**Temperature (K)**
850	1.128	91,522	282.625

Two dimensional steady Reynolds Averaged Navier-Stokes (RANS) solution has been solved by Fluent 6.3. Second-order upwind solution methods were implemented. Moreover, the turbulence model used in the analysis is the Spalart Almaras turbulence model.

There are four different diffusion angles used in the analysis (3, 4, 5 & 6 degrees). Figure 2.3 shows the results of the CFD analysis. The results are represented by velocity magnitude contours.

Results show that for diffusion angles 5 and 6, flow separation is evident. Also the velocity at the tunnel exit is predicted to be around 10 m/s.

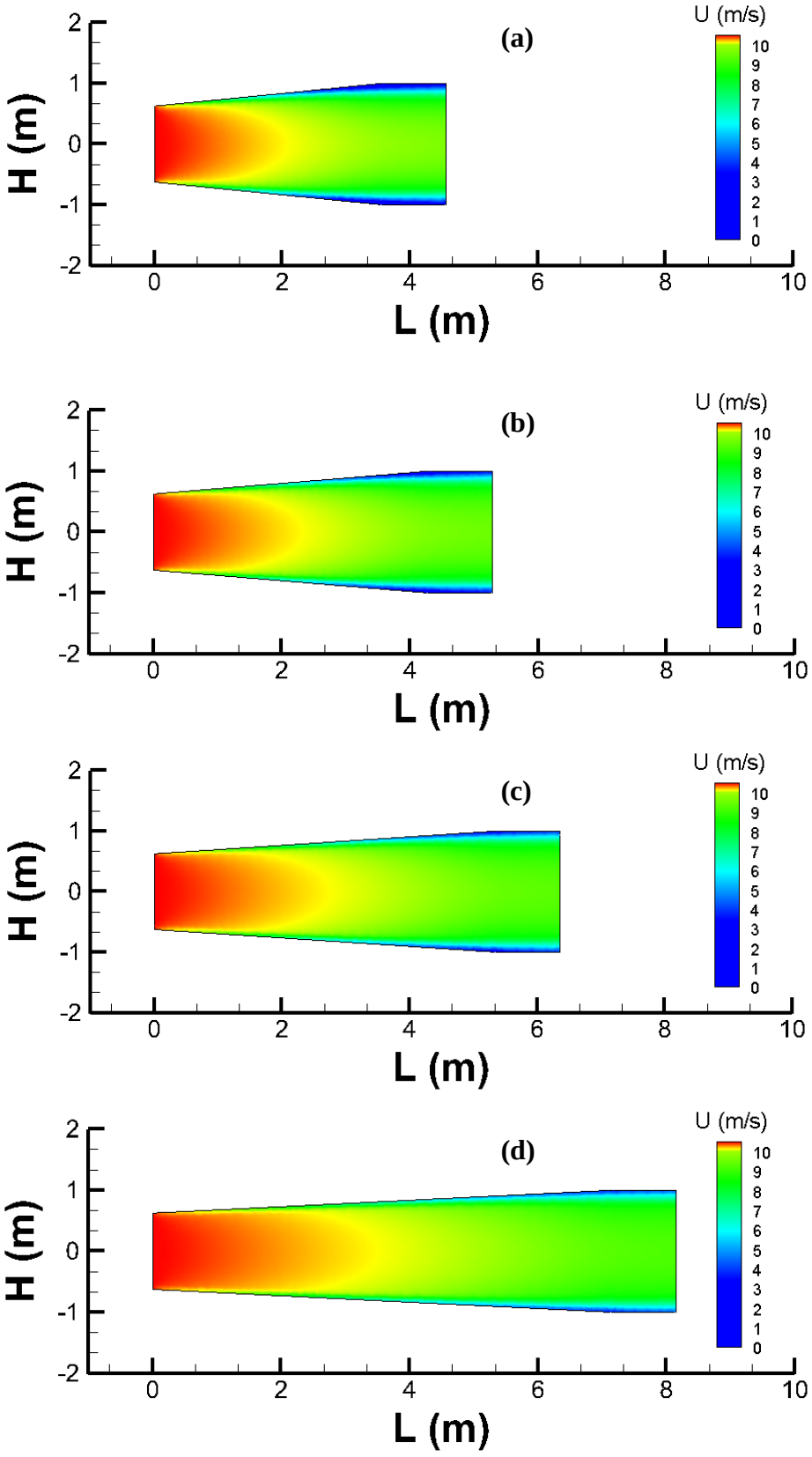

Figure 2.3: CFD analysis of the open jet wind tunnel at different diffusion angles: (a) 6 degrees, (b) 5 degrees, (c) 4 degrees, (d) 3 degrees

Figure 2.4 shows the velocity profiles at the exit of the open jet wind tunnel. The purpose of these velocity profiles is to predict the boundary layer thickness and to observe the flow uniformity at the tunnel exit that the wind turbine rotor will encounter. As the diffusion angle increases, the boundary layer thickness increases. And the width of the flow uniformity will decrease. The maximum width of the flow uniformity is from (-0.6<y<+0.6). Diffusion angles 3 & 4 gives a more uniform flow compared with the other cases. Therefore with the addition of flow straighteners the flow quality will improve.

The total length of the wind tunnel is greatly affected by the diffusion angle of the diffuser. Therefore, the length of the tunnel is an important factor in deciding the location of the tunnel in the hangar building where the tunnel will be located. Table 2.2 shows the total length of the tunnel for different diffusion angles.

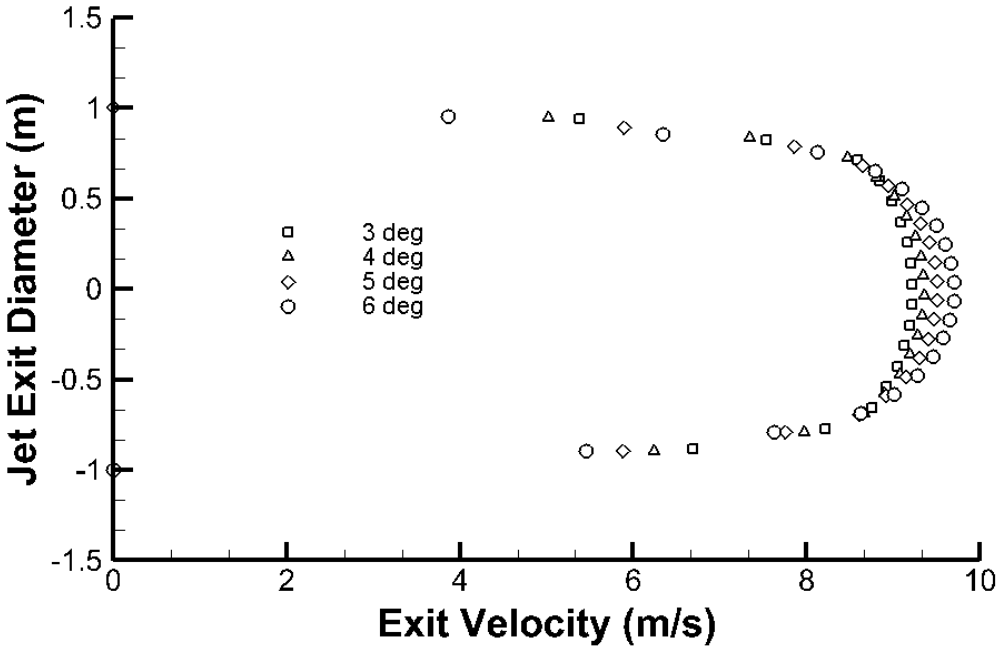

Figure 2.4: Velocity profiles for different diffusion angles

Table 2.2: Tunnel total length (Diffuser + Straight Duct)

Diffuser expansion angle (degrees)	**Tunnel total length (m)**
3	7.16
4	5.36
5	4.29
6	3.57

In conclusion, based on the preliminary CFD analysis and the velocity profiles shown in Figure 2.4, a diffuser with a diffusion angle of 3 degrees presents the best results for the wind tunnel design. Therefore, a diffusion angle of 3 degrees gives the tunnel total length to be 7.16 m.

2.1.2. Flow Straightener Design

In order to decrease the turbulence levels and improve the flow quality of the open jet wind tunnel. The installation of flow straighteners is required to achieve the desired goals.

There are two types of flow straighteners used in a wind tunnel, namely screens and honeycombs. The physical mechanism for decreasing turbulence is different for screens and honeycombs. Screens reduce axial turbulence more than lateral turbulence, whereas honeycomb reduces lateral turbulence more than axial turbulence [37].

In this section a literature review of the design criteria for screens and honeycombs is presented, afterwards the appropriate specifications of the screens and honeycomb are selected in order to be installed on the open jet wind tunnel.

2.1.2.1. Screen Design

They are two types of screens based on the open-area ratio (β), where β is the ratio of the open area (i.e. porous area) to the total area of the screen. If $\beta>0.57$ the screen is a coarse mesh screen, and if $\beta<0.57$ the screen is called a fine mesh screen. Experimental studies show that a coarse screen must precede a fine screen [38]. Moreover, based on CFD data, results show that a screen with $\beta>0.57$ is more effective in reducing directional instability [39]. Whereas a screen with $\beta<0.57$ causes a flow instability in the form of longitudinal vortices that appears in the test section [40]. Therefore, Metha and Bradshaw, [41] in their paper states that at least one screen with a larger $\beta>0.57$ should be installed.

Another important design parameter taken into account is the wire diameter of the screens. Groth and Johansson, [42] state in their paper that wire diameter is an important factor in selecting screens and that it depends on Reynolds number. The open-area ratio and wire diameter for the selected screens are mentioned in details in the selection section.

2.1.2.2. Honeycomb Design

The most important factor in selection of honeycomb is the length-to-diameter ratio. The larger the length-to-diameter ratio the smaller is the lateral turbulence and the higher the pressure loss [40]. There have been many studies in the literature about honeycomb design and selection process. According to Metha and Bradshaw, [41], this ratio should be between 6 & 8. Moreover, Laws and Livesey, [43], stated that this ratio may vary between 5 & 10. In addition, Vinayak and Bradshaw, [39], conducted CFD studies and found out that the length to diameter ratio suitable for honeycomb design is between 8 and 12. Furthermore, experimental studies conducted by Farell and Sadek, [38], show that this value can vary from 5 to 10.

Honeycomb cell can come in different geometries. CFD studies were conducted to study the effect of cell geometry on the flow quality. Results show that cell geometry has no effect on flow quality [39]. Moreover, the open-area ratio for honeycomb should be larger than 0.8 [44].

The selection and placement procedure for honeycomb and screens is described in details in the following section.

2.1.2.3. Selection and Placement of Flow Straighteners

In order to reduce the turbulence levels in the testing chamber and improve the flow quality, placement of the flow straighteners is as important as the selection itself. The distance between the flow straighteners and the sequence of their location affects the flow properties greatly.

This placement distance, the type of flow straightener, the geometry and dimensions of flow straightener, the flow quality of the flow straighteners will decide the placement and order of flow straighteners.

The order of the flow straighteners affects the distance between them, the decay in turbulence levels resulting from the upstream flow straighteners once reaches a constant value determines this distance [45]. Moreover, as mentioned previously in any series of screens, the finest mesh screens are located downstream. Scheiman, [45], relates this distance to turbulence decay, which occurs with 50 to 75 screen meshes downstream of the screen. Also for honeycomb this distance is determined to be about 50 times the cell diameter, or 1 to 10 times the honeycomb thickness. Accordingly, the distance between flow straighteners has to be selected carefully in order to avoid the adverse effects that each flow straightener poses on the other. This distance should be within 80 to 100 mesh size of screens, or at least 30 times the cell diameter of the honeycomb or 4 times the thickness. Studies show that the turbulence decay identifies the distance between screens to be 50 times larger than the mesh size

[42]. Another study shows that the screen spacing should be 0.2 times the settling chamber diameter [41]. In a similar study conducted by Barlow et al., [46], this distance is determined to be around 30 times the mesh size of the screen or around 500 times the wire thickness.

The placement of flow straighteners as well as the spacing between them is greatly affected by the incoming flow. The following sections are dedicated to selecting the flow straighteners as well as determining the spacing between them.

2.1.2.4. Screen Selection and Placement

The selection of screen specifications is an important part of the design. Based on 4201/R357 RevB report [47], the acceptable wire diameter and mesh frequency combination is presented in Figure 2.5. According to these charts the open area ratio was calculated from the wire thickness specified in combination with the mesh frequency. These computations will determine the screens located before and after the honeycomb. Therefore a screen with an open area ratio of $\beta>0.57$ will be installed before the honeycomb and a screen with an open area ratio of $\beta<0.57$ will be installed after the honeycomb. In addition, the selected screens do not cause any undesirable pressure losses if the Reynolds number based on wire thickness for different speeds is under $\mathrm{Re}_{critical} = 50$. In these studies, it was shown that the incoming flow velocity for the screens at the selected wire thickness does not fall under the critical Reynolds number unless they are below 2 m/s. Experiments at 10 m/s open jet velocity were carried out and results show that the screen incoming flow will not fall under the critical Reynolds number and so undesirable pressure losses will not occur. Therefore, the selected screens will operated in safe conditions.

Another important issue is the location of the screen with an open area ratio of $\beta<0.57$. The location is greatly affected by the formation of the boundary layer and its separations. Therefore results show that the appropriate location would be 100 times the mesh size downstream of the honeycomb.

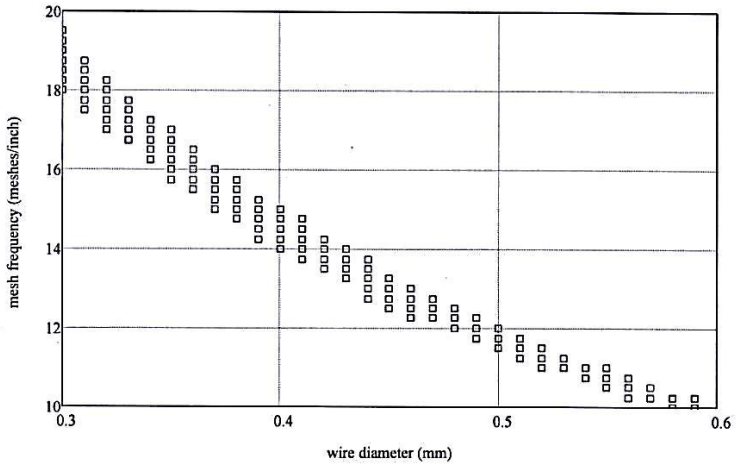

Figure 2.5: Acceptable wire diameter and mesh frequency combination [47]

2.1.2.5. Honeycomb Selection and Placement

The first step in honeycomb selection process is the number of cells. Based on literature the cell number is determined by considering the lateral direction for reducing turbulence in the test section. Based on the diameter of the test section the cell number is determined to be 200 cells per diameter. Another important parameter in the selection of honeycomb is the ratio of thickness to cell diameter. As mentioned previously, this ratio is determined to be between 5 and 10. Moreover the open area ratio will be taken above 0.8. The position of the screen following the honeycomb is selected based on the honeycomb properties determined. Accordingly, the diameter of the cell and the thickness of the honeycomb were determined. According to the calculated values, the distance between the screens is affected by the boundary layer thickness. The optimal distance is 32 times the cell diameter or 4.6 times the honeycomb thickness in order to prevent the formation of boundary layer. This value gives two different placement criteria.

To summarize, the flow straighteners used for this tunnel consist of one honeycomb and one fine mesh screen and one coarse mesh screen. Their specifications, selection and placement are mentioned in Figure 2.5, Table 2.3, and Table 2.4. For further

information related to flow straightener's selection and placement procedure refer to Uzol, [48].

Table 2.3: Flow Straighteners Specifications, Selection and Placement

Name of Flow Straightener	Cell Size	Screen Thickness	Mesh Frequency	Aspect Ratio	Wire Diameter	Location of Flow Straightener
Coarse Screen	-	-	0.53/mm	0.54	0.5 mm	Diffuser Outlet
Honeycomb	12.5 mm	100 mm	-	>0.8	-	220 mm downstream of the coarse screen
Fine Screen	-	-	0.45/mm	0.60	0.5 mm	400 mm downstream of the honeycomb

Table 2.4: Screen Specifications

	Mesh	Wire Diameter [mm]	Opening [mm]	Open Area [%]
Fine	15	0.40	1.25	57
Coarse	18	0.32	1.12	60

2.1.3. Final Version of the Wind Tunnel

This section summarizes the final version of the wind tunnel, production material and differences from the preliminary design.

- The diffuser exit diameter and the tunnel exit diameter have been increased from 1.5 m to 1.7 m.
- The diffusion angle has been kept as 3 degrees.
- The circular straight duct is increased from 0.5 m to 1.4 m.
- The total length of the tunnel has been decreased from 7 m to almost 6 m.

The wind tunnel utilized for conducting the experiments was produced from metal sheets with thickness of 4 mm. The Open-Jet wind tunnel facility is driven by a 45 kW electric motor that runs a 1.25 m diameter axial fan. The open jet facility consists of a 4.3 m long circular diffuser with an inlet cross section diameter of 1.25 m and an exit cross section diameter of 1.7 m with a 3 deg diffusion angle. The diffuser is followed by three straight circular sections (i.e. Circular Ducts) having a diameter of 1.7 m and a total length of 1.4 m. The Open-Jet facility is equipped with flow straighteners (1 Honeycomb & 2 Turbulent Screens) to improve the quality of the flow and ensure a uniform flow at the jet exit. The total length of the wind tunnel with the fan is around 7 m long as shown in Figure 2.6 (top). A 3x3 m^2 cage is also installed in front of the tunnel for protection purposes during the operation of the experiment. Figure 2.7 shows different views of the wind tunnel after production is complete.

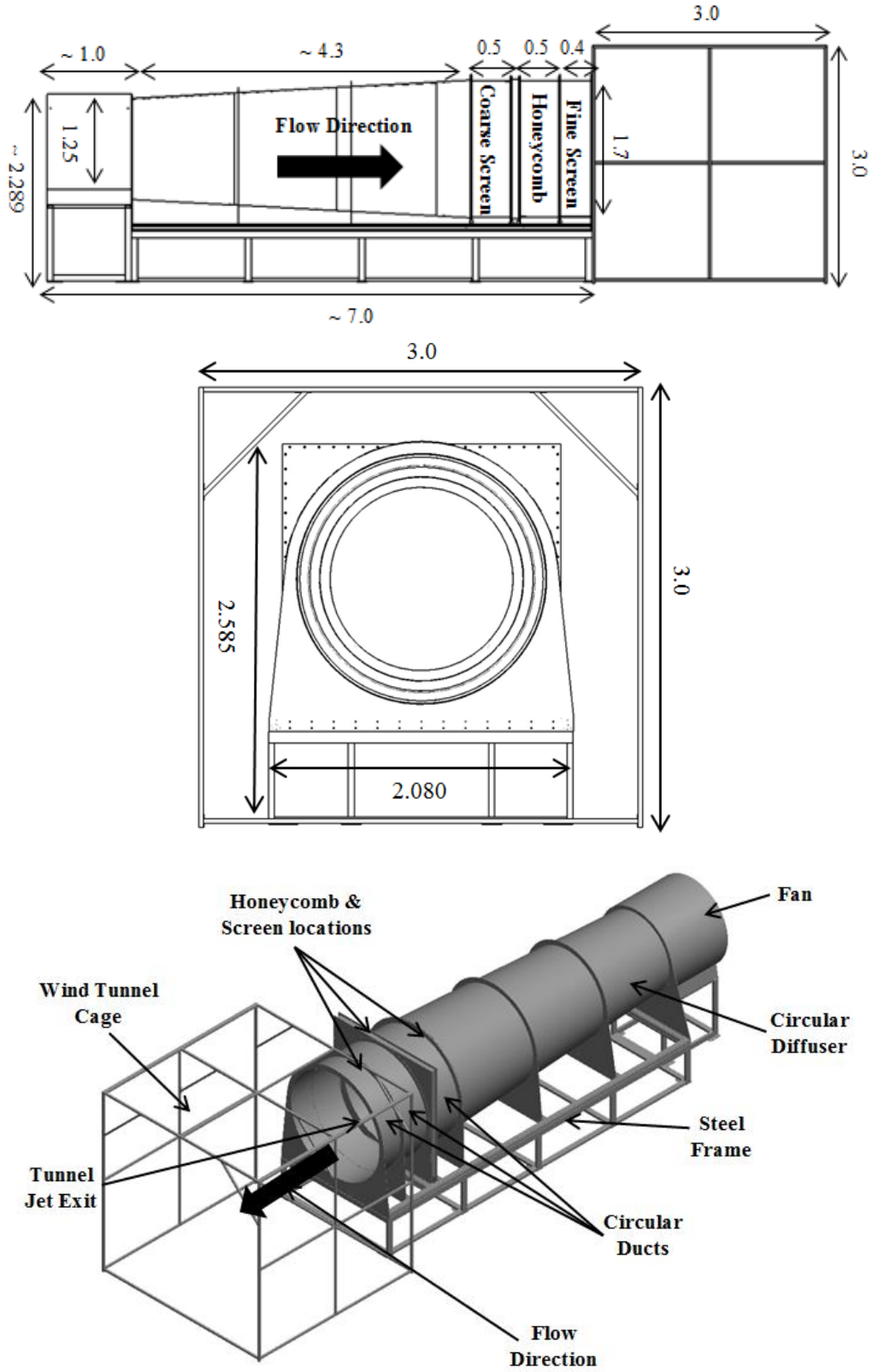

Figure 2.6: Final layout of the wind tunnel dimensions and the 3D Rendered design of the wind tunnel. Dimensions are in meters and the solid black arrow marks the flow direction

Figure 2.7: Different views of the wind tunnel after production

2.1.4. Wind Tunnel Characterization

In this section a characterization study is performed for the open jet wind tunnel at different selected wind tunnel motor frequencies. In order to check the boundary layer thickness and flow uniformity at the exit of the wind tunnel, instantaneous velocity measurements are performed using a single sensor hot-wire driven by a Constant Temperature Anemometer (CTA) system.

Figure 2.8 presents the general coordinate system definitions used in the current measurements. The hot-wire sensor is calibrated before each measurement in order to avoid any inaccuracy due to temperature changes. For this purpose a reference velocity probe is used for calibrating the hot wire sensor.

The calibration is conducted inside a subsonic suction type wind tunnel (with TI<1%) located at the aerodynamics lab of METU Center for Wind Energy (METUWIND) as shown in Figure 2.9. Calibration of the hotwire is done at an ambient temperature of 19.5^0C. The data were collected at a sampling rate of 5 kHz for 2 seconds using NI-9741 DAQ system driven by a LabView program through a PC.

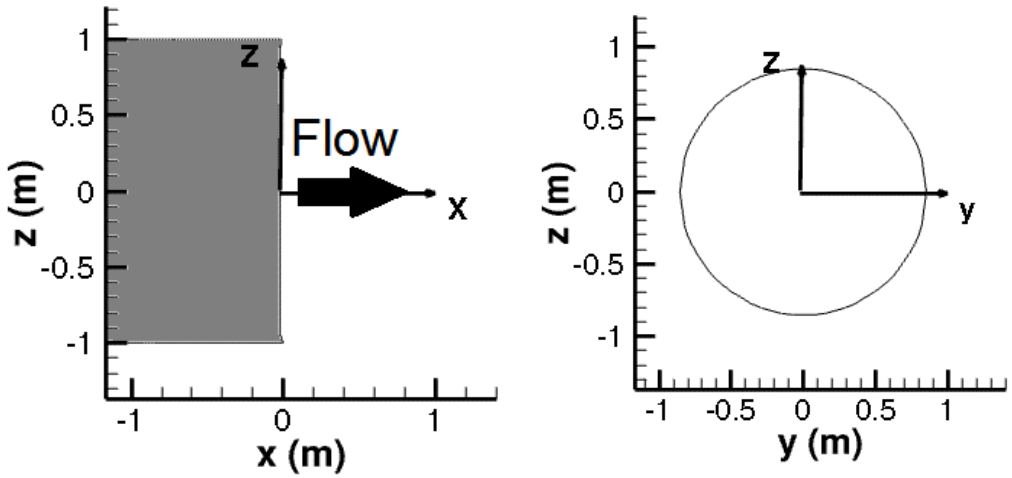

Figure 2.8: Coordinate system definitions used in the wind tunnel characterization and other measurements

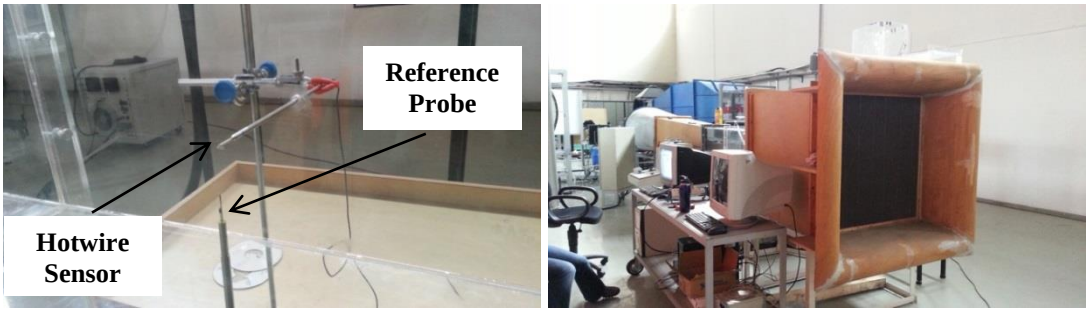

Figure 2.9: Hot-wire sensor and reference velocity probe inside the test section (left), Wind tunnel used for calibration (right)

Figure 2.10 shows the mean velocity and turbulence intensity at the jet centerline $(y,z)=(0,0)$ for different wind tunnel motor frequencies. Results shows that the maximum velocity that can be reached by the open jet wind tunnel is around 10 m/s, and the average turbulence intensity is around 2 %.

In addition, measurements have been conducted at the exit plane of the open-jet wind tunnel in the y & z directions. Measurements have been conducted at two selected motor frequencies (25 Hz represented by the square symbols & 35 Hz represented by the triangle symbols). The data were acquired by traversing the hot-wire sensor along the y-axis and z-axis using 3-axis traverse system shown in Figure 2.11. Figure 2.12 and Figure 2.13 respectively present the mean axial velocity and turbulence intensities for the two selected motor frequencies.

The results of the characterization show that the flow is quite uniform away from the walls and around the jet centerline. The boundary layer thicknesses are below 7 mm (0.4% D) and the turbulence levels are around 2.5%.

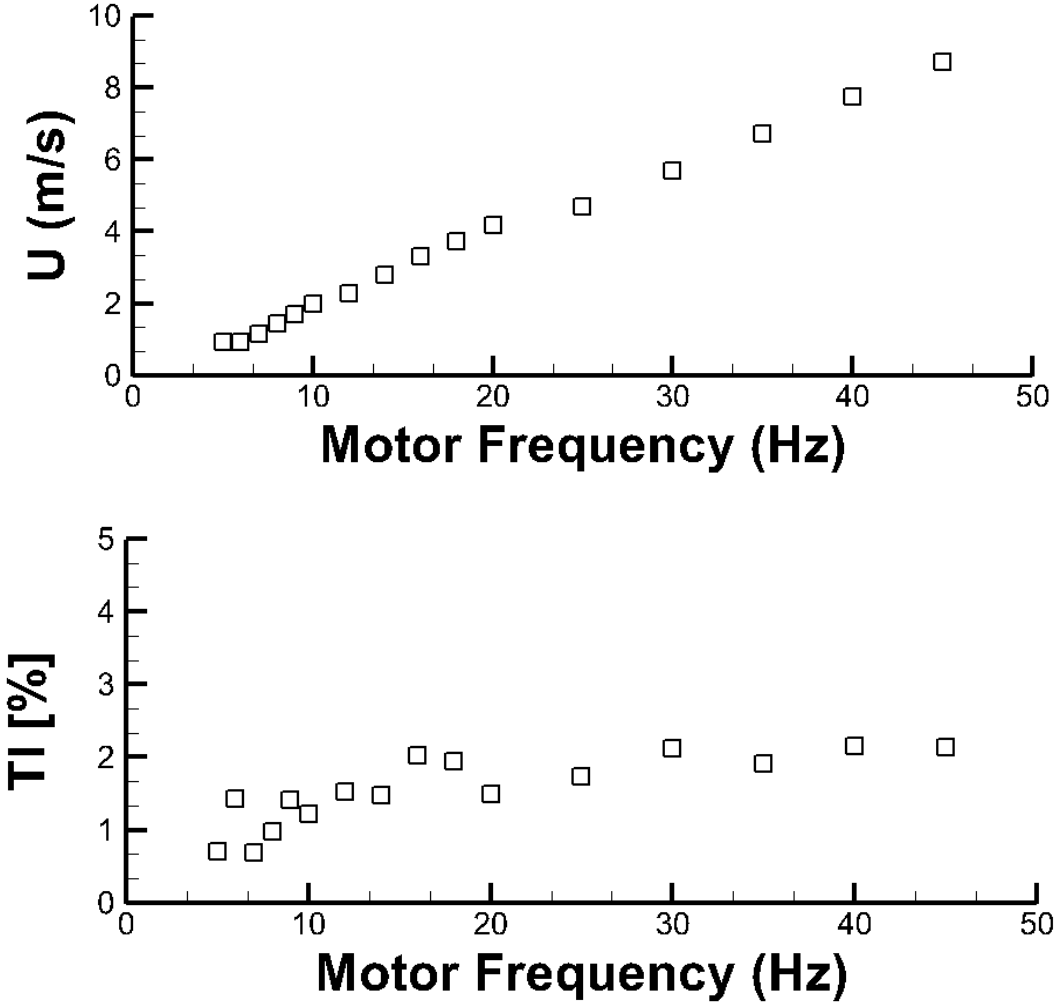

Figure 2.10: Mean axial velocity (left) and turbulence intensity (right) at the jet center line $(y,z)=(0,0)$ for different wind tunnel motor frequencies

Figure 2.11: Hotwire sensor and reference velocity probe at the jet centerline (left), wind tunnel setup with 3-axis traverse system (right)

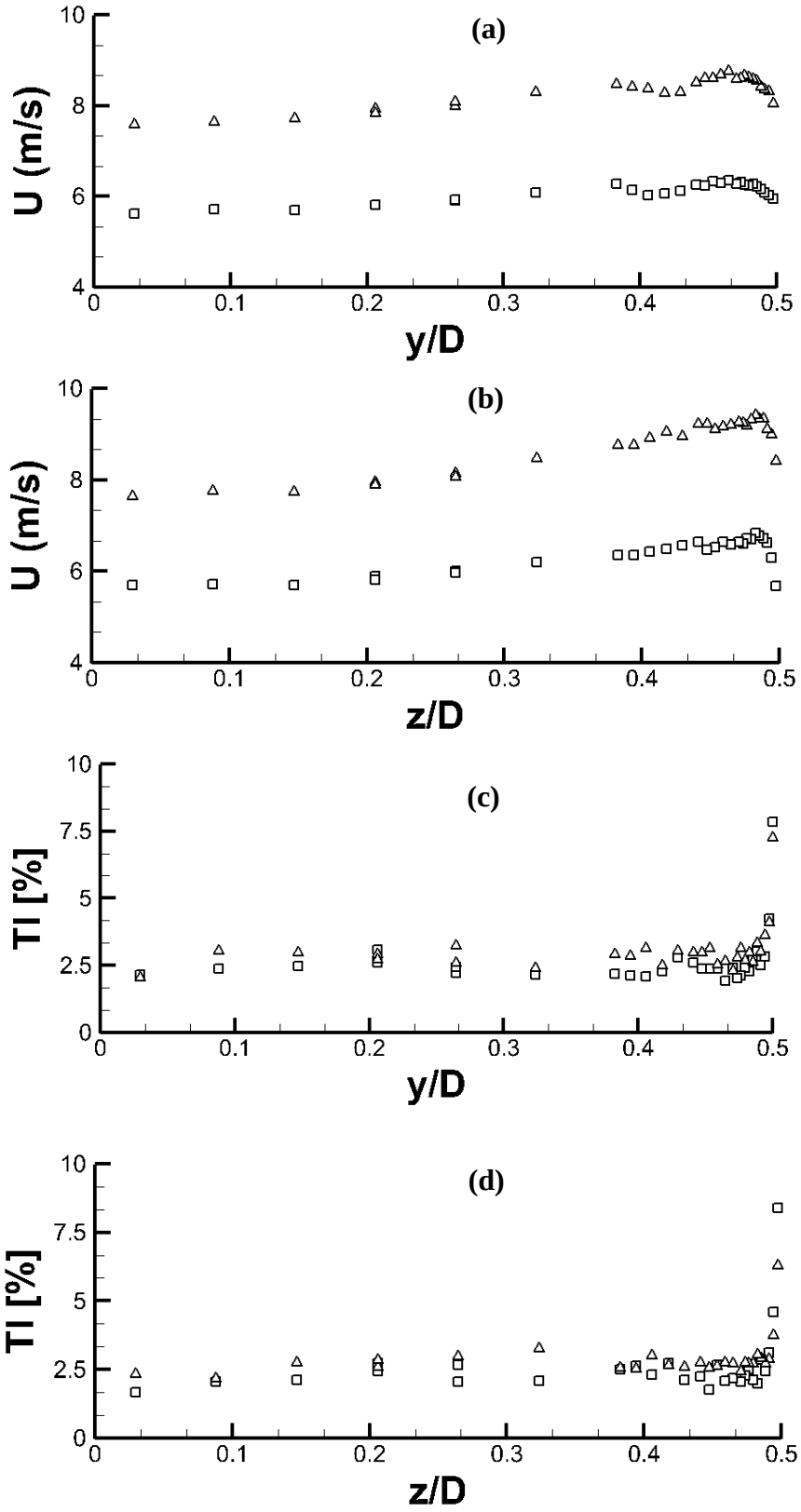

Figure 2.12: Mean axial velocity (a, b) and turbulence intensity (c, d) variations at the jet exit plane of the open-jet tunnel. Squares (□) and triangles (Δ) represent the motor frequency at 25 Hz and 35 Hz respectively

2.2. MODEL HORIZONTAL AXIS WIND TURBINE (HAWT)

The main purpose of this study is to conduct an experimental investigation of the effects of tip injection on a model wind turbine performance and wake characteristics. Therefore, the model wind turbine is specifically designed and produced to meet the conditions needed to successfully conduct the experiments. This section presents the design and production process of a model horizontal axis wind turbine.

2.2.1. Model HAWT Design

The model wind turbine used in the experiments has a 0.95 m diameter 3-bladed rotor with non-linearly twisted and tapered blades that have NREL S826 profile as shown in Figures 2.13 & 2.14. The rotational speed of the turbine is controlled by a 1.5 kW Panasonic AC servo motor and it is equipped with an HBM T20WN/5 Nm torque transducer that measures the torque and rpm. In addition, an ATI six axis F/T transducer that measures the thrust and side forces on the turbine rotor has been installed between the tower and nacelle. The nacelle, hub and the blades are specifically designed to allow pressurized air to pass through and get injected from the tips while the rotor is rotating. This pressurized air is supplied by an air compressor connected to a mass flow meter to measure the injected mass flow rate.

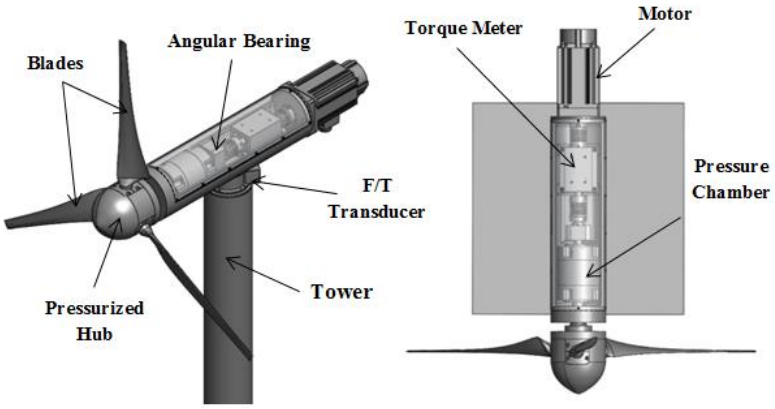

Figure 2.13: Model Horizontal Axis Wind Turbine (HAWT) components

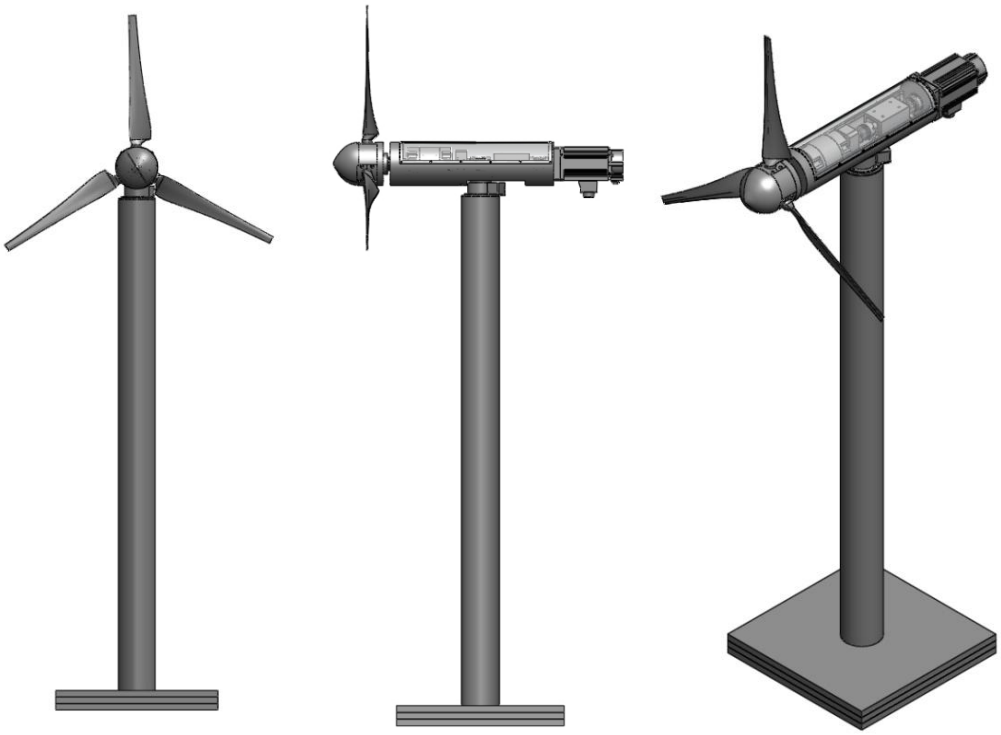

Figure 2.14: Different views of the model HAWT

2.2.2. Injection System

The injection system in the model wind turbine consists of a pressure chamber, a hollow shaft located inside the nacelle, a pressurized hub as well as blades with flow channels along the span embedded within the blade geometry to allow pressurized air to get injected from the tips of the blades during rotation. The pressure chamber (shown in Figure 2.15) is sealed with rotating mechanical seals, which allow rotation of the shaft passing through this chamber and also prevent air leakage. Moreover, radial bearings are also integrated inside the pressure chamber in order to carry its weight and avoid any stress on the mechanical seals.

Furthermore, the connections between the shaft and the hub as well as the connections between the hub and the blades are also sealed with appropriate O-rings to prevent air leakage during air injection. The pressurized air for the injection system is supplied from outside and is connected to the pressure chamber with

pneumatic quick connect interfaces as presented in Figure 2.15. After the pressurized air comes into the pressure chamber, it passes through the air transfer holes on the hollow shaft (shown in Figure 2.16) and is delivered to the pressurized hub (shown in Figure 2.17). After it passes through the hub, the pressurized air is transferred through the embedded channels inside the blades and finally gets injected from the tips of the blades (shown in Figure 2.22).

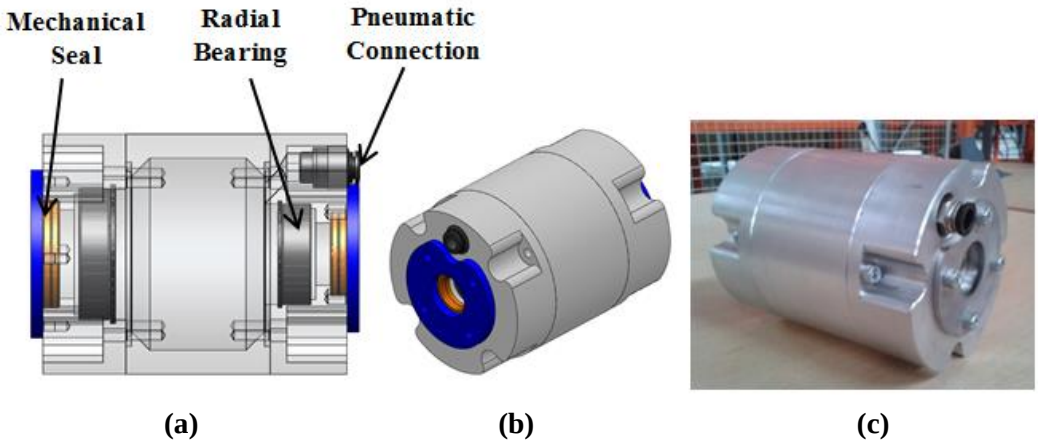

Figure 2.15: (a) Internal components of the pressure chamber, (b) rendered CAD of the pressure chamber, and (c) pressure chamber after production

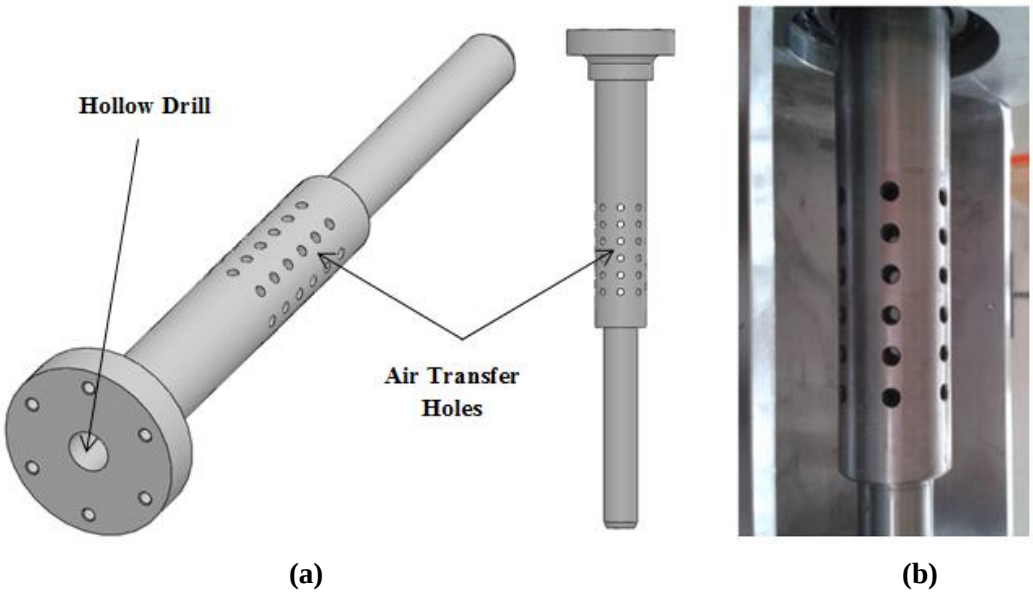

Figure 2.16: (a) Rendered CAD of the hollow shaft, (b) hollow shaft after production

(a) **(b)**

Figure 2.17: (a) Rendered CAD of pressurized hub, (b) pressurized hub after production

Figure 2.18 explains how the injection system operates, describing how the air is being supplied to the wind turbine until it is injected from the blade tips while the turbine is rotating.

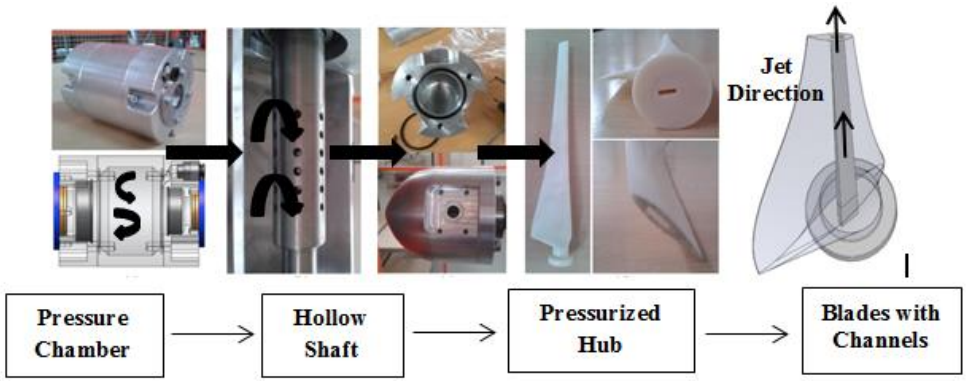

Figure 2.18: Injection system operation: air transfer through the model wind turbine components. Solid black arrows indicate how air flows through the system

2.2.3. Wind Turbine Blades

As mentioned above, the model wind turbine is equipped with blades that have standard NREL airfoils of the type S826 with a 14% thickness. The chord length distribution and the twist of the rotor blade are designed according to a standard blade element momentum (BEM) method [49]. Figure 2.19 present the chord and twist distributions of these blades taken from Karlsen [50].

The profile which features a separation ramp at the back is designed for a Reynolds number of $\mathrm{Re} = \frac{\omega R c}{\upsilon} = 2 \times 10^6$ to give maximum lift [49]. According to Krogstad and Lund [49], the blade geometry can be characterized by a "gentle separation due to trailing edge ramp", a "rapid transition on suction side due to small radius of curvature", a "low sensitivity to surface roughness" and a "strong separation on lower side at negative angle of attack". A cross section of the NREL S826 profile is shown in Figure 2.20. Further information on the profile can be found in reference [51].

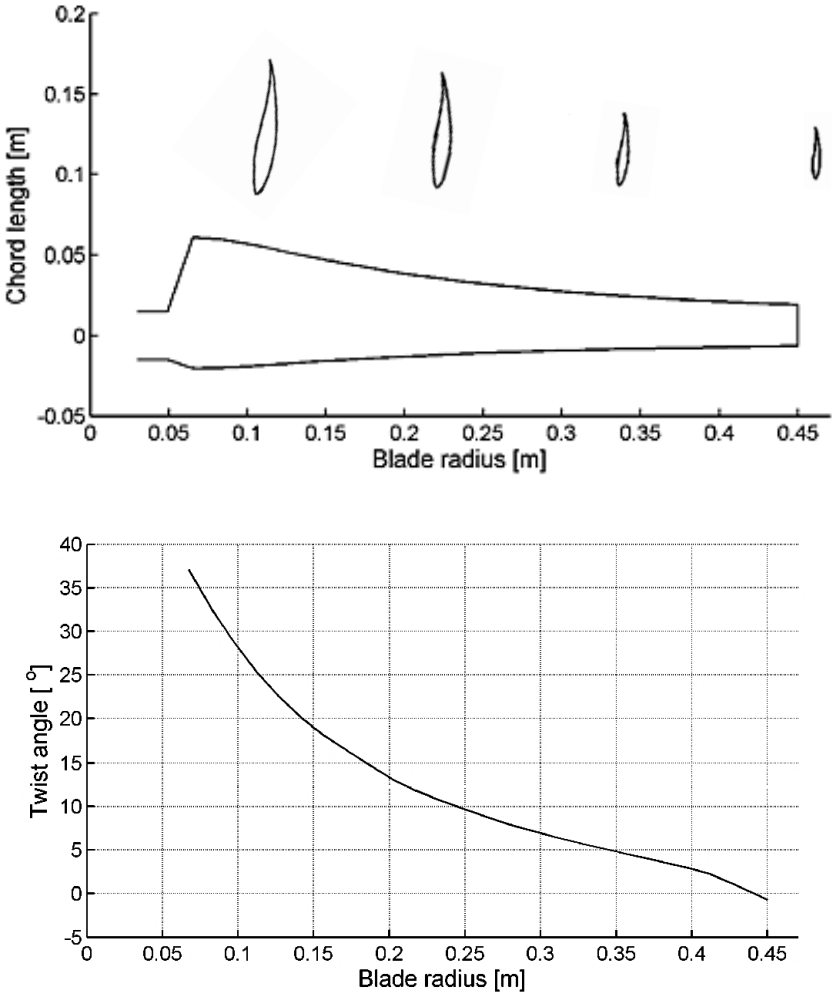

Figure 2.19: (Top) Chord length distribution and (bottom) twist angle distribution [50]

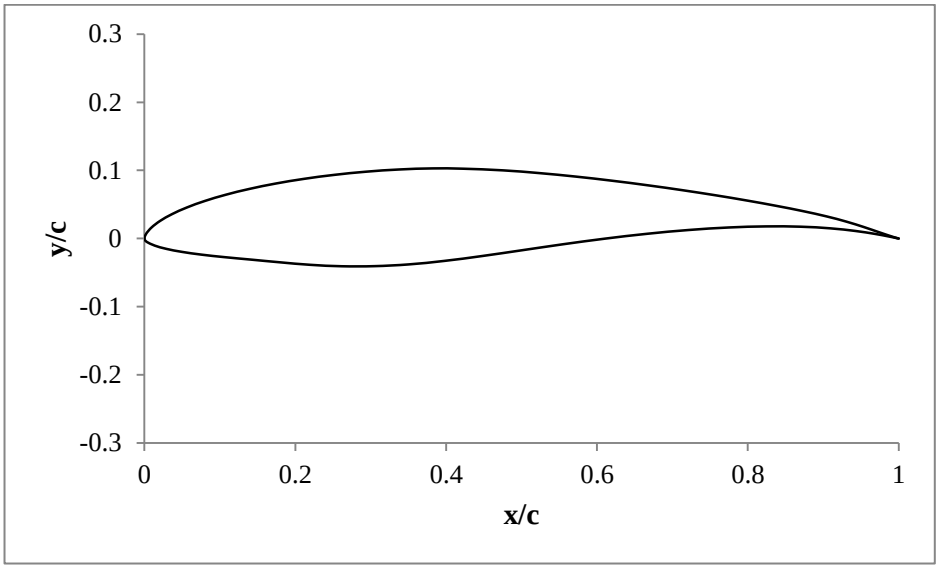

Figure 2.20: Scaled blade profile NREL S826 with 14% thickness

Figure 2.21 shows a view onto the model wind turbine blade in streamwise and circumferential projections.

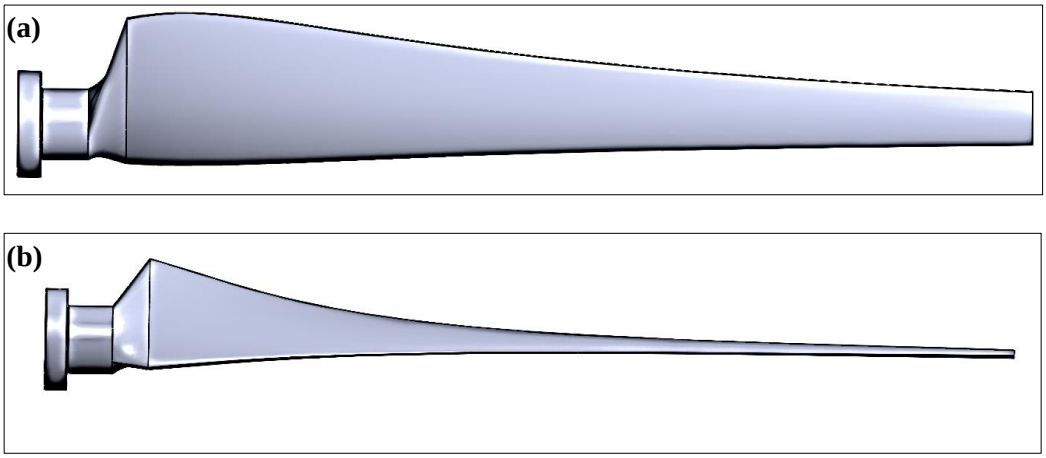

Figure 2.21: View on blade in (a) streamwise projection, (b) circumferential projection

The design of the blades has been slightly modified by adding a flow channel embedded inside the blade along the whole span. This channel has a rectangular profile and it has been twisted according to the blade profile. The blade flow channel is shown in Figure 2.22.

The blades were produced from ABS plastic using 3D rapid-prototyping technique with 0.6 mm precision. Due to manufacturing restrictions the design of the manufactured blades have a slight difference from the original ones as shown in Figure 2.22 (c). The difference appears in the trailing edge of the blade's profile. The sharp trailing edge has been modified into a circular edge with 0.6 mm diameter all along the blade span to meet the production needs.

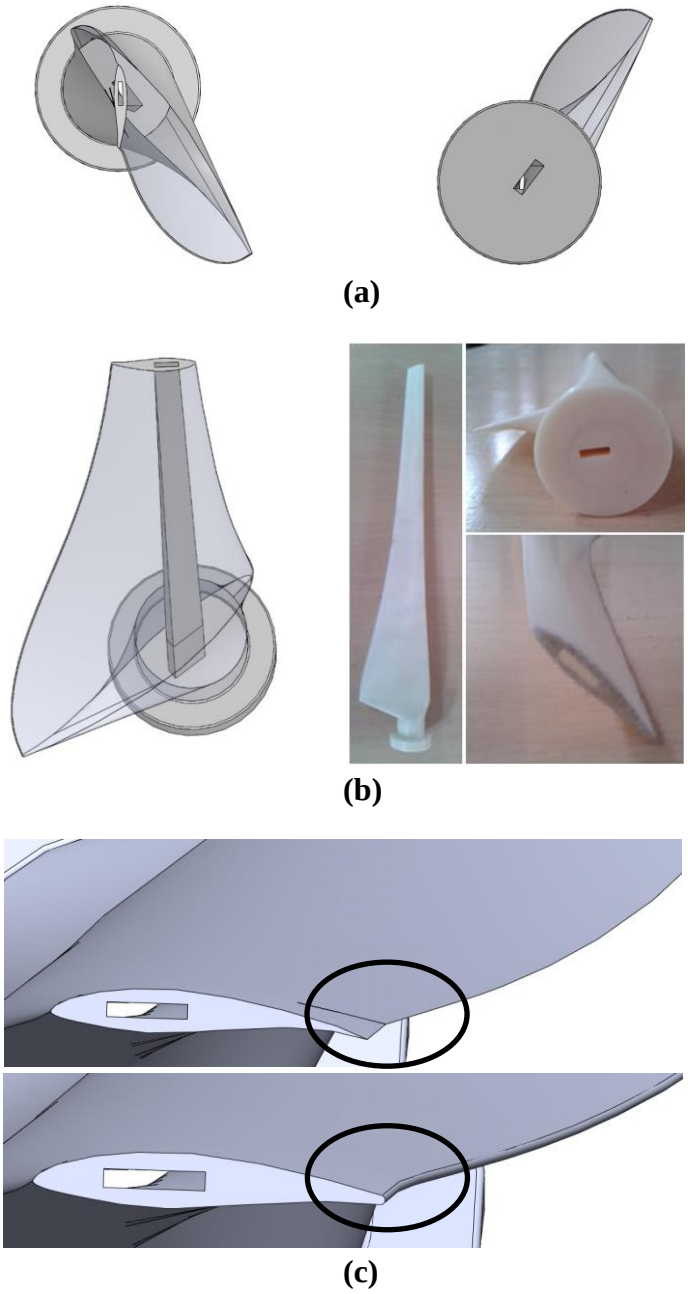

Figure 2.22: (a) cross section of the flow channel at root and tip of the blade, (b) blades after production (c) difference in the trailing edge to meet production needs

2.2.4. Final Version of the Model HAWT

Figure 2.23 and Table 2.5 show the final version and dimensions of the model wind turbine after production. The production was done using 3-axis CNC machining.

Table 2.5: Dimensions of model wind turbine components

Component	Symbol	Dimensions [mm]
Blade Span	S_{blade}	431
Hub Diameter	D_{hub}	130
Hub Length	L_{hub}	147.90
Rotor Diameter	D_{rotor}	950
Nacelle Diameter	$D_{nacelle}$	130
Nacelle Length	$L_{nacelle}$	487.55
Tower Diameter	D_{tower}	114
Tower Height	H_{tower}	1524
Foundation	-	500 x 500 mm^2

Figure 2.23: Model HAWT after production

CHAPTER 3

MEASUREMENT DETAILS

3.1. MEASUREMENT CAMPAIGNS

In this thesis study a number of test measurements on the prescribed experimental setup comprising the model wind turbine located at the exit of an open jet wind tunnel are performed. An overview of all the measurements details are presented in Table 3.1.

Performance measurement of the model wind turbine is conducted in the measurement campaigns for the baseline case as well as the injection cases. The performance measurement includes the torque and thrust data of the model wind turbine. The C_p and C_T data are obtained for the model wind turbine for different TSR and wind tunnel inflow velocities.

Furthermore, line traverses have been conducted just upstream (US) and just downstream (DS) of the rotor disk at several TSR for a single wind speed of U_∞=5 m/sec, in order to investigate the effects of tip injection on axial induction and the local angle of attack. The line traverse starts at the blade root section and extends up to 500 mm in the y-direction in step sizes of $\Delta y = 10\,mm$. The line traverses are shown in Figure 3.1.

In addition, wake measurements were conducted at the different axial stations (0.25D, 0.5D, 1D, & 2D) downstream of the turbine rotor. For each axial station the flow field is scanned in a square cross section from $z = y = 0\,mm$ to $z = y = +750\,mm$ respectively to the center of the rotor hub. The hot wire probe is

traversed in steps $\Delta z = \Delta y = 25\,mm$ in vertical and horizontal directions resulting in a measurement grid of 961 grid points per axial station for both the baseline and injection cases. The measurement grid used for the wake measurements is depicted in Figure 3.2.

Tip vortex measurements were also conducted just downstream of the rotor blade tip. The measurement plane is a 200 mm x 200 mm grid with step sizes of $\Delta x = 10\,mm$ and $\Delta y = 2\,mm$ resulting in a measurement grid of 976 grid points as shown in Figure 3.3.

Table 3.1: Measurement Campaigns

Type and location of measurement	**Resultant parameters**	**Method/ Instrument**	**Grid Size/ Step-sizes/ Measurement Points**
Performance and Wake Measurements of the Model Wind Turbine with and without Tip Injection			
C_P and C_T variations with TSR at three different inlet wind speeds	C_p, C_T, λ	Torque Sensor Load Sensor	-
Line traverses just upstream (US) and just downstream (DS) of rotor disk	U_m, TI	HW CTA	Δy=10 mm
Area Wake at 0.25D, 0.5D, 1D, & 2D downstream of the model turbine (Parallel to rotor plane)	U_m, TI	HW CTA	600 mm x 600 mm Δy=Δz=25 mm 961 points
Near flow field measurement just downstream of the blade tip	U_m, TI	HW CTA	200 mm x 200 mm Δx=10 mm Δy=2 mm 976 points

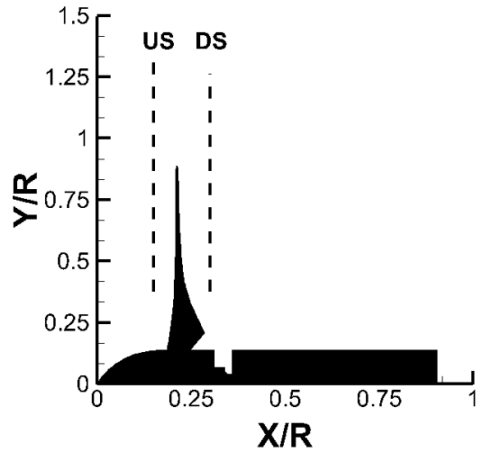

Figure 3.1: Line traverse locations upstream (US) and downstream (DS) of the rotor disk

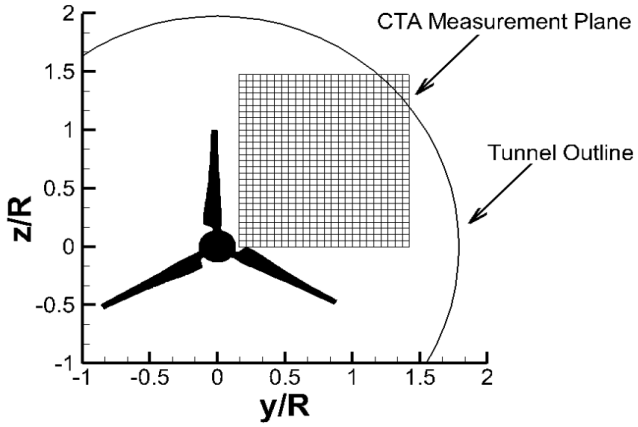

Figure 3.2: Wake area traverse measurement plane downstream of the rotor

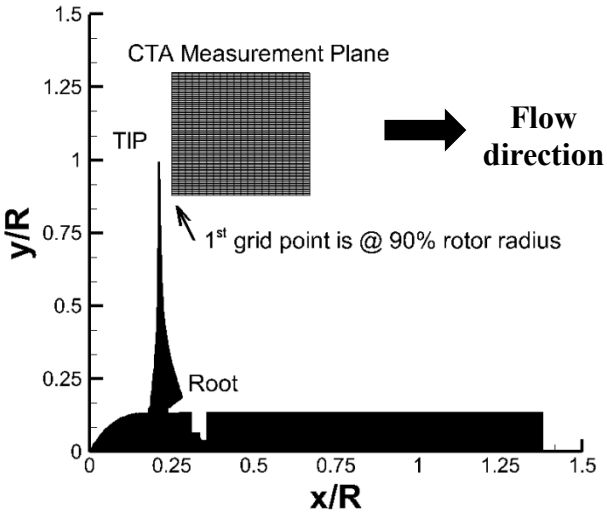

Figure 3.3: Near tip traverse measurement plane just downstream of the blade tip

3.2. DATA ACQUISITION

3.2.1. Evaluation of Frictional Torque on the shaft

Various mechanical elements that are placed on the shaft between the turbine rotor and the torque transducer such as the Pressure Chamber (PC), seals, bearings and couplings generate a resistive frictional torque on the system. Since these elements are placed between the turbine rotor and the torque transducer, the measured torque from the transducer includes these effects and it has to be corrected appropriately to obtain the actual torque of the turbine rotor only. Normally the frictional torque generated by the bearings and couplings is small compared to the torque of the turbine rotor and is generally neglected. However, in the current test setup a significant amount of frictional torque is generated by the PC mainly due to the existence of contact rotary seals embedded inside to prevent the air leakage from the pressure chamber. Furthermore, the frictional torque characteristics of these seals (therefore the PC) change with rotational speed and the air pressure level inside the pressure chamber. So for every measurement condition, i.e. rotor rpm and amount of injection level, one has to determine the actual frictional torque on the shaft generated by the PC and correct the torque measured by the torque transducer accordingly. Figure 3.4 shows a Free Body Diagram (***FBD***) of the setup showing the various torque components acting on the system.

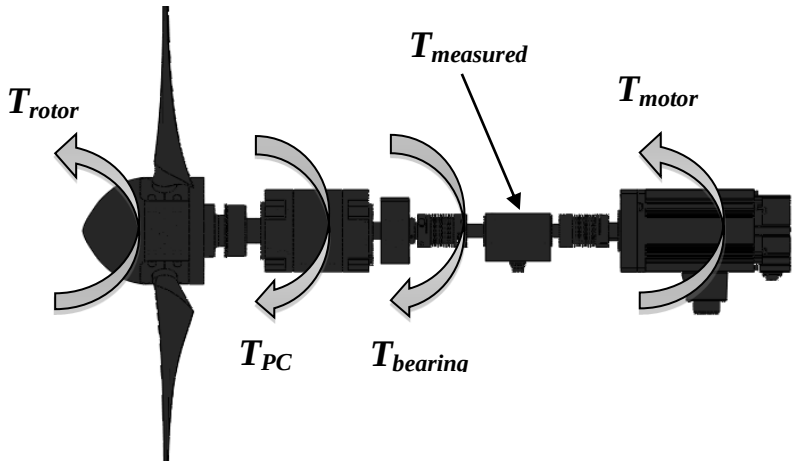

Figure 3.4: Free body diagram (FBD) showing various torque components acting on the shaft

For this purpose, several measurements are performed to determine the variation of the frictional torque generated by the PC with rotational speed for injection and no-injection cases. These measurements are obtained at no wind conditions just by running the turbine rotor with the motor. Figure 3.5 shows the variation of the friction torque measured by the torque transducer with rotational speed when the PC is installed for no-injection and injection cases. These frictional torque data are used for correcting the measured torque to obtain the actual torque of the turbine rotor.

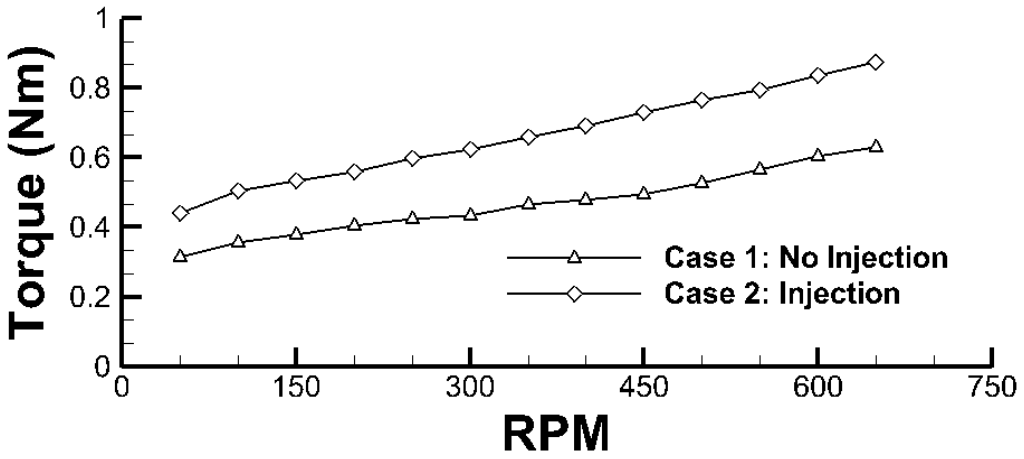

Figure 3.5: Frictional torque variation for no wind conditions at selected RPM

3.3. CONTROL SYSTEM

The rotational speed of the wind turbine rotor has been controlled by a Panasonic AC servo motor as mentioned previously. The motor has been connected to a NI motion control assembly consisting of a Compact RIO-9076 DAQ system through a NI-9512C Axis stepper drive interface module that is connected to AC servo motor through NI9930P motion control accessory in order to control the motor characteristics through a LabView program. The setup for the motor system is shown in Figure 3.6 & Figure 3.7 respectively.

A second alternative to control the servo motor is by building a breadboard in order to supply an input voltage to the motor driver, the input voltage is controlled by a wheel as shown in Figure 3.7 (a).

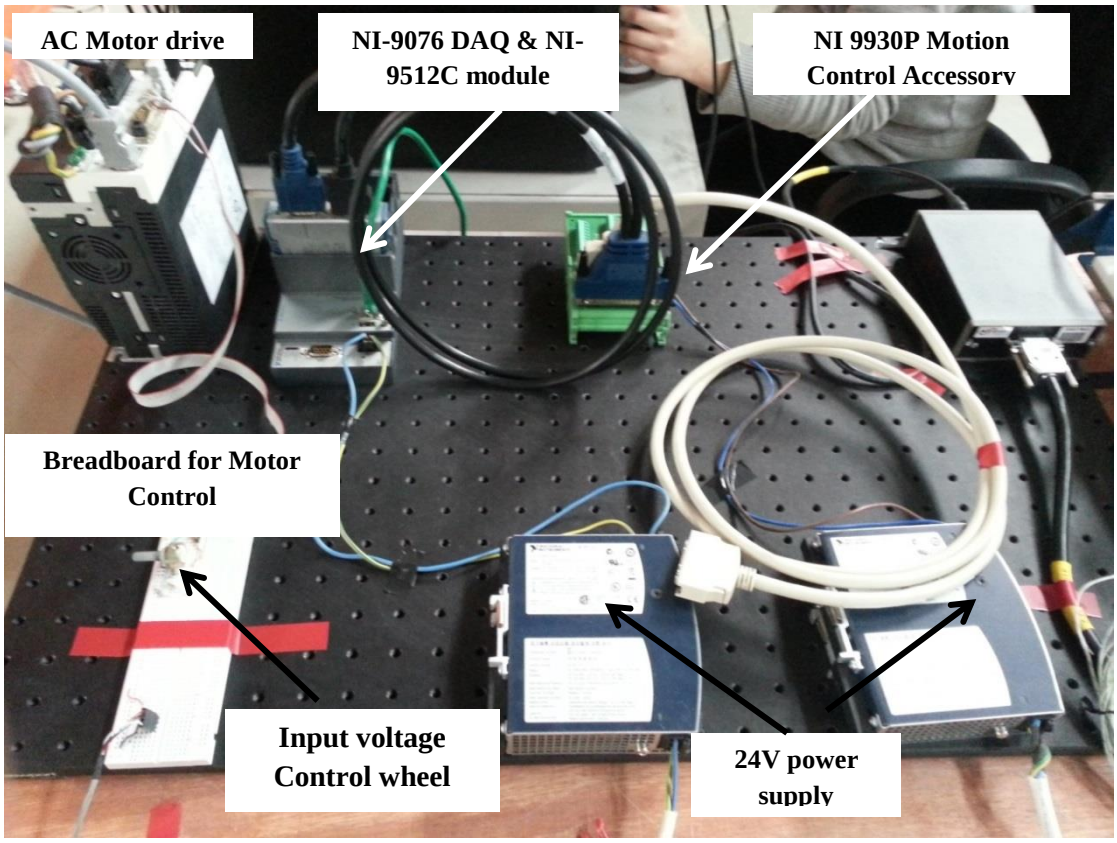

Figure 3.6: National Instruments motion control assembly

The torque meter and the F/T transducer have been connected to NI DAQ-9172 system through an NI-9205 analog input module with 250kS/s aggregate sampling rate and controlled by a LabView program through a computer as shown in Figure 3.7 (b). Data for the F/T sensor have been collected at a sampling rate of 10 kHz for a sampling duration of 30 seconds, whereas the torque sensor data have been collected at a sampling rate of 5 kHz for a sampling duration of 30 seconds.

The motor, torque sensor as well as the F/T sensor have been connected to a DC power supply voltage in order to operate properly as shown in Figure 3.7 (c). The torque sensor is also connected to an oscilloscope in order to measure the rotational speed as well as the phase angle that generate a square signal as shown below.

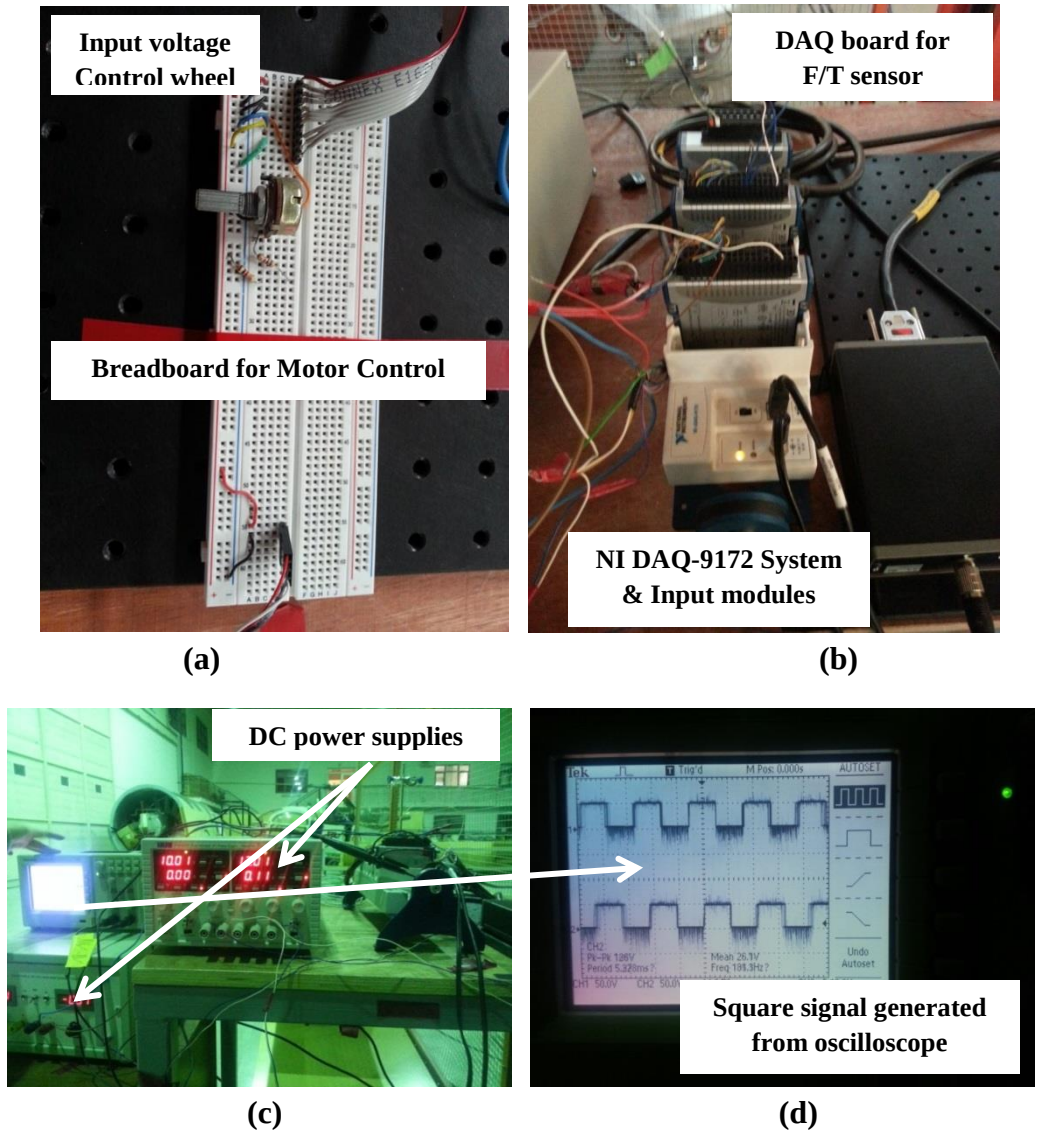

Figure 3.7: Control System: (a) Servo motor breadboard controller, (b) NI DAQ system for torque and load sensors data collection, (c) DC power supplies and Oscilloscope, (d) Square signal generated from Oscilloscope to measure RPM and Phase angle

3.4. CONSTANT TEMPERATURE ANEMOMETRY (CTA)

Line traverses and wake measurements have been conducted using a single sensor hot-wire probe driven by a Constant Temperature Anemometry (CTA) system. Dantec Dynamics Type 55P11 hot-wire probe were used, which have a 5 μm diameter Platinum plated tungsten wire. The active sensor length is 1.25 mm. Hot-

wire probes are calibrated by means of a Dantec 54T29 calibration unit. Temperature Changes are monitored with a thermometer and the hotwire output voltages were correct accordingly. The anemometer is connected to NI DAQ-9172 system through a NI-9205 analog input module and controlled by a LabView program through a PC.

Figure 3.8 (left) shows the experimental setup used for wake area traverses mentioned previously in the measurement campaigns section. The movement of the hotwire used for collecting the data at each measurement point is controlled by a combined multi-axis traverse system as shown in Figure 3.8. Similar procedure has been followed for the tip near field flow measurement setup shown in Figure 3.8 (right).

For the wake measurements, data have been collected at a sampling rate of 5 kHz for a sampling duration of 10 seconds resulting in 50000 samples at each measurement point, whereas, for tip flow measurements data have been collected at a sampling rate of 5 kHz for a sampling duration of 4 seconds resulting in 20000 samples at each measurement point.

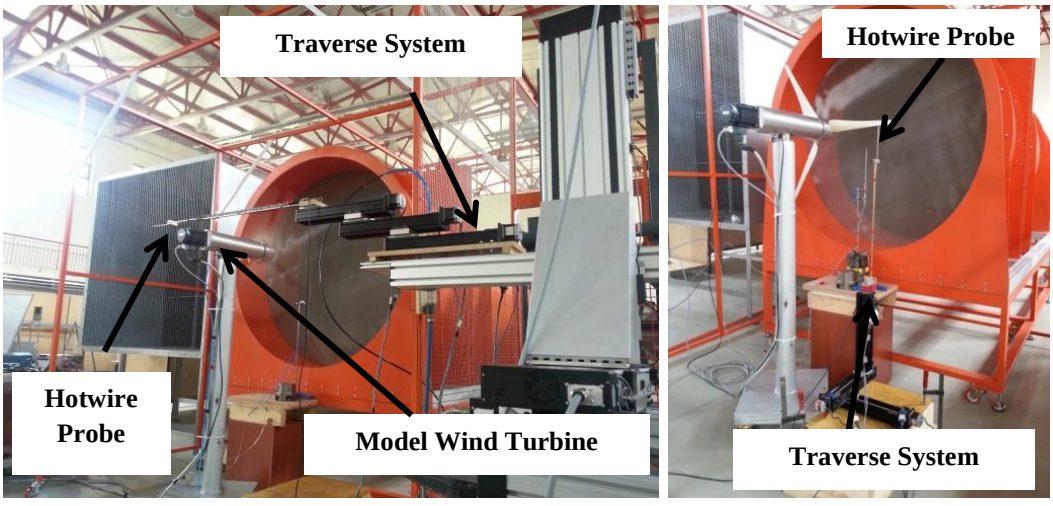

Figure 3.8: (Left) Experimental setup for area wake measurements, (right) experimental setup for tip flow measurements

3.5. UNCERTAINTY ESTIMATES

During any experiment the inaccuracies and errors arising during measurements have to be taken into account. In the present study there are several instruments and facilities used that could suffer inaccuracies. These instruments range from velocity measurements of the tunnel speed using pitot static probe, hotwire sensor driven by the CTA system during the measurement campaign conducted as well as during calibration, traverse systems used for scanning the wake measurements, the torque transducer as well as the F/T transducer could also suffer inaccuracies during the measurements. Therefore, an uncertainty estimates is a vital step during the course of this study.

Firstly, the tunnel jet exit velocity was monitored using a Pitot-static probe through Scanivalve DSA 3217 pressure scanner, which has an accuracy of 0.12%. The tunnel speed has been measured several times before each measurement, and the tunnel was kept running for 1-2 minutes before the load measurements was initiated, this gives more accurate results and prevent the inaccuracy in the jet tunnel frequency. Maximum observed difference was about 0.1 m/sec for each measurement campaign.

Secondly, the torque and F/T transducers could suffer inaccuracies as well, but based on experiments several sampling rates and number of samples have been tested in order to better quantify the errors resulting from the tests. Therefore, high sampling rate (5 kHz) and a sampling duration of 30 seconds was a good choice during data collection which resulted in less than 2% error during the measurement campaign.

Thirdly, the inaccuracies resulting during the hotwire measurements depend mainly on two factors; the ambient temperature during the experiments which is an important factor that affects the hotwire measurements. According to Jorgensen [52], a change in temperature of 1 degree can evoke an error in measured velocity of about 2%. Therefore, the ambient temperature has been monitored with a thermometer and the maximum observed difference in temperature during the wake measurements which lasted around 5 hours was less than 0.1 degrees. Also to better overcome this

problem, the temperature of the laboratory has been adjusted using an in-house heating system, and the temperature was also monitored during the course of the experiments. Another important factor is the hotwire sensor misalignment, which in many cases is neglected, if the probe head is aligned in the same way during the calibration.

Lastly, there are also errors and measurement inaccuracies occurring due to human errors, such as adjusting the turbine rotor axis with the tunnel centerline, which was done manually. Moreover, the traverse mechanisms used for hotwire movement has a resolution of 0.00635 mm for the VXM traverse system and the displacement accuracy of the TSI ISEL traverse system is $\pm 300\,\mu m$.

CHAPTER 4

RESULTS AND DISCUSSIONS

This chapter includes the results of the experiments that have been conducted throughout this thesis study. The results include performance and wake measurements of the model wind turbine for the baseline (no-injection) case as well as the injection cases. Furthermore, measurements downstream of the rotor blade tip are also included for the baseline and injection cases.

4.1. PERFORMANCE MEASUREMENT OF THE MODEL HAWT

The experiments are performed at selected wind speeds and at selected RPM values to obtain the power and thrust coefficients variations with TSR for baseline (no-injection) and for the injection case measurements. The model wind turbine is placed half a rotor diameter away from the exit of the open-jet tunnel. The center of the hub and the tunnel centerline are concentric. The blades are installed at a zero pitch angle. The turbine is rotating in counterclockwise direction.

4.1.1. Baseline (no-injection) Measurements

The power and thrust coefficient variations with TSR at different wind speeds are presented in Figure 4.1. As it can be seen from the results, the wind turbine displays expected trends in general in terms of power and thrust variations. It's known that for small wind turbines the power coefficient depends both on the wind speed and the TSR, especially at high TSR values, unlike large turbine rotors where the power coefficient is mainly a function of TSR only [53]. This characteristic is also generally

attributed to the poor aerodynamic performance due to the low Reynolds number operation of small wind turbine blades [53]. For this specific rotor, at every wind speed, as TSR increases C_P stays close to zero and almost constant up to about TSR=3. Then there is a sudden increase in C_P after TSR=3.5 and the rotor reaches the maximum C_P levels at around TSR=4.5. For higher TSR levels the C_P starts to decrease. For lower wind speeds and high TSR values, it can be seen that the power coefficient takes negative values. The main reason for this is that as the RPM increases the local angle of attack on the blades starts to get negative values. This causes the blades to produce negative lift and hence negative torque values generating the observed negative C_P values. The thrust coefficient variation as presented in Figure 4.1 shows an increasing trend with TSR as expected. Up to about TSR=4 variations for all different wind speeds collapse onto one single line. After this point deviations start to appear and as is evident at higher wind speeds the C_T value increases much faster for higher wind speeds. Note that the results get limited as TSR gets increased for high wind speeds. This was due to mainly structural integrity concerns of the current rotor blades at high RPM values.

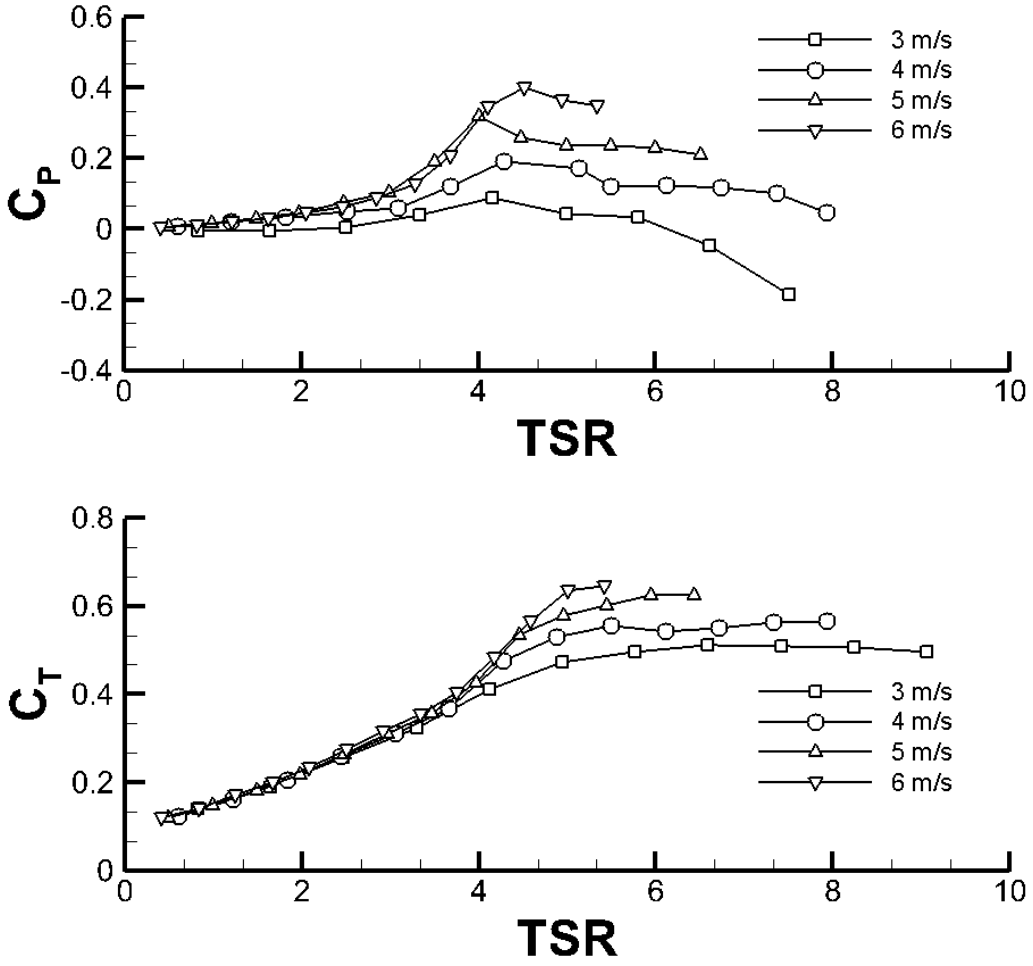

Figure 4.1: Measured power and thrust coefficient variations with TSR for different wind tunnel speeds

4.1.2. Drag due to Hub and Nacelle

One should note that the measured thrust values do include the drag due to the hub and the nacelle because of the position of the force-moment transducer. In order to quantify this influence on the measured C_T values we measured the drag of the hub and the nacelle without the blades at selected wind speeds. Figure 4.2 presents the C_T distributions with TSR with and without the drag of the hub and the nacelle. As is evident the values do get reduced slightly when hub/nacelle effect is removed. Maximum observed difference is about 13%.

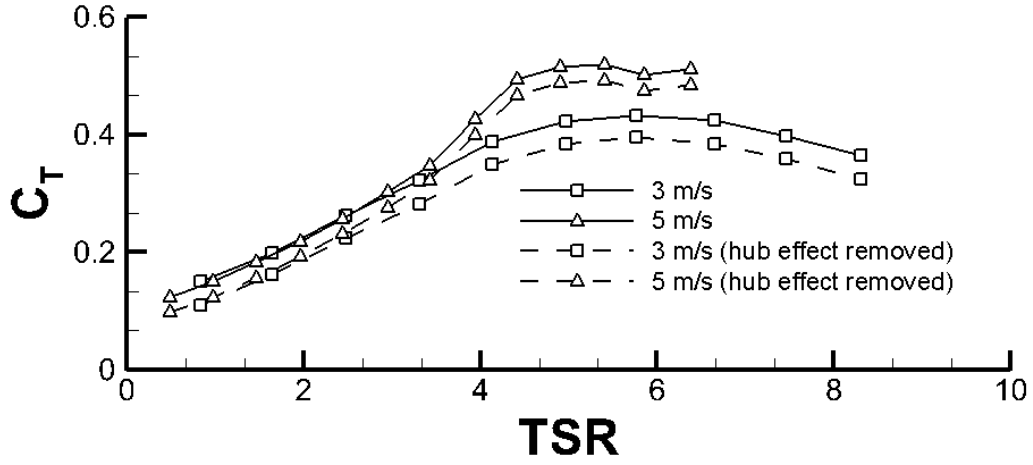

Figure 4.2: Measured thrust coefficient variations with TSR for selected wind speeds with and without the drag influence of the hub and the nacelle

4.1.3. Comparison with NTNU Data

The baseline measurement results are also compared to those obtained from the experiments conducted at the Norwegian University of Science and Technology (NTNU) using a similar turbine [4]. Both the METU and the NTNU turbines use the same NREL S826 profile as well as the same taper and twist distributions. Due to the manufacturing restrictions imposed on the METU blades because of the existence of the internal embedded flow channels, the chords of the METU blades are reduced about 0.6 mm along the span. This corresponds to a maximum difference of 25% at the tip chord compared to the NTNU turbine. The difference gets smaller as one approach to the root because of the increase in the chord of the blade. Also the diameter of the METU turbine is approximately 1% larger than that of the NTNU turbine. The main purpose of this comparison was to check the reliability and the confidence level of our test setup.

The C_p distribution comparison presented in Figure 4.3 is for a freestream wind speed of 5.8 m/s and it shows that both turbines have very similar trends in general. After TSR=3 both turbines go through a sudden increase in C_p and reaches a maximum at around TSR=4.5. The C_p values for both turbines sharply decrease after TSR=5, possibly due to laminar separation bubble on the blades caused by low

Reynolds number flow [53]. This phenomenon causes severe performance losses such as increase in drag and higher uncertainties especially for Reynolds numbers lower than 100,000. Therefore for small wind turbines the power and thrust curves become a function of both TSR and wind speed for low Reynolds numbers as explained by Probst, et al., [53]. The thrust coefficient variations presented in Figure 4.3 for both turbines also show similar trends but the METU turbine has reduced amount of thrust. The average reduction is about 35% in the thrust coefficient. The main reason behind this is the fact that the chords of the METU blades are smaller compared to those of the NTNU blades. Another reason for this reduction may be the fact that the NTNU turbine measurements are performed inside a closed test section and the blockage (wall) effects might result in an increase in thrust coefficient in comparison to the METU turbine. Note that current results get limited as TSR gets increased for high wind speeds. This was due to mainly structural integrity concerns of the current rotor blades at high RPM values.

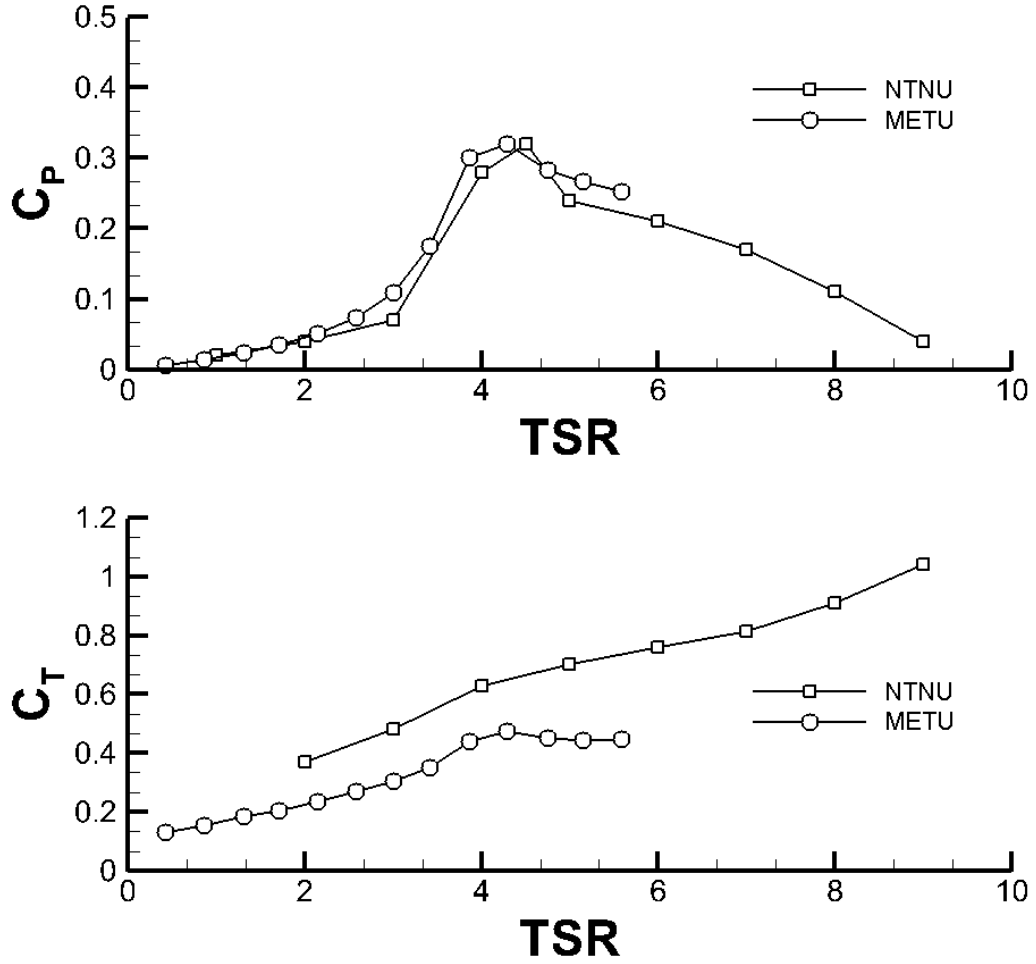

Figure 4.3: Comparison of measured C_p and C_T data with those obtained at Norwegian University of Science and Technology (NTNU) as presented in (Bartl [4]). The data presented are obtained at 5.8 m/s wind speed

4.2. MEASUREMENTS WITH TIP INJECTION

The measurements with tip injection are performed for several wind speeds and injection flow rates. Three in-flow velocities (4, 5 & 6 m/s) as well as three injection rates were selected. In order to determine the flow rate coming out from the blade tips, the velocity at the tip of each blade has been measured using a Pitot-Static probe while the turbine is stationary and this value is used for obtaining the outgoing mass flow rate from each blade. For instance, at maximum injection rate, the average injection velocity from each blade is around a 100 m/s and the velocity variation from blade to blade is less than 5%. Injection Momentum Ratio (R_M), which is defined as the ratio of the total momentum of injected air to the momentum of air going through the rotor disk (Equation 4.1), as well as the Injection Velocity Ratio (Equation 4.2), which is defined as the ratio of the injection velocity from one of the blades to the freestream wind speed (R_V), are used as indicators of the amount of injection used during the tests. The corresponding injection velocity ratios are given on the plots.

$$R_M = \frac{total\ momentum\ of\ injected\ air}{momentum\ of\ air\ going\ through\ the\ rotor\ disk} \qquad [4.1]$$

$$R_V = \frac{injection\ velocity\ \ from\ one\ of\ the\ blades}{freestream\ velocity} \qquad [4.2]$$

Figures 4.4, 4.5 & 4.6 present the measured power and thrust coefficient variations with TSR both for the baseline (no-injection) as well as for the injection cases at three different wind speeds (4, 5, & 6 m/s). The baseline cases are plotted as solid black lines with no symbols. Lines with symbols correspond to the three different injection momentum ratios. Note that these rates are slightly different for different inflow wind speeds. Results show that injection has significant effect on the power and thrust coefficients in comparison to the baseline data especially at higher TSR beyond maximum C_P TSR.

At 4 m/s (Figure 4.4) it is obvious that injection has no effect on the power and thrust coefficients for lower TSR regardless of the injection ratio used. It is also evident that for injection ratios 0.3% and 1.1%, injection has negative effects on the power coefficient and no effect on the thrust coefficient variations. Whereas, as the injection ratio increases it's clear that the power and thrust coefficients starts to increase especially for maximum C_P TSR and higher TSR values.

The case where the wind speed is 5 m/s (Figure 4.5) shows the most significant effects of injection on the power and thrust coefficients. Injection starts to take effect as one approach the TSR for maximum C_p and higher TSR values. For the thrust values injection seems to have slight effects on the entire range of lower TSR and increases significantly for higher TSR. Whereas for a wind speed of 6 m/s (Figure 4.6) the injection only have slight effect on the TSR for maximum C_p and beyond especially for maximum injection momentum ratio.

These observations can be explained as follows, for lower TSR the power coefficient shows lower values compared to higher TSR, this is due mainly to stall conditions present at this region. Therefore, when injection is applied, the local angle of attack has further increased compared to baseline case, resulting in lower lift values. Therefore, we are still in stall condition and the decrease in lift distribution which is directly related to the torque applied on the turbine rotor reflects on the lower values of the power coefficient as shown in the above mentioned figures for lower TSR region. Moreover, for higher TSR values especially the case at 4 m/s and for lower injection ratios, it is known that at this region for higher TSR the angle of attack starts to take negative values, and when injection is applied the angle of attack increases further, resulting in negative lift, which is reflected on the negative power coefficient values at higher TSR especially at 4 m/s wind speed. These observations are further explained in the following sections by observing the local angle of attack distribution at the rotor disk.

Another observation related to the significant change in the power and thrust values, is due to the increase in effective span and effective aspect ratio of the blades when

injection is applied. Previous studies have shown that spanwise blowing from the wing tips results in induced drag reduction and lift augmentation due to an increase in effective span [54 & 55].

Tables 4.1, 4.2 & 4.3 show the percentage increase/decrease in the power and thrust coefficient variations at maximum C_P TSR which is usually the design TSR. As it appears for the case at 4 m/s, the maximum percentage increase in the power and thrust coefficients occurs at an injection momentum ratio R_M=2.0% (R_V=25). Whereas, for the lower injection ratios, it's obvious that injection has negative effects on the power and thrust coefficients variations. Therefore, as we increase the injection ratio beyond R_M=2.0%, injection starts to have significant effects on the power and thrust coefficients. Similar observation could be seen for the case where the wind speed is 6 m/s (Table 4.3). However, the injection has lower effects on the power and thrust coefficients variations as compared to other cases. The case where the wind speed is 5 m/s (Table 4.2), it is obvious that the injection ratios used in the experiments have the most significant effects on the power and thrust coefficients variations for maximum C_P TSR. Therefore, it is clear that as we increase the injection ratio the power and thrust coefficient will increase as well.

The measured power and thrust coefficient variations with TSR with and without tip injection at selected wind speeds are mentioned in Table B.1 in Appendix B.

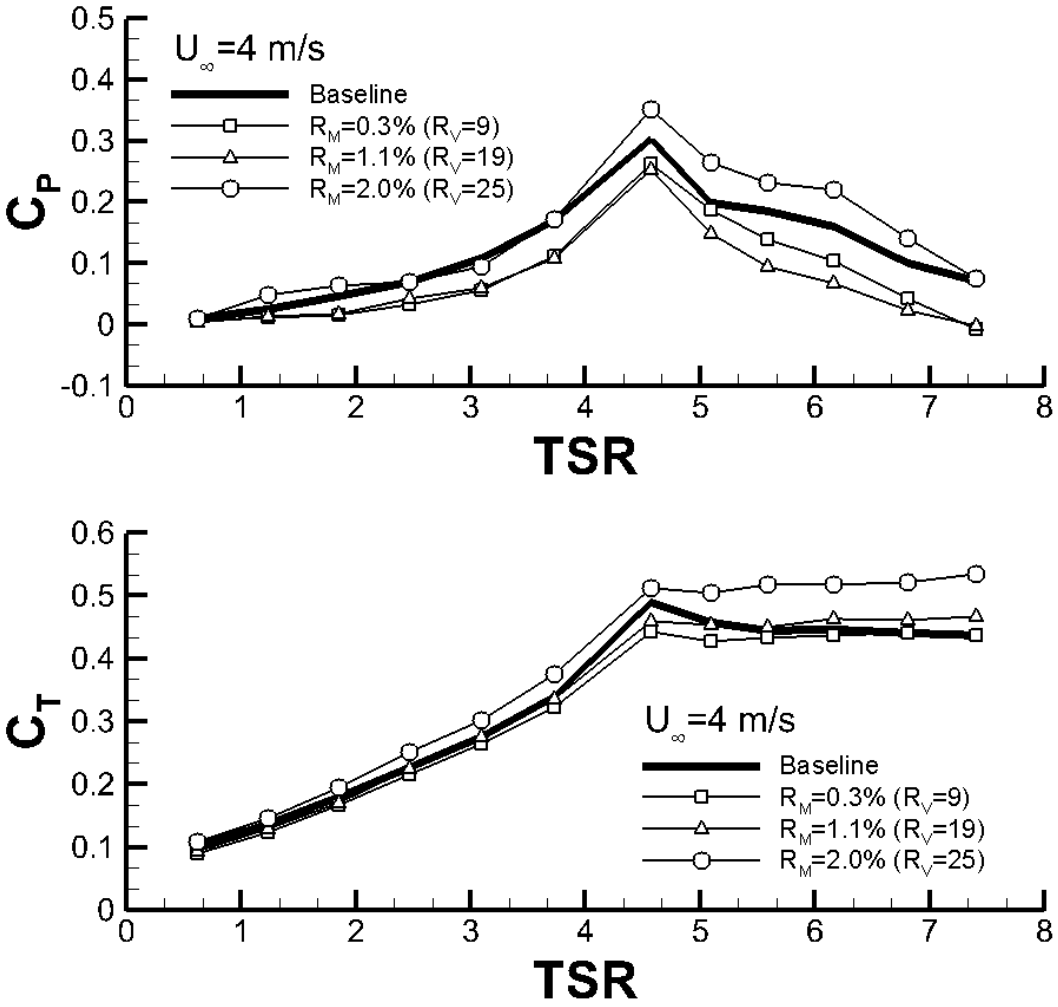

Figure 4.4: Measured power and thrust coefficient variations with TSR with and without tip injection @ U_∞=4 m/s wind speed

Table 4.1: Percentage increase/decrease in the power and thrust coefficient variations with comparison to the baseline case @ U_∞=4 m/s wind speed

	U_∞=4 m/s TSR=4.5	
	C_P	**C_T**
Baseline Case	-	-
Injection @ R_M=0.3 %	-13.6 %	-9.8 %
Injection @ R_M=1.1 %	-16.6 %	-6.0 %
Injection @ R_M=2.0 %	15.9 %	4.5 %

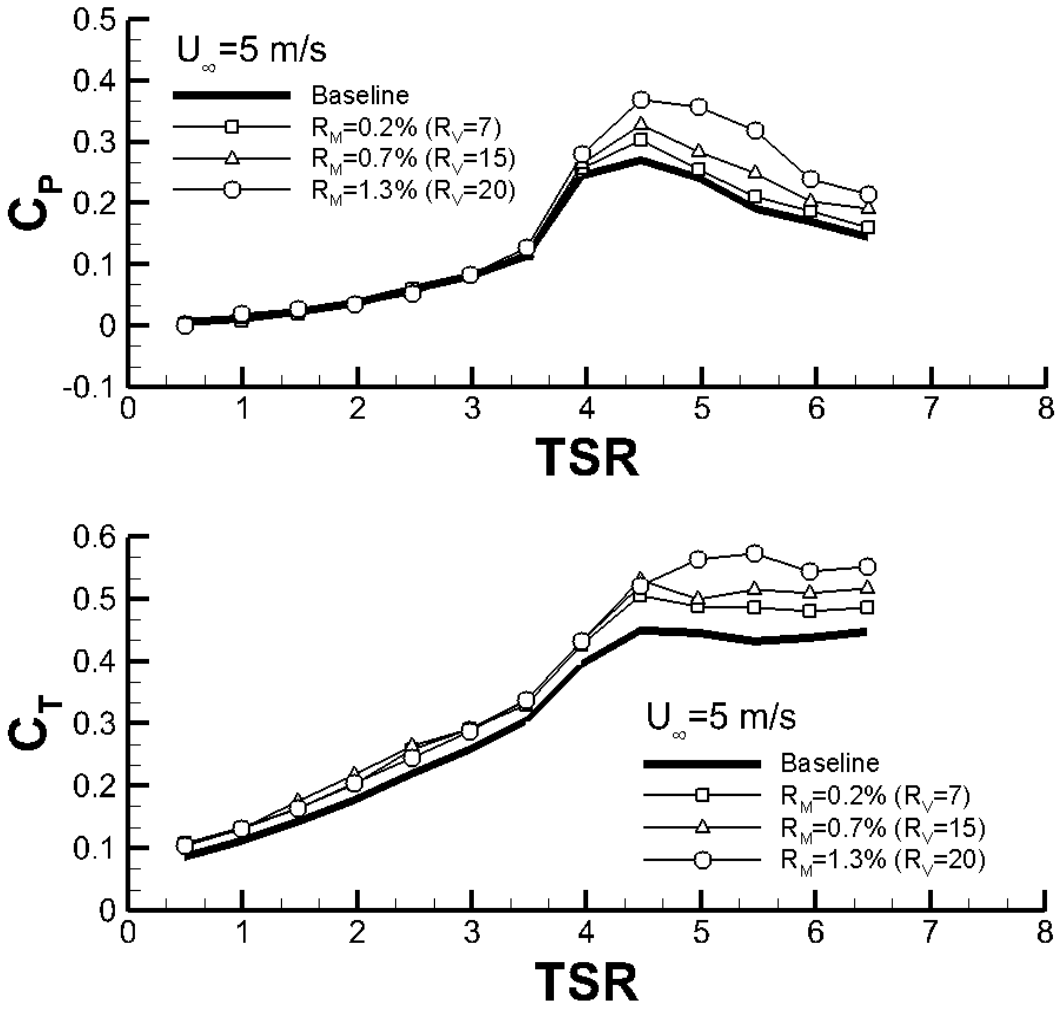

Figure 4.5: Measured power and thrust coefficient variations with TSR with and without tip injection @ U_∞=5 m/s wind speed

Table 4.2: Percentage increase/decrease in the power and thrust coefficient variations with comparison to the baseline case @ U_∞=5 m/s wind speed

	U_∞=5 m/s TSR=4.5	
	C_P	**C_T**
Baseline Case	-	-
Injection @ R_M=0.2 %	11.7 %	12.6 %
Injection @ R_M=0.7 %	21.1 %	18.2 %
Injection @ R_M=1.3 %	35.8 %	16.0 %

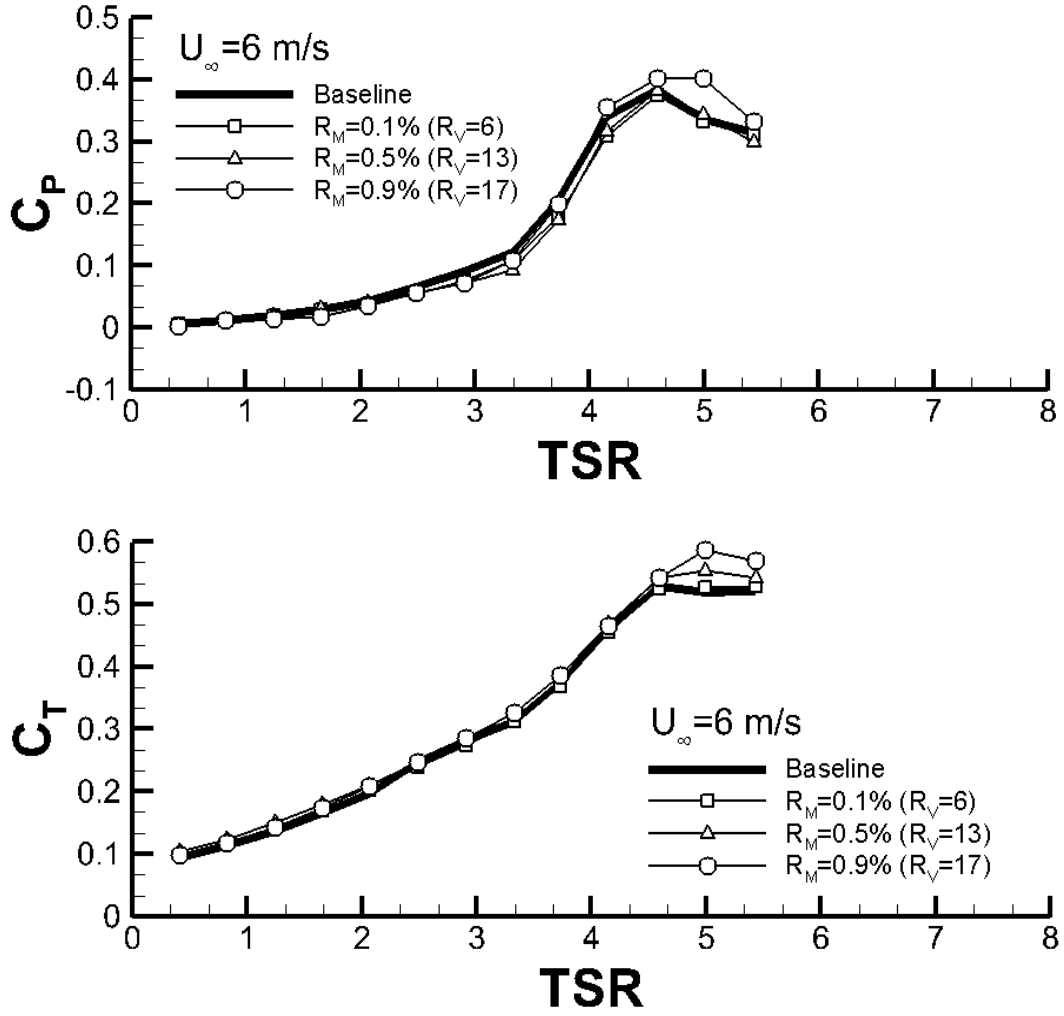

Figure 4.6: Measured power and thrust coefficient variations with TSR with and without tip injection @ U_∞=6 m/s wind speed

Table 4.3: Percentage increase/decrease in the power and thrust coefficient variations with comparison to the baseline case @ U_∞=6 m/s wind speed

	U_∞=6 m/s TSR=4.5	
	C_P	**C_T**
Baseline Case	-	-
Injection @ R_M=0.1 %	-2.3 %	-0.8 %
Injection @ R_M=0.5 %	-0.2 %	2.6 %
Injection @ R_M=0.9 %	4.5 %	2.8 %

4.3. POWER BUDGET CALCULATIONS

In order to better quantify the effects of the tip injection technique on the performance of the model wind turbine used in the experiments. A power budget calculation is a vital step in order to determine how efficient the injection is in terms of power coefficient and flow parameters.

The power budget calculation stems from the performance of the wind turbine, i.e., the power the turbine produces at the optimum TSR for a specific wind speed.

The power budget calculation is calculated for a wind speed of 5 m/sec and TSR=4.5 which produces the maximum power coefficient for both the baseline as well as the injection cases as presented in Table 4.4.

In order to calculate the power efficiency of the model wind turbine used in the experiments, one has to obtain the maximum theoretical power using Betz limit, $\left(C_{P_{\max_{theoretical}}} = 0.593\right)$ which is defined as follows:

$$P_{\max_{theoretical}} = \tfrac{1}{2}\rho U_{\infty}^{3} A_{rotor} C_{P_{\max_{theoretical}}} \qquad [4.1]$$

$$P_{\max_{theoretical}} = 31.63 \ Watts$$

Now by using the power coefficients presented in Table 4.4 we can obtain the rotor power for the baseline as well as the injection cases using the following equations:

$$P_{BL} = \tfrac{1}{2}\rho U_{\infty}^{3} A_{rotor} C_{P_{\max}} = 14.4 \ Watts$$

$$\&$$

$$P_{INJ} = \tfrac{1}{2}\rho U_{\infty}^{3} A_{rotor} C_{P_{\max}} = 19.7 \ Watts \qquad [4.2]$$

Also we need to obtain the power of the injected jet air that is the kinetic energy of the injected flow as shown in the following equation:

$$P_{jet} = \frac{1}{2}\dot{m}_{jet} U_{jet}^2 = 6.97\ Watts \qquad [4.3]$$

Details onto how the jet power is obtained are mentioned in Appendix C.

Now the efficiency of the model turbine is defined as the ratio of the maximum power achieved by the turbine at the above mentioned flow conditions over the theoretical maximum power achieved by Betz limit for both the baseline as well as the injection cases as shown in Equation 4.4.

$$Efficiency\ \ (Baseline) = \frac{P_{BL}}{P_{\max_{theoretical}}} = 46\%$$

$$\& \qquad [4.4]$$

$$Efficiency\ \ (Injection) = \frac{P_{INJ}}{P_{\max_{theoretical}}} = 62\%$$

Therefore, from the above mentioned equations one can define a power efficiency of the system describing the power budget at the given flow conditions (U_∞=5 m/sec & TSR=4.5) as follows:

This power efficiency represents how much the power has increased due to tip injection without taking into account how much power is being spent on the injected air.

$$Power\ Efficiency\ \ (PE) = \frac{P_{INJ} - P_{BL}}{P_{\max_{theoretihe}}} = 17\% \qquad [4.5]$$

Now when the power of the injected air (Equation 4.3) is taken into account, the power efficiency of the system is defined as follows:

$$Power\ Efficiency\ \ (PE) = \frac{(P_{INJ} - P_{Jet}) - P_{BL}}{P_{\max_{theoretical}}} = -5.29\% \qquad [4.6]$$

Data have been summarized in Table 4.4.

Table 4.4: Efficiency calculations @ U_∞=5 m/sec & TSR=4.5

U_∞= 5 m/sec & TSR=4.5	
$P_{max,\ theoretical}$ @ $C_{Pmax,theoretical}$=0.593	31.63 Watts
$P_{max,\ BL}$ @ $C_{Pmax,BL}$ =0.27	14.4 Watts
$P_{max,\ INJ}$ @ $C_{Pmax,INJ}$ =0.37	19.7 Watts
P_{Jet} @ R_M=1.3 %	6.97 Watts
Efficiency (Baseline)	46 %
Efficiency (Injection)	62 %
PE (No jet power)	17 %
PE (jet power)	-5.29 %

From the obtained results presented in Table 4.4, it seems that in order to increase the power by 5.3 Watts, we need to spend 6.97 Watts on the injected air, which gives 5.29% power deficiency for the process. This value means that our system is not efficient in order to obtain higher power and thrust coefficients for the model turbine since we are spending more power than we gain.

The entire aim of the study is to show whether tip injection can produce more power compared to the baseline case. Moreover, there is more into this technique than an increase in the aerodynamic loads. This is related to the wake characteristics of the model wind turbine which significantly changes due to tip injection, as well as the tip vortex characteristics as will be shown in the following sections. This change in the

flow field downstream of the wind turbine has major influences on the downstream turbines in wind farm arrangements. This is directly related to the structural fatigue life of the turbine blades as well as the performance of the downstream turbine as we can predict.

The measured and calculated values of the velocity ratios, mass flow rate ratios, as well as the momentum ratios are presented in Table C.1 in Appendix C.

4.4. INFLOW AND OUTFLOW MEASUREMENTS OF THE ROTOR

This section involves line traverse measurements conducted just upstream and just downstream of the rotor disk along the radial direction (y/R). Details are given in Table 3.1 in Chapter 3. Single sensor hot-wire driven by a CTA system was used for measuring the instantaneous axial velocity upstream and downstream of the rotor. Data have been collected by using an NI DAQ system controlled through LabView program. The sampling rate at which data were acquired is 5 kHz and the sampling duration is 10 seconds at each measurement point. The measurements with tip injection were performed at the same operating conditions for a certain injection ratio from the blade tips (R_M=1.3%) at a wind speed of 5 m/s and for 2 and 5 TSR values. The reason behind these measurements is to investigate the effects of tip injection on the axial induction and local angle of attack which seems to be the reason behind the increase in power and thrust coefficient values as mentioned earlier.

Figure 4.7 presents the measured mean wind speed distribution just in front of the rotor disk at 0.02D upstream location for TSR 2 and 5, where D is the rotor diameter. Knowing the local blade speed, twist and pitch angles, we use this distribution to estimate the local angle of attack along the span, which is presented in Figure 4.9. As one can observe, in case of injection the inflow wind speeds are slightly elevated all along the span. The average increase is around 2%. This is also reflected in the local angle of attack distribution in which a slight increase along the span is evident. Accumulative increase of local lift and drag forces due the increase in local angle of attack may be the reason behind the observed increases in power and thrust coefficients at TSR=5. Note that the angle of attack range changes between 6.5 and 10 degrees so the blade seems to operate under attached flow conditions at this TSR value, as expected. Whereas, for TSR=2 as shown in Figure 4.9 the blade is operating under stall conditions and the angle of attack range changes between 24 and 27 degrees. We have previously made 2D airfoil characterization studies of the NREL S826 airfoil at low Reynolds numbers and one can refer to (Ostovan et al. [56]) for the data.

For the case where TSR=2, results shows similar observation in terms of increased values for the wind speed and local angle of attack. As mentioned earlier for low TSR, stall conditions are present in this region which results in low power and thrust coefficients. When injection is applied the increase in local angle of attack is substantial which further resulted in decreased power coefficients. Moreover, at lower TSR the thrust coefficient seems to be slightly increased for the injection cases, the reason behind this increase may be attributed to the substantial increase in velocity magnitude downstream of the rotor near the blade tips region.

Figure 4.8 shows the average measured wind speed distribution along the span at 0.02D upstream of the rotor for 5 m/s wind speed and TSR=5. The reason behind this measurement is to check the repeatability and reliability of the measurements and to observe whether there is an actual difference between the injection and baseline measurements. The average of three measurement sets was calculated and the error between each measurement was obtained as shown by the error bars in Figure 4.8. Results show that the error is small for the baseline and injection cases, and that the observed increase in the wind speed which is also reflected on the local angle of attack distribution is mainly attributed to tip injection.

Figure 4.10 shows the velocity and turbulence intensity variations at 0.02D downstream of the rotor, with and without injection. In terms of the velocity within the wake region just downstream of the rotor disk one can observe slight increase when there is injection, consistent with the observation upstream of the rotor disk as presented previously in Figure 4.7. Near the blade tip region (y/R=1), there is a sharp change in the velocity distribution for the baseline case. Having tip injection modifies this region significantly. The momentum of the jet exiting from the blade tips generates a peak in the velocity distribution and the transition region from the turbine wake to freestream conditions occupies a wider area when the injection is applied. The turbulence intensity variation presented in Figure 4.10 (bottom) presents also dramatic changes near the tip due to tip injection. The tip jets when mixing with the oncoming freestream seem to generate substantial increases in local turbulence level showing almost 3-4 times more turbulence intensity at the peak of the

distribution. Note that the velocity and the turbulence intensity variations nicely converge on to each other for baseline and injection cases away from the tip regions within the wake and the freestream zones. From the observed velocity and turbulence intensity distributions, one can predict that the entire flow field will be significantly influenced when injection is applied especially near the tip region and for the entire wake region. This significant change is further explained in details in the following sections.

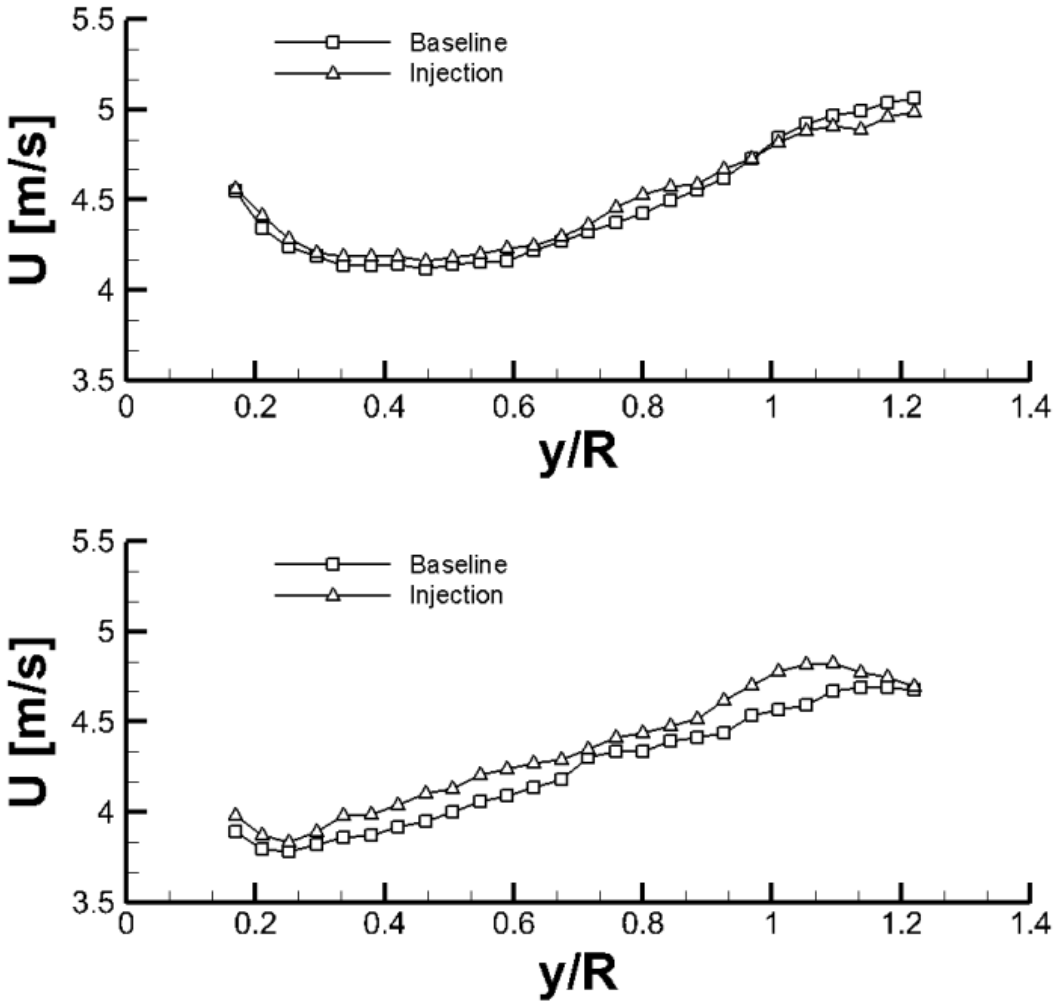

Figure 4.7: Measured wind speed distribution along the span at 0.02D upstream of the rotor: (Top) U_∞=5 m/s, TSR=5, R_M=1.3%; (Bottom) U_∞=5 m/s, TSR=2, R_M=1.3%

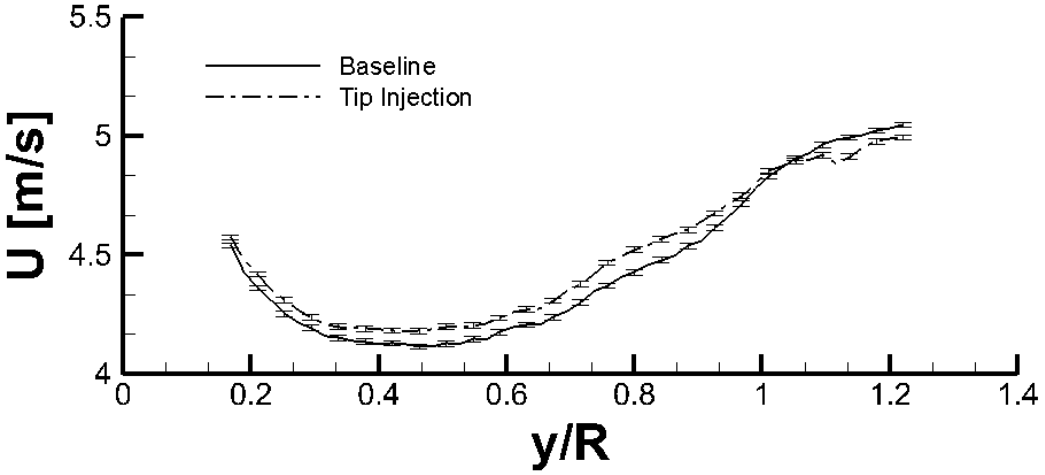

Figure 4.8: Average measured wind speed distribution along the span at 0.02D upstream of the rotor @ U_∞=5 m/s, TSR=5, R=1.3%

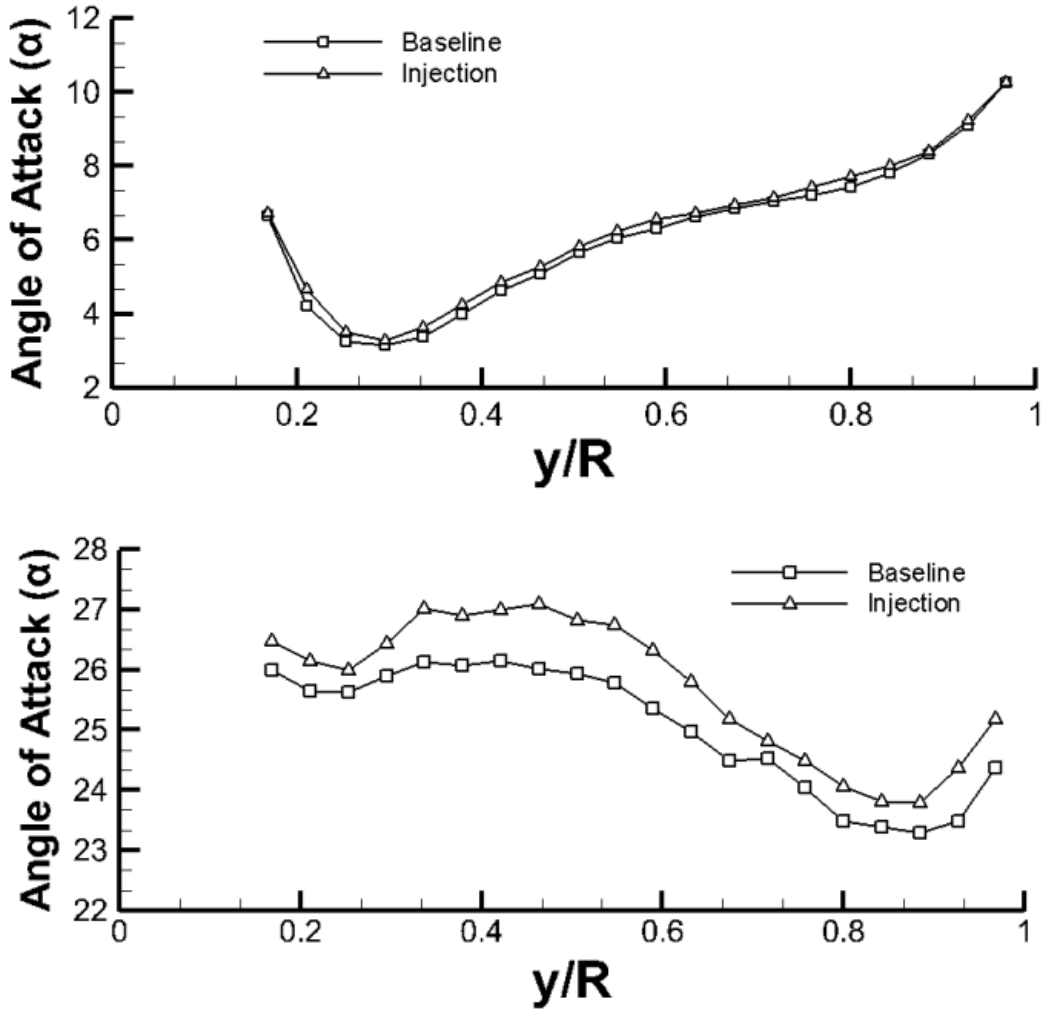

Figure 4.9: Estimated local angle of attack distribution along the blade span: (Top) U_∞=5 m/s, TSR=5, R_M=1.3%; (Bottom) U_∞=5 m/s, TSR=2, R_M=1.3%

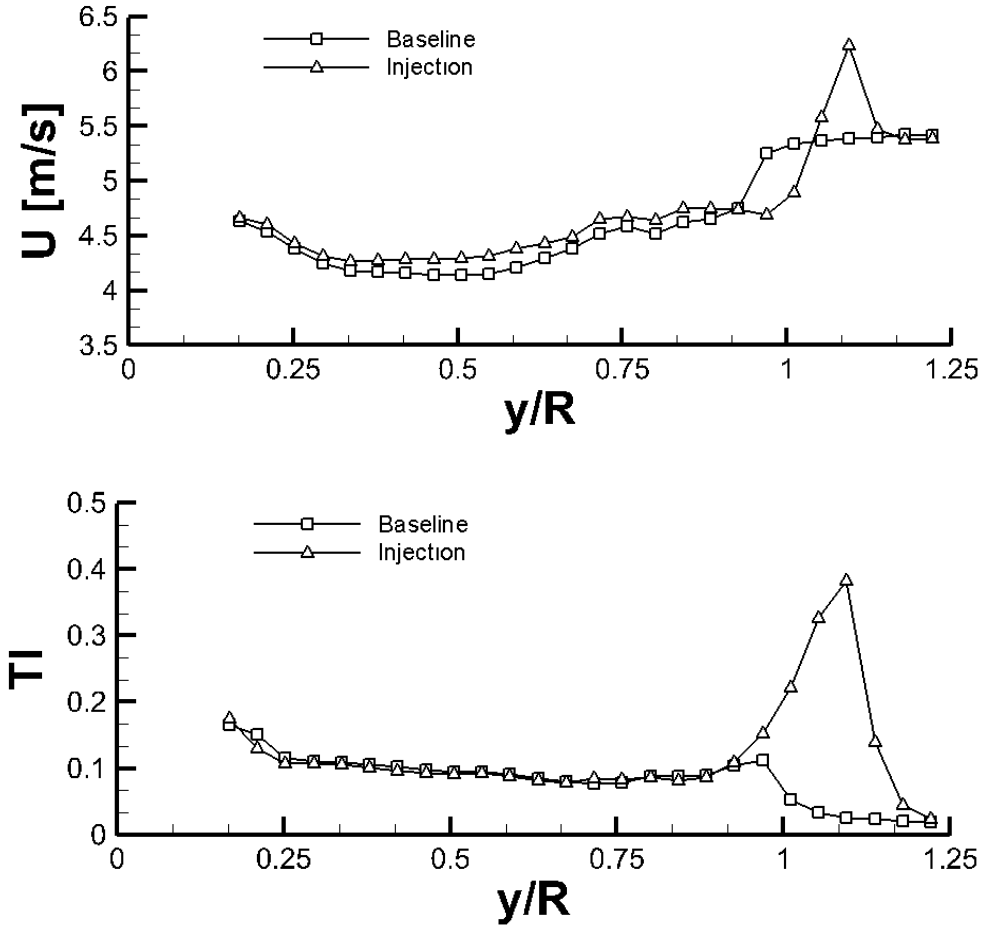

Figure 4.10: (Top) Axial velocity and (bottom) turbulence intensity variations at 0.02D downstream of the rotor, with and without tip injection. U_∞=5 m/s, TSR=5, R_M=1.3%

4.5. WAKE MEASUREMENTS

This section describes the wake measurements conducted downstream of the rotor disk. Measurements details are presented in chapter 3, describing the measurement plane and data acquisition. Baseline as well as injection measurements have been conducted at different axial locations as shown in the following sections. Figure 3.2 and Figure 3.8 (left) show the measurement plane and setup for these tests. Tests have been done at a wind speed of 5 m/s for a TSR=5 and the injection ratio used is R_M=1.3%.

Figures 4.11 and 4.12 show the velocity and turbulence intensity variations, respectively, for baseline (left column) and injection (right column) cases on 0.25D (1^{st} row), 0.5D (2^{nd} row), 1D (3^{rd} row), and 2D (4^{th} row) downstream planes. The flow is coming out of the page in these figures and the circular line marks the outline of the open-jet tunnel. In Figure 4.11 one can clearly observe three distinct regions of flow downstream of the rotor. First the wake of the rotor is evident as a low momentum zone downstream of the rotor disk. The freestream flow indicated by red color is also visible. On the top right corner one can also see the low momentum shear layer boundary of the open jet flow that is issued from the tunnel. Both for the baseline and injection cases streamwise diffusion of the wake is evident as one move from 0.25D to 2D. This is indicated by the wake zones starting to occupy wider areas as well as by the contour lines starting to get away from each other and spread more as one moves downstream.

When there is injection the tip region gets affected substantially. The low momentum zone within the rotor wake seems to widen and occupy a larger area at every streamwise location downstream of the rotor especially at 1D and 2D. Mostly affected region is off course near the tips. The relatively sharp boundary that exists in the baseline case between the wake and the freestream zones, marked by the closely packed contour lines there, seem to get more diffused and the contour lines become spread out when there is tip injection. This spreading out of contour lines exists on every one of the presented measurement planes and become very evident especially

on 1D & 2D downstream planes. This indicates that the tip injection not only affects the loads on the blades but changes the wake diffusion characteristics of the turbine, which will of course be critical in multiple turbine configurations. Another critical observation is clearly presented at 2D downstream where the velocity start to increase and the flow field starts to recover as one propagates downstream which is also critical in for downstream turbines.

Figure 4.12 presents the turbulence intensity variations on the same downstream planes for the baseline and injection cases. Three distinct high turbulence regions can be depicted: One near the hub that occurs most probably due to the root vortices shed from the blades, one near the tip clearly marking the regions occupied by the tip vortices and one at the top right corner again marking the shear layer of the open-jet flow issued from the tunnel. Note that at 1D & 2D lower left hand corner the increase turbulence levels are due to the wake region of the tower and the nacelle. The effect of injection can be observed even more clearly from these plots. First, near the blade tips the region occupied by the tip vortices seem to be pushed radially outward from the rotor disk compared to the baseline case. Second, this region is now marked with higher turbulence levels and packed with more number of contour lines indicating a wider and highly turbulent region gets generated when one applies tip injection. As one moves downstream this region gets enlarged quickly due to diffusion and starts to occupy an even wider zone at 1D & 2D downstream. The flow region normally occupied by the tip vortices get much more spread out and diffused at 2D when the tip injection is applied. At 2D downstream the flow field and especially the tip region gets entirely diffused resulting in entirely minimizing the effects of the tip vortex as compared to the baseline case. This of course is again critical especially if there is a downstream turbine, which will now be exposed to less concentrated tip vortices incoming from the upstream turbine. In addition the tip vortices are now at a different radial position and this will of course change the interaction characteristics of a downstream rotor with the incoming wake.

Figure 4.13 shows line distributions of velocity and turbulence intensity along radial direction at z/R=0.47 for 0.25D (1^{st} row), 0.5D (2^{nd} row), 1D (3^{rd} row), and 2D (4^{th}

row) downstream locations. These plots illustrate some of the arguments presented previously in a more quantitative manner. The radially outward motion of the tip effects, the increase in the momentum and the turbulence levels, the streamwise diffusion of the flow near the tips and the fact that the tip injection causes a spreading of the turbulence intensity distributions can all be seen in these figures.

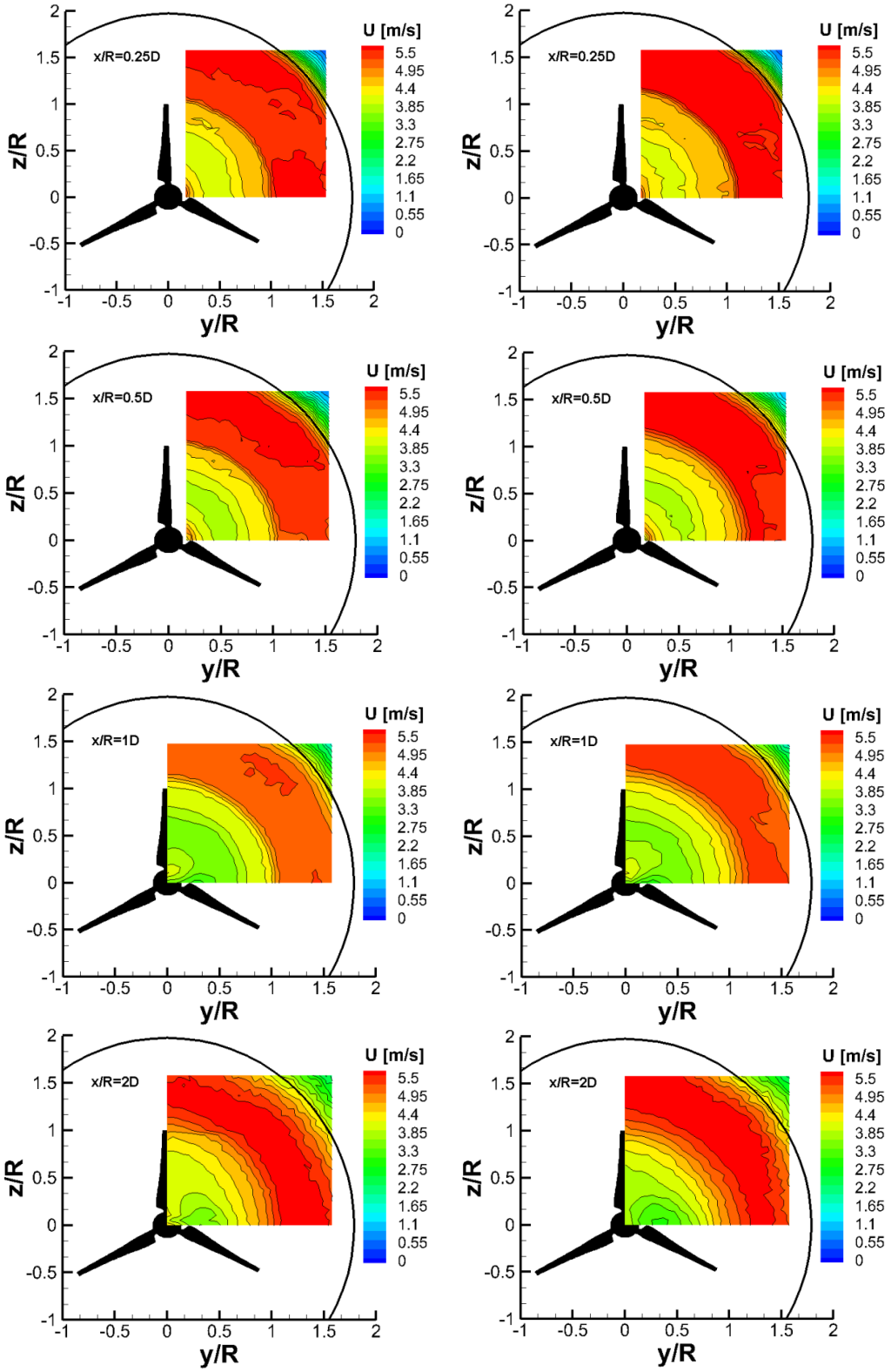

Figure 4.11: Velocity distributions within the wake of the turbine rotor**.** ***Left column***: Baseline, ***Right column***: Injection Case @ R_M=1.3%. ***1st row:*** 0.25D, ***2nd row***: 0.5D, ***3rd row:*** 1D, ***4th row:*** 2D downstream planes. Flow is coming out of the page and the circular line marks the outline of the open-jet tunnel

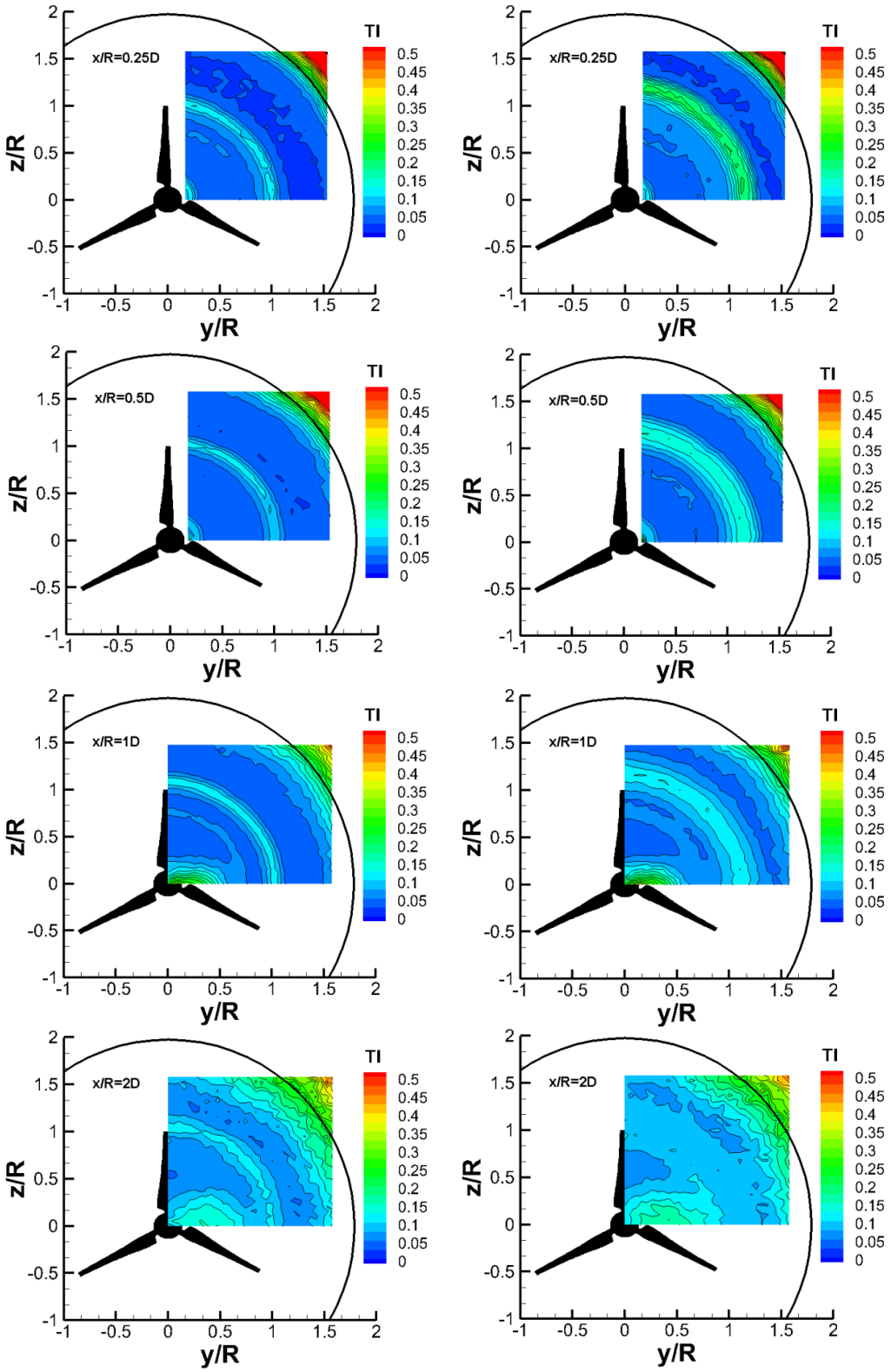

Figure 4.12: Turbulence intensity distributions within the wake of the turbine rotor. ***Left column*:** Baseline, ***Right column***: Injection Case @ R_M=1.3%. ***1st row***: 0.25D, ***2nd row***: 0.5D, ***3rd row***: 1D, ***4th row***: 2D downstream planes. Flow is coming out of the page and the circular line marks the outline of the open-jet tunnel

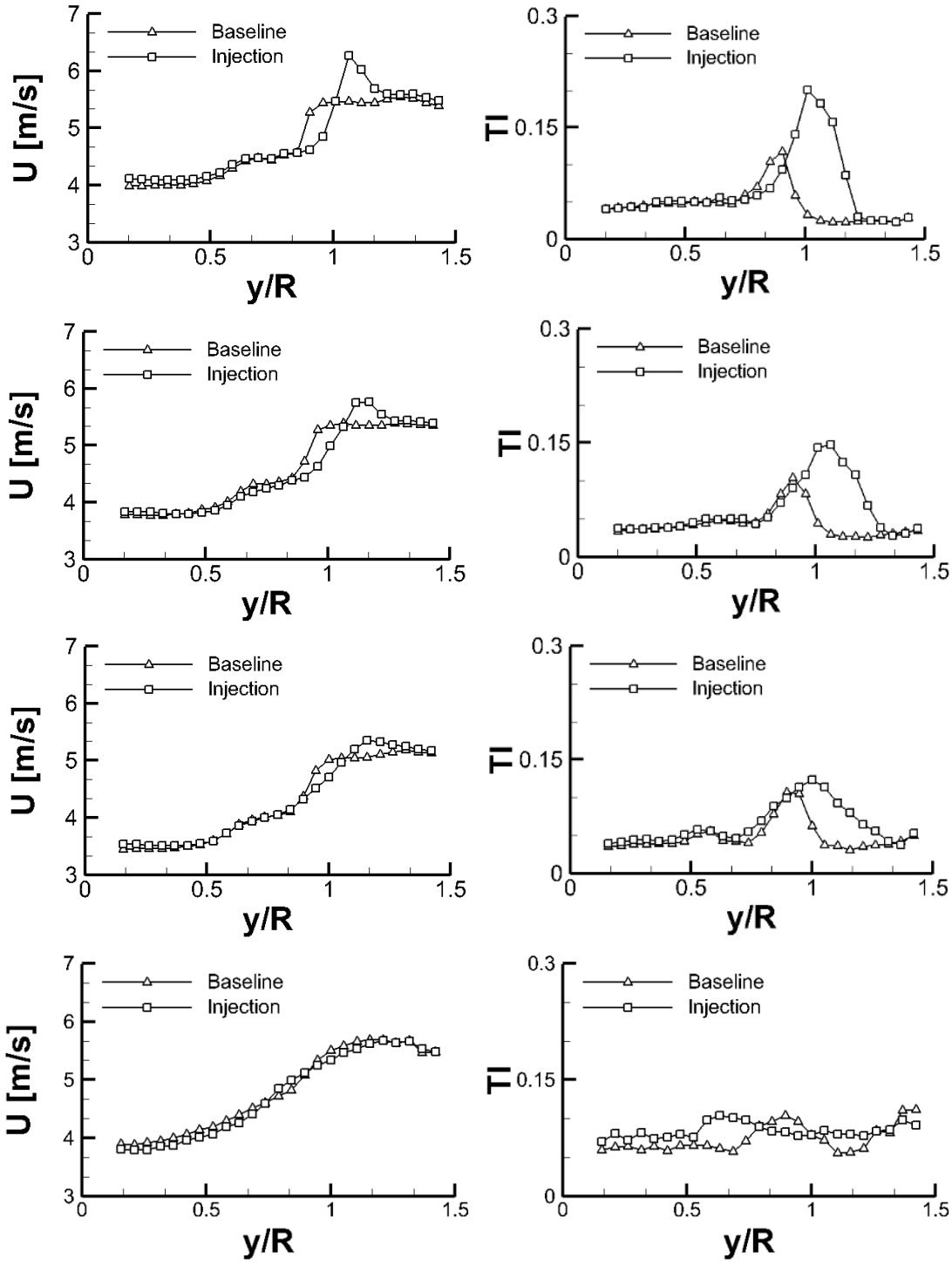

Figure 4.13: Velocity (left column) and turbulence intensity (right column) variations along radial direction at z/R=0.47. ***1st row***: 0.25D, ***2nd row***: 0.5D, ***3rd row***: 1D, ***4th row***: 2D downstream planes

4.6. TIP NEAR FIELD MEASUREMENTS

This section describes the measurements conducted downstream of the model wind turbine rotor blade tip. Measurement details and data acquisition are presented in chapter 3. Figure 3.3 and Figure 3.8 (right) show the measurement plane and setup for these tests. The aim of these experiments is to understand the tip flow field just downstream of the rotor blade tips. Moreover, to support our arguments in the previous sections in terms of the wake characteristics and to try to understand how the tip injection affects the tip vortex trajectory as well as its diffusion, which has a direct impact on the entire wake flow region.

Figures 4.14 and 4.15 show the velocity magnitude and turbulence intensity plots for both the baseline (1^{st} row) and injection (2^{nd} row) cases. The flow is coming from left to right. The plots show the model turbine and the measurement plane in the first columns. While, in the second columns a larger version of the velocity and turbulence intensity plots are presented to better visualize the flow field structure. The experiments have been conducted at a wind speed of 5 m/s and for TSR=5. The model wind turbine is placed half a rotor diameter away from the exit of the open-jet tunnel. The center of the hub and the tunnel centerline are concentric. The blades are installed at a zero pitch angle. The turbine is rotating in counterclockwise direction. That is, the turbine blades are coming out of the page as can be seen from the plots.

As shown in Figures 4.14 and 4.15, the flow field downstream of the rotor blade tip show typical tip vortex trajectory as expected for the baseline case. The plots show different flow regimes downstream of the blade tip characterized by low momentum zone in the wake of the rotor blade and starts to increase as you move along the radial direction until the velocity reaches the free stream velocity as shown in Figure 4.14. The tip vortex is clearly depicted in the velocity field plots. This is clearly shown in the turbulence intensity plots for the baseline case in Figure 4.15. The tip vortex trajectory shows similar behavior as expected for a typical wind turbine rotor characterized by two paths shed from the blade tip.

For the injection cases as presented in the 2nd row for the velocity magnitude and turbulence intensity plots. It is clear that injection has significant effects on the flow field downstream of the rotor blade tip. The trajectory of the tip vortex and the near wake flow characteristics have been significantly influenced by injection. It appears that injection causes increased diffusion and mixing downstream of the rotor. Furthermore, the injection seems to increase the width of the wake region, which the effects have been clearly shown in the previous sections where the wake measurements have been presented. These results clearly support our observations related to the effects that injection imposes on the flow field downstream of the rotor.

Figure 4.16 shows the velocity and turbulence intensity variations along the radial direction for both the baseline as well as the injection cases at different axial locations downstream of the blade tip. These plots illustrate some of the arguments presented previously in a more quantitative manner. It is clear from the figures that injection has caused an increase in velocity and turbulence levels especially near the tip region. It shows that the distinct peaks resulting from the tip vortex in the turbulence intensity plots are no longer present when injection is applied.

Figure 4.17 shows the velocity and turbulence intensiy variations along the radial direction at different axial locations downstream of the rotor blade tip for both the baseline case (1st row) and injection case (2nd row). The velocity profiles shows expected trends starting from a low velocity region located behind the rotor and increases until it reaches the freestream velocity. All three locations downstream of the blade tip shows similar trends and they all collapse into a single line especially in the freestream region. However, they show distinct differences in the wake region as expected. As one moves downstream of the rotor blade tip the velocity starts to drop as shown for the 0.65R case. On the other hand, the turbulence intensity plots show similar trends and as expected there appear to be two distinct peaks representing the tip vortex strength.

Whereas for the injection cases, the velocity and turbulence intesity show different variations especially near the blade tip region. The velocity magnitude shows

increased velocity due to tip injection, and thr turbulence levels are 3 times higher compared to the baseline case. As a result of tip injection, there exit more diffusion and mixing downstream of the blade tip resulting in drastically changing the tip vortex trajectroy and its chracteristics. Further downstream it seems that the flow is expanding around the blade tip region resulting in higher velocity magnitude and turbulence intensity levels in the wake region, which we have seen its effects iin previous sections.

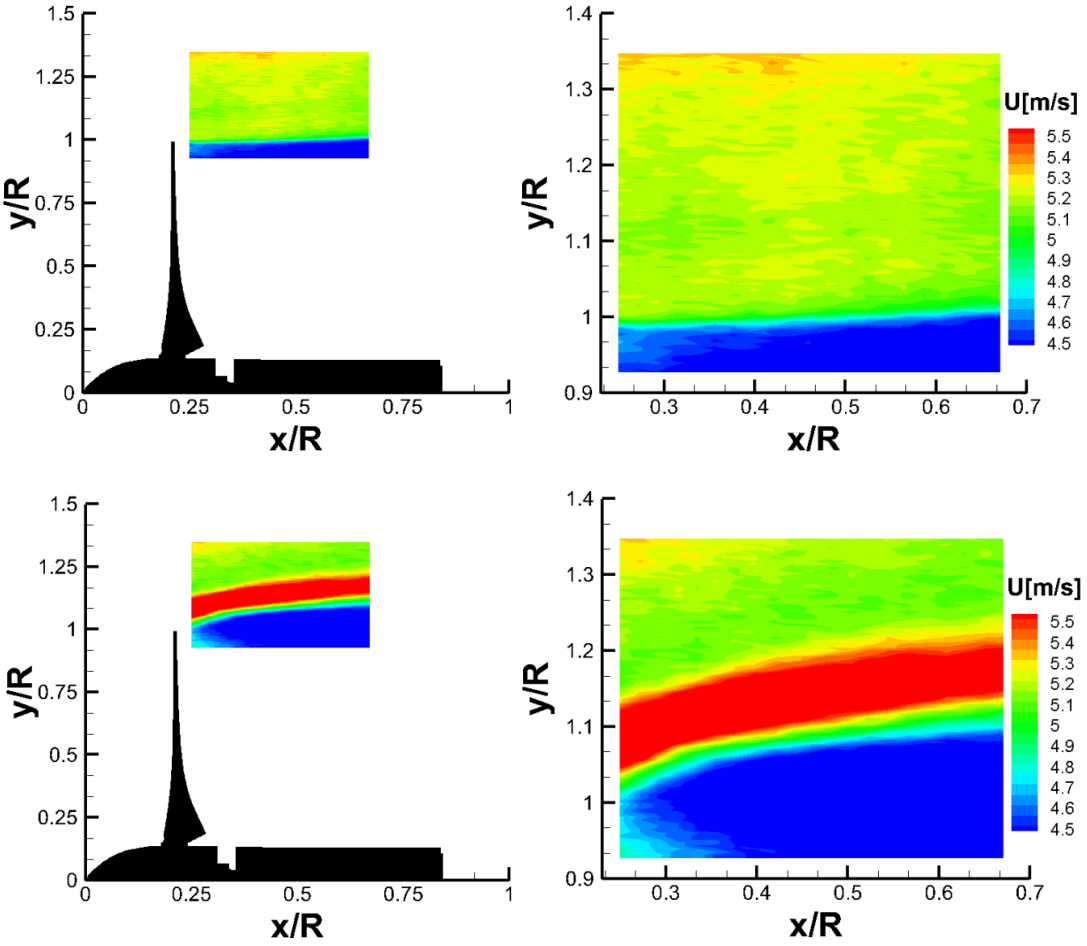

Figure 4.14: Velocity magnitude distributions downstream of blade tip region @ U_∞=5 m/s & TSR=5. ***1st row***: Baseline case, ***2nd row***: Injection case @ R_M=1.3%

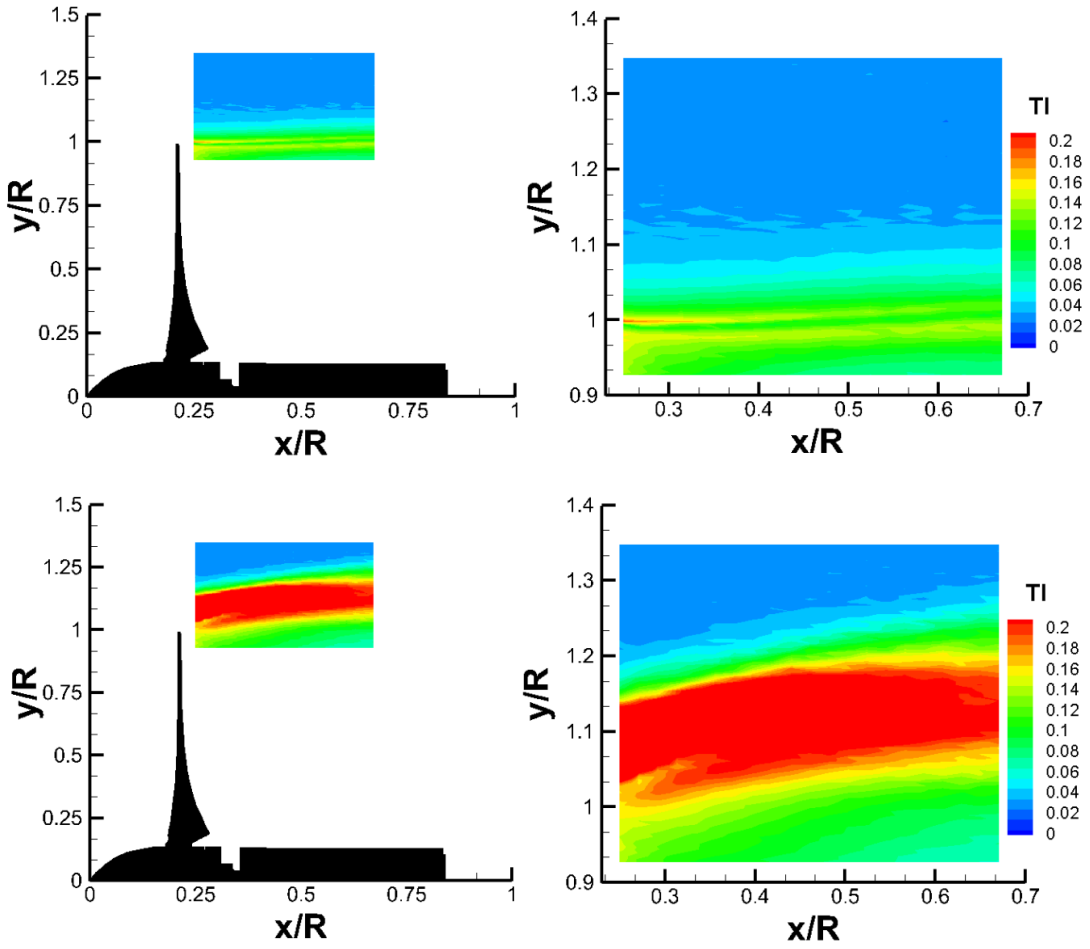

Figure 4.15: Turbulence intensity distributions downstream of blade tip region @ U_∞=5 m/s & TSR=5. ***1st row***: Baseline case, ***2nd row***: Injection case @ R_M=1.3%

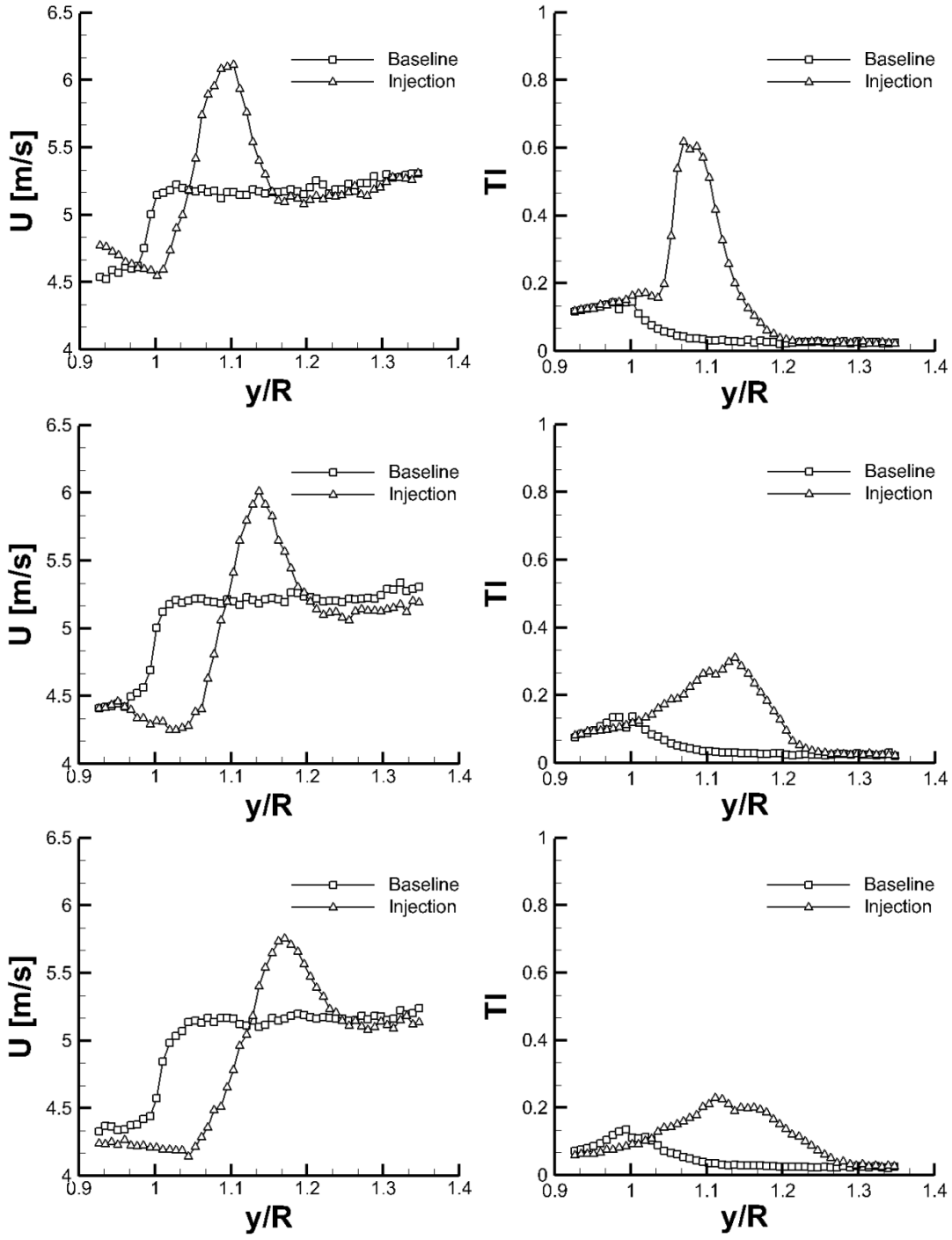

Figure 4.16: Velocity (left column) and turbulence intensity (right column) variations along radial direction at U_∞=5 m/s & TSR=5. ***1st row***: 0.27R, ***2nd row***: 0.44R, ***3rd row***: 0.65R downstream of the blade tip

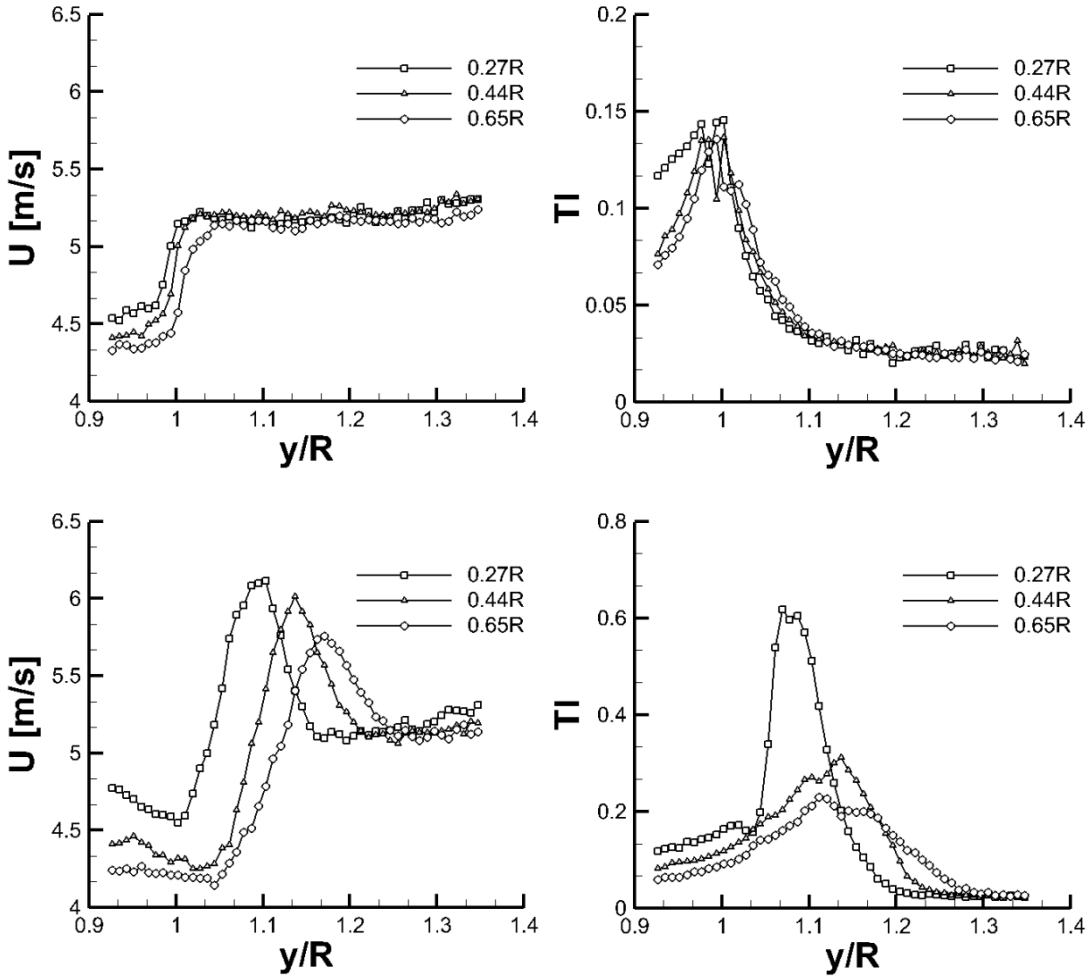

Figure 4.17: Velocity (left column) and turbulence intensity (right column) variations along radial direction at U_∞=5 m/s & TSR=5 for different axial locations downstream of the blade tip. ***1st row***: Baseline case, ***2nd row***: Injection case @ R=1.3%

CHAPTER 5

CONCLUSIONS AND FUTURE WORK

5.1. CONCLUSIONS

This thesis study summarizes the results of an experimental investigation of the effects of tip injection on the performance and wake characteristics of a model wind turbine rotor. Firstly, baseline measurements have been conducted to quantify the performance and to check the reliability of the model wind turbine by obtaining the power and thrust coefficient variations for several TSR and wind speeds as well as by comparing the model turbine performance with a similar replica located at the Norwegian University of Science and Technology (NTNU). Secondly, the power and thrust coefficients variations at different TSR for different wind speeds and injection ratios have been obtained. Thirdly, the wake characteristics of the model wind turbine are obtained with Constant Temperature Anemometry (CTA) measurements downstream of the wind turbine rotor. Results show the reliability of the experimental setup and the power and thrust coefficients variations are as expected for a typical model wind turbine rotor. Furthermore, for the injection cases, obtained characteristics have remarkable differences compared to the baseline cases at the selected wind speeds. Most significant effects were observed for TSR values near maximum C_P condition up to higher levels. The case where the wind speed is 5 m/s shows the most promising effects of injection as compared to the other two cases. In addition, measurements near the tip region shows that when injection is applied the tip vortex trajectory as well as near field characteristics are significantly influenced. This resulted in increased diffusion and mixing of the flow field downstream of the rotor which is reflected on the wake measurements conducted downstream of the rotor plane at different axial locations. The wake characteristics have been substantially influenced due to injection, showing a tip flow region that is radially

pushed outwards and marked with increased levels of turbulence and packed with more contour lines occupying wider areas compared to the baseline case.

The tip injection used in the following study is for steady state control of the load data. Based on the PBC, the system shows a power deficiency when one uses tip injection, since we are spending more power on the injected air than we gain especially in terms of the increase in power and thrust coefficient variations. Therefore, tip injection is not efficient for increasing the power and thrust coefficients in steady state.

However, that doesn't mean tip injection is not useful to improve the performance of the wind turbine. This technique can be used for active load control in the off design conditions, that is when the turbine is not operating in optimal flow conditions. In this case, tip injection can be used for instantaneous active load control and can be controlled depending on flow conditions and load requirements. Even though this technique is not efficient in terms of load control especially for steady state conditions, it has significant effects on the wake flow field characteristics as shown previously. Therefore, tip injection might be useful especially in multiple turbine configurations such as wind farms, where the downstream turbine will be exposed to less concentrated tip vortices and this will change the performance as well as the interaction characteristics with the downstream turbines.

5.2. FUTURE WORK

Future work in order to improve this study and obtain further information related to the effect of tip injection on the performance and wake characteristics of the model wind turbine used in the experiments are presented in following points with other recommendations related to the entire experimental setup:

- A new set of metal blades need to be manufactured. This will help in obtaining power and thrust coefficients data at higher TSR without

experiencing any failure in the blades in terms of vibration and structural integrity.

- Tests need to be conducted at higher injection ratios in order to observe the effects of different injection rates on the load data and flow field characteristics. Thus, a powerful compressor has to be purchased in order to achieve this goal.
- More load data under yawed conditions, in order to see the effects of injection at these flow conditions.
- Phase-Locked Particle Image Velocimetry (PL-PIV) measurements has to be conducted within the wake and near the tip region, in order to support the CTA measurements, and to give further information related to the tip vortex flow field, tip vortex trajectory, tip vortex characteristics such as the turbulent kinetic energy and Reynolds stresses, as well as the time evolution of the tip vortex.
- Closed-loop torque and thrust control using tip injection. This study will be helpful in terms of controlling the injection technique depending on load requirements and flow conditions
- Using tip injection in multiple turbine interaction. Effects of tip injection on the performance and wake characteristics of a downstream wind turbine which will support our arguments onto whether the tip injection technique is useful in multiple turbine arrangements.

REFERENCES

[1] Manwell J.F., McGowan J.G., and Rogers A.L., "***Wind Energy Explained: Theory, Design and Application***", John Wiley & Sons Ltd., Second Edition, 2009

[2] Jain P., "***Wind Energy Engineering***", The McGraw-Hill Companies, first edition, September 2011

[3] Adaramola M.S., Krogstad P-Å, "***Experimental Investigation of Wake Effects on Wind Turbine Performance***", Renewable Energy, 2011. doi:10.1016/j.renene.2011.01.024

[4] Bartl J., "***Wake Measurements Behind an Array of Two Model Wind Turbines***", MSc. Thesis 2011, Norwegian University of Science and Technology (NTNU), Norway

[5] Vermeer L.J., Sørensen J.N., Crespo A., "***Wind Turbine Wake Aerodynamics***", *Progress in Aerospace Sciences*, 39:467–510, 2003

[6] Sanderse B., "***Aerodynamics of Wind Turbine Wakes***", Energy research Centre of the Netherlands, ECN-E-09-016, 2009

[7] Hedda P.B., "***An Experimental Investigation of Wind Turbine Wake***", MSc. Thesis 2012, Norwegian University if Science and Technology (NTNU), Norway.

[8]Gómez-Elvira R., Crespo A., Migoya E., Manuel F., Hernandez J., "***Anisotropy of Turbulence in Wind Turbine Wakes***", Journal of Wind Eng. and Ind. Aerodynamics, Elsevier Ltd., 2005, No. 93, pp. 797–8

[9] Gad-el-Hak M., "***Flow Control: Passive, Active, and Reactive Flow Management***", Cambridge University press, ISBN 0 521 77006, 2000

[10] Gad-el-Hak, M., "***Overview of Turbulence Control Research in U.S.A***.," Proceedings of the Symposium on Smart Control of Turbulence, ed. N. Kasagi, pp. 1-20, University of Tokyo, 2-3 Dec. 1999, Tokyo, Japan

[11] Kral L.D, "***Active Flow Control Technology***", ASME Fluids Engineering Division Technical Brief 1998

[12] Johansen J., Sørensen N., "***Aerodynamic investigation of Winglets on Wind Turbine Blades using CFD***", Risø-R-1543(EN), Risø National Laboratory, Roskilde 2006

[13] Elfarra, M.A., "***Horizontal Axis Wind Turbine Rotor Blade: Winglet and Twist Aerodynamic Design and Optimization Using CFD****",* PhD Thesis 2011, Middle East Technical University

[14] Gaunaa M., Johansen J., "***Determination of the Maximum Aerodynamic Efficiency of Wind Turbine Rotors with Winglets***", The Science of Making Torque from Wind (TORQUE2007), Jornal of Physics: Conference Series 75 (2007)-012006

[15] Shimizu Y., Imamura H., Matsumura S., Maeda T., ''***Power Augmentation of a Horizontal Axis Wind Turbine Using a Mie-Type Tip Vane: Velocity Distribution around the Tip of a HAWT Blade with and without a Mie-Type Tip Vane***'', ASME Journal Solar Energy Engineering, Vol.117, pp. 297–303, 1995

[16] Shimizu Y., Ismaili E., Kamada Y., Maeda T., "***Rotor Configuration Effect on the Performance of a HAWT with Tip-Mounted Mie-Type Vanes***", ASME Journal Solar Energy Engineering, Vol. 125, pp. 441–447, 2003

[17] Bai Y., Ma X., Ming X., "***Lift Enhancement of Airfoil and Tip Flow Control for Wind Turbine***", Applied Mathematics and Mechanics, Vol. 37, No. 7, pp. 825-836, 2011

[18] Barrett R., Farokhi S., "***Subsonic Aerodynamics and Performance of a Smart Vortex Generator System***", Journal of Aircraft, Vol. 33, No. 2, 1996

[19] Lin J.C., "***Control of Turbulent Boundary-Layer Separation using Micro-Vortex Generators***", AIAA Paper 99-3404, 30th AIAA Fluid Dynamics Conference, Norfolk, VA, 1999

[20] Weaver D., McAlister K.W., Tso J., "***Suppression of Dynamic Stall by Steady and Pulsed Upper-Surface Blowing***", NASA Tech. Paper 3600, ATCOM Tech Report 95-A-005, 1996

[21] Bons J., Sondergaard R., Rivir R., "***The Fluid Dynamics of LPT Blade Separation Control Using Pulsed Jets***", ASME Journal of Turbomachinery, Vol. 124, No. 1, pp. 77-85, 2002

[22] James R.D., Jacobs J.W., Glezer A., "***A Round Turbulent Jet Produced by an Oscillating Diaphragm***", *Phys. Fluids* 8:2484, 1996

[23] Smith B.L., Glezer A., "***The Formation and Evolution of Synthetic Jets***", Physics of Fluids, vol. 10, no. 9, pp. 2281-2297, 1998

[24] Post M.L., Corke T.C., "***Overview of Plasma Flow Control: Concepts, Optimization and Applications***", AIAA Paper 2005-0563, 2005

[25] Moreau E., "***Airflow Control by Non Thermal Plasma Actuators***", *Journal of Phys. D*, 40: 605-636, 2007

[26] Moreau E., Benard N., Jolibois M., Touchard G., "***Airflow Control by Plasma Actuators: Last Significant Results at the University of Poitiers***", 2nd European Conference for Aerospace Sciences, 2007

[27] Ostovan Y., "***Experimental Investigation of Waveform Tip Injection on the Characteristics of the Tip Vortex***", M.Sc. Thesis 2011, Middle East Technical University

[28] Bettle J.R., "***Experimental Study of a Wing Tip Vortex with Tip Blowing***", M.Sc. Thesis 2004, The University of New Brunswick, Canada

[29] Duraisamy K., Baeder J. D., "***Control of Helicopter Rotor Tip Vortex Structure Using Blowing Devices***", 60th Annual Forum Proceedings, American Helicopter Society, Vol. 2, pp. 1952-1967, 2004

[30] Vasilescu R., "***Helicopter Blade Tip Vortex Modifications in Hover Using Piezoelectrically Mounted Blowing***", PhD Thesis 2004, Georgia Institute of Technology, USA

[31] Liu Z., Sankar L.N., Hassan A.A., "***Alteration of the Tip Vortex Structure of a Hovering Rotor Using Oscillatory Jet Excitation***", AIAA Paper 99-0906, 2000

[32] Han Y.O., Leishan J.G., "***Investigation of Helicopter Rotor-Blade-Tip-Vortex Alleviation Using a Slotted Tip***", AIAA Journal, Vol. 42, No. 3, pp. 524-535, 2004

[33] Mercan B., "***Experimental Investigation of the Effects of Waveform Tip Injection on the Characteristics of Tip Leakage Vortex in a LPT Cascade***", M.Sc. Thesis 2012, Middle East Technical University

[34] Mercan B., Doğan E., Ostovan Y., Uzol O., "***Experimental Investigation of the Effects of Waveform Tip Injection in a Low Pressure Turbine Cascade***", ASME Turbo Expo 2012, Copenhagen, Denmark

[35] Rao N.M., "***Desensitization of over Tip Leakage in an Axial Turbine Rotor by Tip Surface Coolant Injection***", PhD Thesis 2005, Pennsylvania State University, USA

[36] Niu M., Zang S., "***Experimental and Numerical Investigations of Tip Injection Clearance Flow in an Axial Turbine Cascade***", Journal of Experimental Thermal and Fluid Science 35, 1214-1222, 2011

[37] Scheiman J., Brookst J.D., "***Comparison of experimental and theoretical turbulence reduction from screens, honeycomb, and honeycomb-screen combinations***," AIAA, Vol.18, no.8, 1981

[38] Farell C., Sadek Y., "***Experiments on turbulence management using screens and honeycombs***," St. Anthony Falls Hydraulic Laboratory, University of Minnesota, 1992

[39] Vinayak K., Bradshaw P., "***Simulation of honeycomb-screen combinations for turbulence management in a subsonic wind tunnel***," Journal of Wind Engineering and Industrial Aerodynamics, 2011

[40] Ghorbanian K., Soltani M.R., Manshadi M.D., "***Experimental Investigation on Turbulence Intensity Reduction in Subsonic Wind Tunnels***", Aerospace Science and Technology, Vol. 15, pp. 137-147, 2011

[41] Metha R.D., Bradshaw P., "***Design Rules for Small Low Speed Wind Tunnels***", The Aeronautical Journal of the Royal Aeronautical Society, 1979

[42] Groth J., Johansson A.V., "***Turbulence Reduction by Screens***," J. Fluid Mech., Vol.197, pp. 139-155, 1988

[43] Laws E.M., Livesey J.L., "***Flow through Screens***," Ann. Rev. Fluid Mech., Vol.10, pp. 247-266, 1978

[44] Arifuzzaman M., Mashud M., "***Design Construction and Performance Test of a Low Cost Subsonic Wind Tunnel***", IOSR Journal of Engineering (IOSRJEN). Vol. 2. pp. 83-92, 2012

[45] Scheiman J., "***Some Considerations of the Configuration and Installation of Honeycomb and Screens to Reduce Wind Tunnel Turbulence***," NASATM-81868, Aug. 1981

[46] Barlow J.B., Rae J.R., Pope A., "***Low-Speed Wind Tunnel Testing"***, (3rd ed.). Wiley-Interscience Publication, 1999

[47] AIOLOS Engineering Corporation, "***METUWIND Large Scale Wind Tunnel Airline Design***", design report 4201/R357 Rev B, 4th January 2013

[48] Uzol O., "***Yatay Eksenli Rüzgar Türbinlerinde Uç Enjeksiyonu Kullanılarak Aktif Uç Girdabı Kontrolü Yönteminin Deneysel İncelenmesi"***Gelişme Raporu (1), TÜBİTAK, 2013

[49] Krogstad P-Å., Lund J.A., "***An Experimental and Numerical Study of the Performance of a Model Turbine***", Wind Energy, John Wiley & Sons, Ltd., 2011. DOI: 10.1002/we.482

[50] Karlsen, J.A., "***Performance Calculations for a Model Wind Turbine***" M.Sc. Thesis 2009, Norwegian University of Science and Technology (NTNU), Norway

[51] Somers D.M., "***The S825 and S826 Airfoils***", Period of Performance: 1994 – 1995 National Renewable Energy Laboratory, Airfoils, Inc., 2005

[52] Jorgensen, F.E., "***How to Measure Turbulence with Hot-wire Anemometers-A practical Guide***", Skovlunde, Denmark; Dantec Dynamics, 2002 Publication no: 9040U6151

[53] Probst O., Martínez J., Elizondo J., Monroy O., "***Small Wind Turbine Technology Wind Turbines***", Dr. Ibrahim Al-Bahadly (Ed.) ISBN: 978-953-307-221-0 InTech DOI: 10.5772/15861, 2011

[54] Tavella D.A., Wood N.J., Lee C.S., Roberts L., "***Lift Modulation with Lateral Wing- Tip Blowing",*** *Journal of Aircraft* Vol. 25 No. 4 pp 311-316, 1998

[55] Gursul I., Vardaki E., Margaris P., Wang Z., "***Control of Wing Vortices Active Flow Control",*** *Notes on Numerical Fluid Mechanics and Multidisciplinary Design* pp.137-151 Springer-Verlag Berlin, 2007

[56] Ostovan Y., Hazaveh H.A., Uzol O., "***Aerodynamic Characterization of NREL S826 Airfoil at Low Reynolds Numbers***", Conference on Wind Energy Science and Technology - RUZGEM 2013, Ankara, Turkey

[57] Schlichting H., "***Boundary-Layer Theory***", McGraw-Hill Series in Mechanical Engineering, 7^{th} edition 1979.

APPENDIX A

FAN SPECIFICATIONS AND DIMENSIONS

Table A.1: Fan specification

Curve Code	Fan Diameter	Fan Speed	Power Input	Electric Motor	Noise Level db (A) 3m/1m
	mm	rpm	Kw-Hp		
H4/1200-45A	1200	1500	30-40	200L	97/98

Table A.2: Fan performance

Air Flow Rate (m^3/h) – Static Pressure (mm/WG)							
20	30	40	50	60	70	80	90
94200	92000	87900	84000	77500	55000	33000	20000

Note that:
1 m3/h = 3600 m3/s
1 CFM = 1.699 m3/h
1 mmWG = 9.80665 Pa

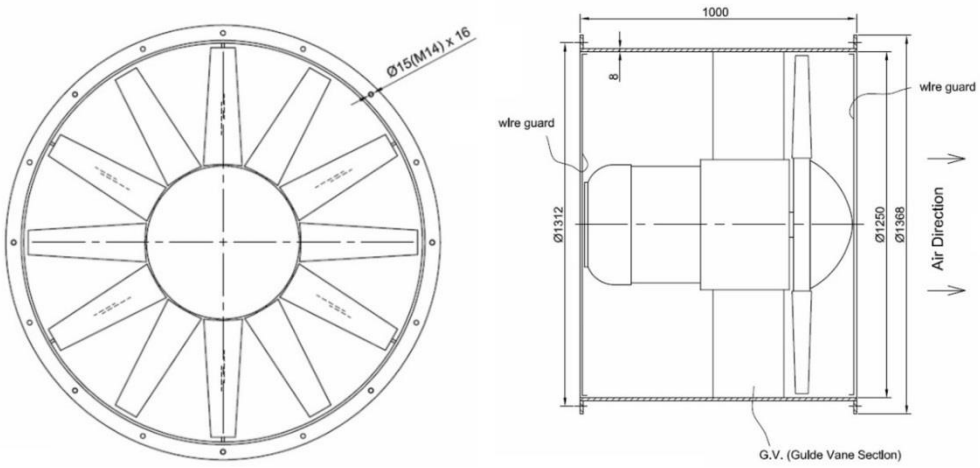

Figure A.1: (Left) normal view of the fan, (right) Side view of the fan

APPENDIX B

MEASURED POWER AND THRUST COEFFICIENTS DATA

Table B.1: Measured power and thrust coefficient variations with TSR

	U_∞=4 m/s											
	Baseline			Injection @ R_M=0.3 % (R_V=9)			Injection @ R_M=1.1 % (R_V=19)			Injection @ R_M=2.0 % (R_V=25)		
TSR	C_p	C_T	C_T'	C_p	C_T	C_T'	C_p	C_T	C_T'	C_p	C_T	C_T'
0.00	0.00	0.12	0.09	0.00	0.11	0.08	0.00	0.12	0.09	0.00	0.13	0.10
0.62	0.01	0.13	0.10	0.01	0.12	0.09	0.00	0.12	0.09	0.01	0.14	0.11
1.23	0.03	0.17	0.14	0.01	0.15	0.12	0.01	0.16	0.13	0.04	0.18	0.15
1.85	0.05	0.21	0.18	0.01	0.19	0.17	0.02	0.20	0.17	0.06	0.23	0.20
2.46	0.07	0.26	0.23	0.03	0.24	0.22	0.04	0.25	0.23	0.07	0.28	0.25
3.09	0.11	0.31	0.28	0.06	0.29	0.26	0.06	0.30	0.27	0.09	0.33	0.30
3.73	0.17	0.37	0.34	0.11	0.35	0.32	0.11	0.36	0.34	0.17	0.41	0.37
4.57	0.30	0.52	0.49	0.26	0.47	0.44	0.25	0.49	0.46	0.35	0.54	0.51
5.10	0.20	0.49	0.46	0.19	0.46	0.43	0.15	0.48	0.45	0.26	0.54	0.50
5.58	0.18	0.47	0.44	0.14	0.46	0.43	0.09	0.48	0.45	0.23	0.55	0.52
6.17	0.16	0.48	0.45	0.10	0.47	0.44	0.07	0.49	0.46	0.22	0.55	0.52
6.81	0.10	0.47	0.44	0.04	0.47	0.44	0.02	0.49	0.46	0.14	0.55	0.52
7.40	0.07	0.47	0.44	-0.01	0.47	0.44	0.00	0.50	0.47	0.08	0.57	0.54
8.04	-0.02	0.46	0.43	-0.06	0.46	0.43	-0.06	0.49	0.46	0.04	0.57	0.54
	U_∞=5 m/s											
	Baseline			Injection @ R_M=0.2 % (R_V=7)			Injection @ R_M=0.7 % (R_V=15)			Injection @ R_M=1.3 % (R_V=20)		
TSR	C_p	C_T	C_T'	C_p	C_T	C_T'	C_p	C_T	C_T'	C_p	C_T	C_T'
0.00	0.00	0.11	0.08	0.00	0.13	0.10	0.00	0.12	0.10	0.00	0.13	0.10
0.49	0.01	0.11	0.09	0.00	0.13	0.11	0.00	0.13	0.10	0.00	0.13	0.10
0.98	0.01	0.14	0.11	0.01	0.16	0.13	0.01	0.16	0.13	0.02	0.16	0.13
1.48	0.02	0.17	0.14	0.02	0.19	0.16	0.02	0.20	0.17	0.03	0.19	0.16
1.98	0.04	0.20	0.18	0.04	0.23	0.20	0.04	0.25	0.22	0.03	0.23	0.20
2.48	0.06	0.25	0.22	0.06	0.29	0.26	0.06	0.29	0.26	0.05	0.27	0.25
2.98	0.08	0.29	0.26	0.08	0.32	0.29	0.08	0.32	0.29	0.08	0.31	0.29
3.47	0.11	0.33	0.31	0.12	0.36	0.33	0.12	0.36	0.34	0.13	0.36	0.34
3.96	0.24	0.42	0.40	0.26	0.45	0.43	0.26	0.46	0.43	0.28	0.46	0.43
4.47	0.27	0.48	0.45	0.30	0.53	0.51	0.33	0.56	0.53	0.37	0.55	0.52
4.97	0.24	0.47	0.45	0.26	0.51	0.49	0.28	0.53	0.50	0.36	0.59	0.56

5.46	0.19	0.46	0.43	0.21	0.51	0.49	0.25	0.54	0.51	0.32	0.60	0.57
5.95	0.17	0.47	0.44	0.19	0.51	0.48	0.20	0.54	0.51	0.24	0.57	0.54
6.45	0.15	0.47	0.45	0.16	0.51	0.49	0.19	0.54	0.52	0.21	0.58	0.55
	U_∞=6 m/s											
	Baseline			**Injection @ R_M=0.1 % (R_V=6)**			**Injection @ R_M=0.5 % (R_V=13)**			**Injection @ R_M=0.9 % (R_V=17)**		
TSR	**C_p**	**C_T**	**C_T'**	**C_p**	**C_T**	**C_T'**	**C_p**	**C_T**	**C_T'**	**C_p**	**C_T**	**C_T'**
0.00	0.00	0.12	0.09	0.00	0.12	0.09	0.00	0.12	0.10	0.00	0.12	0.10
0.41	0.01	0.12	0.09	0.01	0.12	0.10	0.00	0.13	0.10	0.00	0.12	0.10
0.83	0.01	0.14	0.11	0.01	0.14	0.12	0.01	0.15	0.12	0.01	0.14	0.12
1.24	0.02	0.16	0.14	0.02	0.17	0.14	0.02	0.18	0.15	0.01	0.17	0.14
1.65	0.03	0.19	0.17	0.03	0.19	0.17	0.03	0.21	0.18	0.02	0.20	0.17
2.07	0.04	0.22	0.20	0.04	0.23	0.20	0.04	0.24	0.21	0.04	0.23	0.21
2.48	0.07	0.27	0.25	0.05	0.26	0.24	0.06	0.27	0.25	0.06	0.27	0.25
2.91	0.09	0.31	0.28	0.08	0.30	0.27	0.07	0.31	0.29	0.07	0.31	0.29
3.33	0.12	0.34	0.31	0.11	0.34	0.31	0.09	0.35	0.33	0.11	0.35	0.33
3.73	0.21	0.40	0.37	0.18	0.39	0.37	0.17	0.41	0.39	0.20	0.41	0.39
4.15	0.34	0.49	0.46	0.31	0.48	0.46	0.32	0.49	0.47	0.35	0.49	0.46
4.59	0.38	0.55	0.53	0.37	0.55	0.52	0.38	0.57	0.54	0.40	0.57	0.54
5.00	0.34	0.55	0.52	0.33	0.55	0.53	0.34	0.58	0.55	0.40	0.61	0.59
5.43	0.32	0.55	0.52	0.31	0.55	0.53	0.30	0.57	0.54	0.33	0.59	0.57

APPENDIX C

MEASURED INJECTION SYSTEM PARAMETERS

Table C.1: Mass and momentum calculations for the inlet, exit and flow conditions

Total amount of injected mass flow rate and momentum existing the blade tips								
	P_{total}	P_{static}	$P_{dynamic}$	U_{jet}	$\dot{m}_{jet}$	$\dot{m}_{jet,total}$	mom_{jet}	$mom_{jet,total}$
Blade 1	730.29	-11.91	742.20	**35.11**	3.04E-04	**9.50E-04**	1.07E-02	**3.47E-02**
Blade 2	845.33	-11.18	856.51	**37.72**	3.27E-04		1.23E-02	
Blade 3	796.84	-14.49	811.32	**36.71**	3.18E-04		1.17E-02	

Total amount injected mass flow rate and momentum existing the blade tips								
	P_{total}	P_{static}	$P_{dynamic}$	U_{jet}	$\dot{m}_{jet}$	$\dot{m}_{jet,total}$	mom_{jet}	$mom_{jet,total}$
Blade 1	3748.50	-68.41	3816.91	**79.62**	6.90E-04	**2.01E-03**	5.50E-02	**1.55E-01**
Blade 2	3277.27	-83.98	3361.25	**74.72**	6.48E-04		4.84E-02	
Blade 3	3486.13	-82.94	3569.07	**76.99**	6.67E-04		5.14E-02	

Total amount injected mass flow rate and momentum existing the blade tips								
	P_{total}	P_{static}	$P_{dynamic}$	U_{jet}	$\dot{m}_{jet}$	$\dot{m}_{jet,total}$	mom_{jet}	$mom_{jet,total}$
Blade 1	5080.62	-172.70	5253.32	**93.41**	8.10E-04	**2.67E-03**	7.56E-02	**2.75E-01**
Blade 2	6988.41	-187.40	7175.81	**109.17**	9.46E-04		1.03E-01	
Blade 3	6483.99	-177.79	6661.78	**105.19**	9.12E-04		9.59E-02	

Mass flow rate and momentum of air going through the rotor disk		
U_{∞}	$\dot{m}_{rotor}$	mom_{rotor}
4 m/s	3.41	1.37
5 m/s	4.27	2.13
6 m/s	5.12	3.07

Ratio of total amount of injected mass flow rate and momentum to the mass flow rate and momentum of air going through the rotor disk									
	$U_{\infty} = 4\ m/s$			$U_{\infty} = 5\ m/s$			$U_{\infty} = 6\ m/s$		
FM reading	$\mathbf{R_I}$	$\mathbf{R_M}$	$\mathbf{R_V}$	$\mathbf{R_I}$	$\mathbf{R_M}$	$\mathbf{R_V}$	$\mathbf{R_I}$	$\mathbf{R_M}$	$\mathbf{R_V}$
100 L/min	0.03%	0.3%	9	0.02%	0.2%	7	0.02%	0.1%	6
140 L/min	0.06%	1.1%	19	0.05%	0.7%	15	0.04%	0.5%	13
180 L/min	0.08%	2.0%	25	0.06%	1.3%	20	0.05%	0.9%	17

JET POWER CALCULATION

The kinetic energy or the jet power of the injected air from the blade tips has been calculated according to basic fluid mechanics equations for pipe flows through non-circular conduits [57].

The velocity measured at the blade tips while the rotor is stationary represents the maximum velocity at the tip. In reality the velocity at the tip is not uniform, at the blade tip which represents a channel with rectangular cross section a velocity profile forms which is maximum at the channel centerline and minimum at the channel walls. This velocity profile is defined according to the flow regime, i.e. whether the flow is laminar or turbulent. Based on the Reynolds number formula defined as shown in the equation below:

$\mathrm{Re} = \frac{\rho U D_h}{\mu}$, where D_h is the hydraulic diameter defined for non-circular conduits.

$D_h = \frac{4A_c}{p}$, where A_c is the channel cross sectional area and p is the perimeter.

Therefore, $\mathrm{Re} = 13166.79 > 4000$ thus we have a turbulent flow inside the channel. According to Schlichting [57], for pipe flows inside circular or non-circular conduits, if the Re>4000, the flow is set to be a turbulent flow. Moreover, one can calculate the entrance length for a turbulent flow defined as follows; $L_e = 4.4 D_h \mathrm{Re}^{1/6} = 4.33 cm$, and the channel total length is 43 cm, therefore, we have a fully developed turbulent flow.

According to Schlichting [57], for a fully developed velocity profile in a turbulent flow, the average velocity can be obtained from the maximum velocity according to the following equation: $\frac{\bar{u}}{U} = 0.791$ for the Reynolds number calculated previously.

From the above mentioned equation we can obtain the average velocity and use this velocity to calculate the amount of mass flow rate exiting the blade tips. Consequently the kinetic energy of the injected air is obtained as shown in chapter 4.3.